APPLICATION SPECIFIC SPECIALTY OPTICAL FIBERS AND WAVEGUIDES

by

THAN SINGH SAINI

DEPARTMENT OF APPLIED PHYSICS

Submitted

in fulfilment of the requirements of the degree of

DOCTOR OF PHILOSOPHY

to the

DELHI TECHNOLOGICAL UNIVERSITY

DELHI - 110042 (INDIA)

SEPTEMBER 2015

DELHI TECHNOLOGICAL UNIVERSITY

CERTIFICATE

This is to certify that the Ph.D. thesis entitled **"APPLICATION SPECIFIC SPECIALTY OPTICAL FIBERS AND WAVEGUIDES"** submitted to the Delhi Technological University, Delhi for the award of Doctor of Philosophy is based on the original research work carried out by me under the supervision of Dr. Ajeet Kumar and Prof. Ravindra Kumar Sinha, Department of Applied Physics, Delhi Technological University, Delhi, India. It is further certified that the work embodied in this thesis has neither partially nor fully submitted to any other university or institution for the award of any degree or diploma.

21/09/2015

Than Singh Saini
Candidate
(Enrolment No: 2K11/Ph.D./AP/05)

This is to certify that the above statement made by the candidate is correct to the best of our knowledge.

21-09-15

Dr. Ajeet Kumar
(Supervisor)
Assistant Professor, Applied Physics
Delhi Technological University

21/09/2015

Prof. Ravindra Kumar Sinha
(Supervisor)
Professor, Applied Physics
Delhi Technological University

21.09.2015

Prof. Suresh C. Sharma
Head of the Department, Applied Physics
Delhi Technological University

IN THE MEMORY

OF

MY GRAND MOTHER

ACKNOWLEDGEMENTS

This thesis is the result of four years of work whereby I have been accompanied and supported by many people. It is a pleasant aspect that I have now the opportunity to express my gratitude for all of them.

First of all, I would like to express my greatest gratitude to my supervisors Dr. Ajeet Kumar and Prof. Ravindra Kumar Sinha for their proficient guidance and continued encouragement for the fulfillment of the research work. With great pleasure I express my heartfelt gratitude for their advice, fruitful discussions, numerous suggestions, constructive criticism, and constant support throughout the period of my research.

I take this opportunity to express my profound respect to the Vice Chancellor, Delhi Technological University and Head of the Department, Applied Physics, Delhi Technological University for providing the basic infrastructural facilities for carrying out the research work. I further place on record, my thanks to SRC and DRC members Professor S. C. Sharma (Chairman DRC), Prof. Anurag Sharma (External Expert), Prof. B. Chandra (External Expert), Dr. V. K. Sharma (External Expert), Dr. Yogita Kalra (Internal Expert) and Dr. S. K. Soni (Internal Expert) for taking their time serving in my committee and giving me valuable suggestions on my thesis.

My sincere thanks to Dr. P. K. Tyagi and Dr. V. K. Sharma (Delhi University), Dr. Y. Kalra, Prof. S. K. Garg, Dr. A. Singh, Dr. S. N. Khera and my supervisors for their lectures delivered during my Ph.D course work and their continuous encouragement towards the research work. I would also like to thank to Prof. Vipul Rastogy, IIT Roorkee and Dr. Shailendra K. Varshney, IIT Kharagpur for their fruitful research discussion and showing constant interest in my research work. I am very thankful to all the teachers who trained me since the time of my early study. Specially, I am sincerely obliged to Prof. S. S. Sheoran, S. V. College Aligarh for helping and providing moral support during my graduation and post graduation.

The inspiration, support, cooperation and patience which I have received from my friends are beyond the scope of any acknowledgement, yet I would express my heartfelt gratitude to them. I must praise the company of my flat mates Amit Kumar Vishwakarma and Vinay Kumar Yadav. I also express my thanks to all the research

scholar of the department for their constant support and understanding. My special thanks to my lab mates specially Jiten Baruah, Kamal Kishore, Neeraj Sharma, Venus Dillu, Preeti Rani, Nishant Shankhwar and Reena for their support and positive input. I would also like to thank all the B. Tech and M. Tech students specially Kishor Dinkar Naik, A G N Chatainya, Akshit Peer and Gautam Prabhakar who have completed their project work in TIFAC-Center of Relevance and Excellence in fiber optics and optical communication, Advanced Photonics Laboratory and have contributed for these laboratories.

I am in dearth of proper words to express my feeling towards my respected parents for their immutable encouragement, moral support and blessings. My parents teach me the most important principles I should follow in my life. I am devoid of proper words to express my abounding feeling for my all brothers and sisters who always helped me. I am glad to be one of them. I am humbly thankful to my uncle and aunty for loving, caring and providing study environment at their home during my college days. I could not achieve all this without their loving support.

I gratefully acknowledge the initiatives and support towards establishment of TIFAC Centre of Relevance and Excellence in Fiber Optics and Optical Communication at Delhi Technological University, Delhi through "Mission REACH" program of Technology Vision-2020, Government of India.

I would like to thank SPIE (International Society of Optics and Photonics) and OSA (Optical Society of America) for supporting and recognition of my research work. I gratefully acknowledge the financial assistance provided by Delhi Technological University in the form of Junior Research Fellowship and Senior Research Fellowship during the period of my research.

Finally, I thank to all those who helped and supported me. Thank you so much!

Date: (**Than Singh Saini)**

Place: Delhi

ABSTRACT

In this thesis some novel designs of photonic crystal fibers and rectangular waveguides have been reported for the applications: i) in which the nonlinearity need to be eliminated (such as high power fiber lasers and amplifiers); ii) in which the nonlinearity need to be enhanced (such as supercontinuum and slow light generation). Large mode area photonic crystal fiber designs for high power fiber lasers and amplifiers have been achieved by tailoring the size of the air holes and introducing down doped fused silica rods in the selective air holes in the cladding region of the structures. The proposed designs offer effective single-mode operation even with large core size. Effective single-mode operation provides good beam quality at the output of fiber lasers. In the case of LMA waveguide design the trenches of lower refractive index in cladding region have been introduced in such a way that all the propagating modes become leaky. The basic principle behind the cladding profiles is to introduce the high leakage loss to the higher order modes while nominal leakage loss to the fundamental mode, which makes the design effectively single-moded.

Supercontiuum generation (the creation of broadband spectral components when an intense laser pulse passes through a highly nonlinear medium) is an area of exciting research that has been attracting scientific interest over last several decades. The mid-infrared spectral domain ranging from 2 – 15 μm is mainly important because of not only it contains two important windows (3 – 5 μm and 8 – 13 μm) in which the earth's atmosphere is relatively transparent but also the strong characteristic vibration transitions of most of the molecules in this domain. Mid-infrared molecular 'fingerprint region' is applicable in various important applications in different diverse fields such as medical, industry, security and astronomy. In this thesis a sincere attempt has been done to design and analyze the dispersion engineered photonic crystal fibers and rib waveguide geometries for ultra broadband mid-infrared supercontinuum sources. Ever increased supercontinuum spectrum spanning 2 – 15 μm in As_2Se_3 based chalcogenide photonic crystal fiber and rib waveguide has been achieved using femtosecond laser

source of relatively low peak power. Such ultra broadband supercontinuum spectrum has also been achieved using equiangular spiral photonic crystal fiber geometry.

Slow light with tunable features is investigated in doped and undoped tellurite fibers and As_2Se_3 based photonic crystal fiber geometries for telecommunication and computing applications. The maximum time delay up to 137 ns can be obtained using 1 meter long photonic crystal fiber pump with 100 mW. All the PCF and waveguide designs which are applicable for supercontinuum and slow light generation have been designed such that the propagating mode is strongly confined in small core of the structure, which makes the designs highly nonlinear.

Keywords: Photonic Crystal Fiber, Large Mode Area, Effective Single Mode, Low Bend Loss, Rib/Channel Waveguide, Supercontinuum Generation, Slow Light.

List of Publications

Papers in Refereed International Journal of Repute

1. **Than Singh Saini,** Ajeet Kumar, and Ravindra Kumar Sinha, "Triangular-core large-mode-area photonic crystal fiber with low bending loss for high power applications," ***Applied Optics*** *53*(31), 7246-7251 (2014).
2. **Than Singh Saini,** Ajeet Kumar, and Ravindra Kumar Sinha, "Design and analysis of large-core multi-trench channel waveguide for high power applications," ***Applied Optics*** *54*(19), 6134 – 6139 (2015).
3. **Than Singh Saini,** Ajeet Kumar, and Ravindra Kumar Sinha, "Broadband mid-infrared supercontinuum spectra spanning 2 – 15 μm using As_2Se_3 chalcogenide glass triangular-core graded-index photonic crystal fiber," *IEEE/OSA* ***J. Lightwave Technol.*** 33(18), 3914 – 3920 *(*2015).
4. **Than Singh Saini,** Ajeet Kumar, and Ravindra Kumar Sinha, "Broadband mid-IR supercontinuum generation in As_2Se_3 based chalcogenide photonic crystal fiber: A new design and analysis," ***Opt. Commun***. *347*, 13 – 19 (2015).
5. **Than Singh Saini,** Ajeet Kumar, and Ravindra Kumar Sinha, "Slow light generation in single mode tellurite fibers," ***J. Modern Optics*** *62*(7), 508 – 513 (2015).
6. **Than Singh Saini,** Amira Bailli, Ajeet Kumar, Rim Cherif, Mourad Zghal, and Ravindra Kumar Sinha, "Design and analysis of equiangular spiral photonic crystal fiber for mid-infrared supercontinuum generation," ***J. Modern Optics*** (In Press) 2015; DOI: 10.1080/09500340.2015.1051600
7. **Than Singh Saini,** Ajeet Kumar, and Ravindra Kumar Sinha, "Design of large-mode-area microstructured optical fiber with single-mode operation for high power fiber lasers" ***Advanced Science Letters*** (In Press) 2015.
8. Rim Cherif, Amine Bensalem, **Than Singh Saini**, Ajeet Kumar, Ravindra Kumar Sinha, and Mourad Zghal, "Design of small core tellurite photonic crystal fiber for slow light based application using stimulated Brillouin scattering" ***Opt. Engg***. *54*(7), 075101 – 075101-6 (2015).
9. Ravindra Kumar Sinha, Ajeet Kumar, and **Than Singh Saini,** "Analysis and Design of Single-Mode As_2Se_3-Chalcogenide Photonic Crystal Fiber for Generation of Slow Light with Tunable Features," ***IEEE J. Sel. Topics Quant. Electron***. (In Press) 2015.
10. **Than Singh Saini,** Ajeet Kumar, and Ravindra Kumar Sinha, "Ultra Broadband mid-infrared supercontinuum spectrum spanning 2 – 15 μm using dispersion engineered As_2Se_3 chalcogenide rib waveguide," ***IEEE J. Sel. Topics Quant. Electron.*** **(Under review).**
11. **Than Singh Saini,** Ajeet Kumar, and Ravindra Kumar Sinha, "Design and Analysis of an Asymmetric Large-Mode-Area Microstructured Optical Fiber with Low Bending Loss," ***Opt. Fiber Technol***. **(Under review).**

Papers in Conference/Workshop Proceedings:

1. **Than Singh Saini**; Ajeet Kumar; Rim Cherif; Ravindra K. Sinha; Mourad Zghal, "Design and analysis of rectangular photonic crystal fiber for supercontinuum generation," *Proc. SPIE* 9586, Photonic Fiber and Crystal Devices: Advances in Materials and Innovations in Device Applications IX, 95860G (August 26, 2015); doi:10.1117/12.2187884.
2. Kishor D. Naik; **Than Singh Saini**; Ajeet Kumar; Ravindra K. Sinha, "Design of single mode single polarization large mode area photonic crystal fiber," *Proc. SPIE 9586*, Photonic Fiber and Crystal Devices: Advances in Materials and Innovations in Device Applications IX, 95860H (August 26, 2015); doi:10.1117/12.2187902
3. Neerad Nandan, **Than Singh Saini**, Ajeet Kumar, Ravindra K. Sinha, "Design and analysis of chevrons shaped split ring resonator in the mid-infrared region," *Proc. SPIE 9544*, Metamaterials, Metadevices, and Metasystems 2015, 95441D (September 1, 2015); doi:10.1117/12.2188341
4. Ajeet Kumar, **Than Singh Saini**, Kishor Dinkar Naik, Ravindra Kumar Sinha, "Design and analysis of rectangular-core large-mode-area photonic crystal fiber," *Proc.* International Conference on Recent cognizance in wireless communication & image processing (ICRCWIP-2015), 16 – 17 January 2015, pp.46, Poornima Institute of Engineering & Technology, Jaipur, INDIA.
5. **Than Singh Saini**, Ajeet Kumar, Ravindra Kumar Sinha, "Design and analysis of a nano-fiber with all-normal and flat dispersion for supercontinuum generation," *Proc.* International Conference on Recent cognizance in wireless communication & image processing (ICRCWIP-2015), 16 – 17 Janary 2015, pp.46, Poornima Institute of Engineering & Technology, Jaipur, INDIA.
6. **Than Singh Saini**, Ajeet Kumar, Ravindra Kumar Sinha, "Design of large-mode-area microstructured optical fiber with single-mode operation for high power fiber lasers," *Proc*. International conference on Frontiers of Spectroscopy (ICFS-2015), 10 – 12 January 2015, pp. 218, Banaras Hindu University, Varanasi, INDIA.
7. **Than Singh Saini**, Ajeet Kumar, Ravindra Kumar Sinha, "Microstructured-core photonic crystal fiber with all normal dispersion for supercontinuum generation," *Proc*. Photonics 2014: 12th International Conference on Fiber Optics and Photonics @ OSA 2014, IIT Kharagpur, WB, India, December 13-16, 2014, T3A.38
8. **Than Singh Saini**, Ajeet Kumar, Ravindra Kumar Sinha, "Stimulated Brillouin scattering based tunable slow light in tellurite photonic crystal fiber," *Proc*. Photonics 2014: 12th International Conference on Fiber Optics and Photonics @ OSA 2014, IIT Kharagpur, WB, India, December 13-16, 2014, T3A.28
9. **Than Singh Saini**, Ajeet Kumar, Ravindra Kumar Sinha, "Design and analysis of highly nonlinear microstructured fiber for supercontinuum generation," *Proc*. IONS Asia-6 Kharagpur conference @ OSA 2014, IIT Kharagpur, WB, India, December 10-12, 2014; pp. 28-29; ***(Received Best Paper Presentation Award)***

10. **Than Singh Saini**, Ajeet Kumar, Ravindra Kumar Sinha, "Highly nonlinear triangular-core photonic crystal fiber with all normal dispersion for supercontinuum generation," *Proc*. Frontiers in Optics (FiO), Tucson, AZ (USA), October 19-23, 2014, ISBN: 1-55752-286-3, Long Wavelength Mid-IR to THz Fiber Devices I, FW1D. 4; http://dx.doi.org/10.1364/FIO.2014.FW1D.4

11. **Than Singh Saini**, Amira Baili, Vinita Dahiya, Ajeet Kumar, Rim Cherif, Mourad Zghal, Ravindra Kumar Sinha, "Design of equiangular spiral photonic crystal fiber for supercontinuum generation at 1550 nm," *Proc. SPIE* 9200, Photonic Fiber and Crystal Devices: Advances in Materials and Innovations in Device Applications VIII, 920012 (September 5, 2014); doi:10.1117/12.2061806.

12. **Than Singh Saini**, Vinita Dahiya, Ajeet Kumar, Ravindra Kumar Sinha, "Design and analysis of large-mode-area microstructured polymer optical fibre with single-mode operation," *Proc. SPIE* 9200, Photonic Fiber and Crystal Devices: Advances in Materials and Innovations in Device Applications VIII, 92000H (September 5, 2014); doi:10.1117/12.2061825;

13. Amira Baili, Rim Cherif, **Than Singh Saini**, Ajeet Kumar, Ravindra Kumar Sinha, Mourad Zghal, "2-10 μm supercontinuum broadening using a highly nonlinear chalcogenide microfiber for mid-IR applications," *Proc. SPIE* 9200, Photonic Fiber and Crystal Devices: Advances in Materials and Innovations in Device Applications VIII, 92000S (September 5, 2014); doi:10.1117/12.2061848.

14. Amira Baili, Rim Cherif, Amine Ben Salem, **Than Singh Saini**, Ajeet Kumar, Ravindra Kumar Sinha, Mourad Zghal, "Design of single-polarisation single-mode photonic nanowire," *Proc. SPIE* 9170, Nanoengineering: Fabrication, Properties, Optics, and Devices XI, 917014 (August 28, 2014); doi:10.1117/12.2061887.

15. **Than Singh Saini**, Ajeet Kumar, Ravindra Kumar Sinha, "Supercontinuum broadening in a highly nonlinear chalcogenide photonic crystal fiber," Siegman Internation School on Lasers, Stanford University, USA, 03 -08 August 2014.

16. **Than Singh Saini**, Ajeet Kumar, Ravindra Kumar Sinha, "Design and Analysis of Large Mode Area Photonic Crystal Fiber with Low Bend Loss," *Proc*. International Conference on Optics & Optoelectronics (ICOL-2014), (XXXVIII Symposium of Optical Society of India), OSI Golden Jubilee Celebration Conference, Instruments Research and Development Establishment (IRDE), Dehradun, Uttarakhand, 5^{th} – 8^{th} March 2014, Paper ID: PP-FIO-19, pp. 94, INDIA

17. Amira Baili, **Than Singh Saini**, Rim Cherif, Ajeet Kumar, Mourad Zghal and Ravindra Kumar Sinha, "Mid-IR supercontinuum broadening in a highly nonlinear As_2Se_3 nanofiber with low confinement loss", *Proc*. International Conference on Optics & Optoelectronics (ICOL-2014), (XXXVIII Symposium of Optical Society of India), OSI Golden Jubilee Celebration Conference, Instruments Research and Development Establishment (IRDE), Dehradun, Uttarakhand, 5-8 March 2014, Paper ID: OP-FIO-7, pp. 67, INDIA ***(Received Best Paper Presentation Award)***

18. **Than Singh Saini**, Ajeet Kumar, Ravindra Kumar Sinha, "FEM Analysis of Single-Mode Microstructured Polymer Optical Fiber", SPIE- Winter School on Photonics, 26-29 Dec. 2013, Indian Institute of Science Education and Research (IISER)- Kolkata, INDIA ***(Received Best Paper Presentation Award)***
19. **Than Singh Saini**, Ajeet Kumar, Ravindra Kumar Sinha, "Two-core photonic crystal fiber with zero intermodal dispersion at 1.064 μm wavelength", Workshop on Recent Advances in Photonics (WRAP), 17-18 Dec. 2013, IIT Delhi, INDIA
20. Vinita Dahiya, **Than Singh Saini**, Ajeet Kumar, Vipul Rastogi, and Ravindra Kumar Sinha, "Large-core single-mode trench assisted leaky channel waveguide for high-power applications", *Proc. SPIE* 8847, Photonic Fiber and Crystal Devices: Advances in Materials and Innovations in Device Applications VII, 88471P (September 25, 2013); doi:10.1117/12.2023466.
21. **Than Singh Saini**, Ajeet Kumar, Vipul Rastogi, and Ravindra Kumar Sinha, "Selectively filled large-mode-area photonic crystal fiber for high power applications", *Proc. SPIE* 8847, Photonic Fiber and Crystal Devices: Advances in Materials and Innovations in Device Applications VII, 88471Q (September 25, 2013); doi:10.1117/12.2023472.
22. **Than Singh Saini**, Ajeet Kumar, Vipul Rastogi, Ravindra Sinha,"Leaky Channel waveguide for Large-Mode-Area Extended Single-Mode Operation," International Conference on Recent Trends in Applied Physics & Material Science, RAM-13, AIP Conf. Proc. **1536**, 1205-06 (2013).
23. **Than Singh Saini**, Ajeet Kumar, Ravindra Kumar Sinha, Ajeet Kumar, Vipul Rastogi, Ravindra Sinha, "Multi-trench channel waveguide for large-mode-area single-mode operation," *Proc.* International Conference on Fiber Optics & Photonics- Photonics-2012, OSA Technical Digest, paper M2A.6, IIT Madras, INDIA. http://dx.doi.org/10.1364/PHOTONICS.2012.M2A.6

CONTENTS

Certificate i

Acknowledgements v

Abstract vii

List of Publications ix

Contents xiii

List of Figures xvii

List of Tables xxv

List of Abbreviations xxvii

1. Introduction 1-10

2. Design of Asymmetric Large Mode Area Photonic Crystal Fibers with Single Mode Operation 11-21

2.1. Introduction 11

2.2. Proposed LMA PCF Structure 12

2.3. Method of Analysis 13

2.4. Numerical Results and Discussion 14

2.5. Tolerance Analysis 20

2.6. Conclusions 20

3. Triangular Core Large Mode Area Photonic Crystal Fibers 23-35

3.1. Introduction 23

3.2. TC LMA PCF Geometry-I 24-29

3.2.1. Results and discussion 25

3.2.2. Tolerance analysis of geometry-I 29

3.3. TC LMA PCF Geometry-II 29-35

3.3.1. Results and discussion 30

3.3.2. Tolerance analysis of geometry-II 34

3.4. Conclusions 35

4. Large Mode Area Multi-trench Leaky Channel Waveguide 37-47

4.1. Introduction 37

4.2. Proposed Channel Waveguide Design 38

4.3.	Numerical Results and Discussions	40-46
	4.3.1. Effect of the cladding parameters	43
	4.3.2. Effects of the core parameters	44
	4.3.3. Extended single-mode operation	46
4.4.	Conclusions	46
5.	**Supercontinuum Generation in Photonic Crystal Fibers**	49-69
5.1.	Introduction	49
5.2.	Method of Analysis	52-55
	5.2.1. Linear characteristics of PCF structure	52
	5.2.2. Nonlinear characteristics of PCF structure	53
5.3.	Design of Triangular Core PCF	55-62
	5.3.1. Results and discussion	55
	5.3.2. Tolerance analysis of TC PCF structure	62
5.4.	Design of Triangular Core Graded Index PCF	62-68
	5.4.1. Results and discussion	63
	5.4.2. Tolerance analysis of TCGI PCF structure	67
5.5.	Conclusions	69
6.	**Equiangular Spiral Photonic Crystal Fiber for Supercontinuum Generation**	71-76
6.1.	Introduction	71
6.2.	Design of Proposed ES PCF Structure	72
6.3.	Numerical Results and Discussion	73
6.4.	Conclusions	76
7.	**Dispersion Engineered Rib Waveguide for Supercontinuum Generation**	77-85
7.1.	Introduction	77
7.2.	Proposed Rib Waveguide Structure	78
7.3.	Numerical Results and Discussion	80
7.4.	Tolerance Analysis of Rib Waveguide	84
7.5.	Conclusions	85
8.	**Tunable Slow Light Generation in Specialty Optical Fibers**	87-100
8.1.	Introduction	87
8.2.	Principle of Slow Light Based on SBS	89

8.3. Slow Light Generation in Er-Doped Tellurite Fiber 91-93
8.3.1. Results and discussion 91
8.4. Slow Light Generation in Undoped Tellurite Fiber 93-94
8.4.1. Results and discussion 93
8.5. Slow Light Generation in Single Mode PCF 95-99
8.5.1. Condition for single mode operation 95
8.5.2. Results and discussion 96
8.6. Conclusions 99

9. Concluding Remarks and Scope for Future Work 101-102

References 103-116

Brief Bio-Data of the Author 117

LIST OF FIGURES

2.1. The transverse cross-section view of proposed LMA PCF. 12

2.2. Variation of the bend losses of LP_{01} and LP_{11} modes and the effective mode area of LP_{01} mode on pitch (Λ) of the structure at 1.064 µm wavelength with d_1 = 16 µm, $d_2 = d_3$ = 6 µm n_f = 1.448 and bend radius, R = 30 cm. 15

2.3. Variation of the bend losses of LP_{01} and LP_{11} modes and the effective mode area of LP_{01} mode on d_1 at 1.064 µm wavelength with Λ = 21 µm, $d_2 = d_3$ = 6 µm n_f = 1.448 and bend radius, R = 30 cm. 16

2.4. Variation of the bend losses of LP_{01} and LP_{11} modes and the effective mode area of LP_{01} mode on d_2 at 1.064 µm wavelength with Λ = 21 µm, d_1 = 16 µm, d_3 = 6 µm, n_f = 1.448 and R = 30 cm. 17

2.5. Variation of the bend losses of LP_{01} and LP_{11} modes and the effective mode area of LP_{01} mode on d_3 at 1.064 µm wavelength with Λ = 21 µm, d_1 = 16 µm, d_2 = 6 µm, n_f = 1.448 and R = 30 cm. 17

2.6. Variation of bend losses of LP_{01} and LP_{11} modes and the effective mode area of LP_{01} mode on the refractive index of fluorine doped fused silica rods (i.e. n_f) at 1.064 µm wavelength, when Λ = 21 µm, d_1 = 16 µm, $d_2 = d_3$ = 6 µm and R = 30 cm. 18

2.7. Variation of bend losses of LP_{01} and LP_{11} modes and the effective mode area of LP_{01} mode on the bending radius (i.e. R) at 1.064 µm wavelength, when Λ = 21 µm, d_1 = 16 µm and $d_2 = d_3$ = 6 µm. 19

2.8. The surface plot of (a) LP_{01} and (b) LP_{11} mode; when proposed PCF is in straight state; (c) LP_{01} and (d) LP_{11} mode when proposed PCF is bend with 30 cm bend radius at 1.064 µm wavelength; with Λ = 21 µm, d_1 = 16 µm, $d_2 = d_3$ = 6 µm and n_f = 1.448. 19

3.1. The transverse cross-sectional view of proposed TC LMA PCF geometry-I. 24

3.2. The variation of bending loss of LP_{01} & LP_{11} modes and the effective mode area of LP_{01} mode with Λ (when d_0 =14 µm, d_1 =10 µm, R = 20 cm, n_f = 1.4462 and λ = 1.064 µm). 25

3.3. The variation of bend loss of LP_{01} and LP_{11} mode and the effective mode area of LP_{01} mode with d_0 (when Λ = 23 µm, d_1 =10 µm, R = 20 cm, n_f = 1.4462 and λ = 1.064 µm). 26

3.4. The variation of bending loss of LP_{01} and LP_{11} mode and the effective mode are of LP_{01} mode with d_1 (when Λ = 23 µm, d_0 =14 µm, R = 20 cm, n_f = 1.4462 and λ = 1.064 µm). 26

3.5. The variation of bending loss of LP_{01} and LP_{11} mode and the effective mode are of LP_{01} mode with R (when Λ = 23 µm, d_0 =14 µm, d_1 =10 µm, n_f = 1.4462 and λ = 1.064 µm). 27

3.6. Electric field distribution of (*a*) LP_{01} mode, (*b*) LP_{11} mode, when proposed PCF is in straight state; (*c*) LP_{01} mode, (*d*) LP_{11} mode when proposed PCF is in bend state with bend radius of 20 cm in x-direction at operating wavelength of 1.064 µm. 28

3.7. The transverse cross-section of the proposed TC LMA PCF geometry-II. 29

3.8. Effect of n_f on (a) the bending loss and (b) Effective mode area. 30

3.9. The variation of effective mode area of LP_{01} mode and bending losses of LP_{01} and LP_{11} modes with fiber pitch (Λ). 32

3.10. The variation of the effective mode area of LP_{01} mode and the bending losses of LP_{01} and LP_{11} modes with d_1. 33

3.11. The variation of the effective mode area of LP_{01} mode and the bending losses of the LP_{01} and LP_{11} modes with d_2. 33

3.12. The variation of the effective mode area of LP_{01} mode and the bending losses of the LP_{01} and LP_{11} modes with bending radius, *R*. 34

3.13. Contour plot of LP_{01} and LP_{11} at optimized parameters (i.e. d_1 = 10 µm, d_2 = 3.6 µm, Λ = 20 µm, n_f = 1.4474 and bending radius, *R* = 15 cm) 34

4.1. Transverse cross-sectional view of the proposed large-core size channel waveguide structure. 39

4.2. Representation of various profiles of the multi-trench cladding according to the power–law expression Eq (1). 40

4.3. Effect of the profile parameter *q* on the effective indices of the first two modes of the waveguide at 1.55 µm wavelength when *a* =5 µm, *b* = 25 µm, *h* = 10 µm, *d* = 1 µm Λ = 6 µm and *t* = 4 µm. 41

4.4. Effect of the profile parameter *q* on the leakage losses of the first two modes of the waveguide at 1.55 µm wavelength when *a* =5 µm, *b* = 25 µm, *h* = 10 µm, *d* = 1 µm, Λ = 6 µm and *t* = 4 µm. 42

4.5. Normalized electric fields of the (*a*) E_{11}^x mode, (*b*) contour plot of the E_{11}^x mode, and the contour plot of the (c) E_{21}^x mode; when *a* =5 µm, *b* = 25 µm, *h* = 10 µm, *q* = 0.5, *d* = 1 µm, Λ = 6 µm and *t* = 4 µm and λ = 1.55 µm. 42

4.6. The effect of the cladding parameter b on the leakage losses of the first two modes of the waveguide structure at 1.55 µm wavelength; when *a* =5 µm, *q* = 0.5, *h* = 10 µm, *d* = 1 µm, Λ=6 µm and *t*=4 µm. 44

4.7. The effect of the cladding parameter *t* on the leakage losses of the first two modes of the waveguide at 1.55 µm wavelength; when *a* = 5µm, *b* = 25 µm, *h* = 10 µm, *q* = 0.5, *d* = 1 µm and Λ = 6 µm. 44

4.8. The effect of the core parameter *h* on the Leakage losses of the first two modes of the waveguide at 1.55 µm wavelength when *a* = 5 µm, *b* = 25 µm, *t* = 4 µm, *q* = 0.5, *d* = 1 µm and Λ = 6 µm. 45

4.9. The effect of the core parameter *a* on the Leakage losses of the first two modes of the waveguide at 1.55 µm wavelength when *b* = 25 µm, *h* = 10 µm, *q* = 0.5, *t* = 4 µm, *d* = 1 µm, and Λ = 6 µm. 45

4.10. The spectral variation of leakage losses on the first two modes of the waveguide when a = 5 μm, b = 25 μm, h = 10 μm, t = 4 μm, q = 0.5, d = 1 μm and Λ = 6 μm. 46

5.1. (a) The transverse cross-section of the proposed TC PCF structure; (b) The electric field distribution of the propagating mode at 4.5 μm. 55

5.2. Influence of the pitch (Λ) on dispersion characteristics of proposed structure while keeping other parameters fixed (*i.e.* d_1= 420 nm and d_2 = 820 nm). 56

5.3. Influence of the hole diameter (d_1) on dispersion characteristics of proposed structure while keeping other parameters fixed (i.e. Λ = 1.2 μm and d_2 = 820 nm). 57

5.4. Influence of the hole diameter (d_2) on the dispersion characteristics of proposed structure while keeping other parameters fixed (*i.e.* Λ = 1.2 μm and d_1 = 430 nm). 57

5.5. The confinement loss of propagating mode of proposed TC PCF when Λ = 1.2 μm, d_1 = 430 nm and d_2 = 900 nm. 58

5.6. The variation of effective mode area of propagating mode and corresponding nonlinear coefficient of proposed TC PCF with optimized parameters. 58

5.7. Tolerance study of d_1: (a) The effect on the effective mode index with ±1% deviation in d_1; (b) the effect on the effective mode area with ±1% deviation in d_1. 58

5.8. Broadening of output spectra obtained at various lengths of TC PCF when peak power of incident pulse = 700 W and pulse duration = 50 fs. 59

5.9. Influence of input peak power on the broadening of output spectra with 50 fs incident pulse in 6 mm length of TC PCF. 60

5.10. Influence of full-width at half maximum of the input pulse on the broadening of output spectra with 700 W peak power in 6 mm length of PCF. 61

5.11. (*a*) The transverse cross-section of proposed TCGI PCF; (*b*) the electric field distribution of propagating mode in PCF at 4.1 μm. 63

5.12. The effect of the diameter of the air holes in first ring (*i.e.* d_1) on chromatic dispersion profile while keeping other parameters fixed as: d_2 = 700 nm, d_3 = 800 nm, d_4 = 900 nm and Λ = 1000 nm. 64

5.13. The effect of the diameter of the air holes in second ring (*i.e.* d_2) on chromatic dispersion profile while keeping other parameters fixed as: d_1 =420 nm, d_3 =800 nm, d_4 =900 nm and Λ =1000 nm. 64

5.14. The chromatic dispersion characteristic of proposed TCGI PCF structure with optimized parameters (*i.e.* d_1 = 420 nm, d_2 = 700, d_3 = 800 nm, d_4 = 900 nm and Λ = 1000 nm). 65

5.15. The confinement loss of proposed triangular-core graded-index photonic crystal fiber structure with optimized parameters (*i.e.* d_1 = 420 nm, d_2 = 700, d_3 = 800 nm, d_4 = 900 nm and Λ = 1000 nm). 66

5.16. The variation of effective mode area of propagating mode and corresponding nonlinear coefficient of proposed triangular-core graded-index photonic crystal fiber with optimized parameters (*i.e.* d_1 = 420 nm, d_2 = 700, d_3 = 800 nm, d_4 = 900 nm and Λ = 1000 nm). 66

5.17. Spectral broadening of supercontinuum spectra from various length of PCF; when 50 fs laser pulses with peak power of 3.5 kW launched at proposed triangular-core graded-index PCF structure. 67

5.18. Broadening of output spectra from 5 mm long TCGI PCF obtained at various values of T_{FWHM} when peak power of incident pulses = 3.5 kW. 68

6.1. The transverse cross-sectional view of the proposed ES PCF structure. 72

6.2. Dispersion characteristics of proposed ES PCF with r_0. 73

6.3. Dispersion characteristics of proposed ES PCF with r_h. 74

6.4. Confinement loss of proposed ES PCF structure. 74

6.5.	Spectral variation of effective mode area of propagating mode and nonlinear coefficient of proposed ES PCF structure.	75
6.6.	Supercontinuum generation at different lengths of ES PCF pumped at 3.5 μm.	75
7.1	(*a*) The transverse cross-sectional view of proposed rib waveguide structure; (*b*) the normalized electric field distribution of propagating mode in the core region at pump wavelength.	79
7.2	The effect of the geometrical parameter '*t*' on chromatic dispersion profile while keeping other parameters fixed as: a = 1 μm, h = 1 μm.	80
7.3	The effect of the core height (*i.e*. *h*) on chromatic dispersion profile while keeping other parameters fixed as: a = 1 μm, t = 0.75 μm.	81
7.4	The effect of the core width (*i.e*. 2*a*) on chromatic dispersion profile while keeping other parameters fixed as: t = 0.75 μm, h = 1 μm.	81
7.5	The chromatic dispersion characteristic of proposed rib waveguide structure with optimized parameters (*i.e*. a = 1.0 μm, t = 0.75 μm, h = 1 μm).	82
7.6	The variation of effective mode area of propagating mode and corresponding nonlinear coefficient of proposed rib waveguide with optimized parameters (*i.e*. a = 1.0 μm, t = 0.75 μm, h = 1 μm).	83
7.7	Spectral broadening of supercontinuum spectra from 4 mm long rib waveguide at different peak power; when 50 fs laser pulses at 2.5 μm launched at proposed rib waveguide structure.	83
7.8	Broadening of output spectra from 4 mm long rib waveguide obtained at various values of pulse width (T_{FWHM}) when peak power of incident pulses = 1.1 kW.	84
8.1	Schematic of the principle of stimulated Brillouin scattering in PCF.	89

8.2	Brillouin gain of the fiber with frequency difference between pump and signal $(\omega_p - \omega_s)$ in two meter *E*r-doped tellurite fiber.	92
8.3	Effect of pump power on Brillouin gain.	92
8.4	Time delay as a function of real fiber length.	93
8.5	Time delay as a function of pump power.	93
8.6	Brillouin gain of the fiber against the frequency difference between pump and signal $(\omega_p - \omega_s)$ in 100 meter long undoped tellurite fiber with 10 mW pump power.	94
8.7	Brillouin gain as a function of pump power.	94
8.8	Time delay per unit power with real fiber length.	94
8.9	Total time delay with pump power.	94
8.10	Transverse cross-sectional view of the proposed highly nonlinear photonic crystal fiber structure.	95
8.11	Variation of 'V' parameter of the proposed PCF with d/Λ.	96
8.12	Electric field distribution of fundamental mode with d/Λ = 0.4 at 1.06 µm wavelength.	96
8.13	Influence of the effective mode area and nonlinear coefficient with d/Λ.	97
8.14	Maximum allowable pump power as a function of d/Λ.	97
8.15	Confinement loss of the proposed PCF structure as a function of d/Λ.	98
8.16	Influence of d/Λ on Brillouin gain in proposed PCF structure with 100 mW pump power.	98
8.17	Influence on time delay per unit length with incident pump power.	98

LIST OF TABLES

3.1.	The optimized structural parameters of proposed TC PCF.	29
5.1.	Geometrical parameters of proposed TC PCF.	61
5.2.	Input pulse parameters for proposed TC PCF.	61
5.3.	Geometrical parameters of proposed TCGI PCF.	68
5.4.	Input pulse parameters for proposed TCGI PCF.	68
7.1.	Geometrical parameters of proposed rib waveguide.	85
7.2.	Input pulse parameters for proposed rib waveguide.	85
8.1.	Maximum allowable pump power (P_{max}).	99
8.2.	Time delay in 1 meter long proposed PCF.	99

LIST OF ABBREVIATIONS

CW	:	*Continuous Wave*
EDFA	:	*Erbium Doped Fiber Amplifier*
EMA	:	*Effective Mode Area*
ES	:	*Equiangular Spiral*
FEM	:	*Finite Element Method*
FWHM	:	*Full Width at Half Maximum*
FWM	:	*Four Wave Mixing*
GNLSE	:	*Generalized Nonlinear Schrödinger Equation*
GVD	:	*Group Velocity Dispersion*
LMA	:	*Large Mode Area*
NA	:	*Numerical Aperture*
OCT	:	*Optical Coherence Tomography*
OWB	:	*Optical Wave Breaking*
PCF	:	*Photonic Crystal Fiber*
PML	:	*Perfectly Matched Layer*
RK4IP	:	*Fourth order Runge Kutta Interaction Picture*
SBS	:	*Stimulated Brillouin Scattering*
SCG	:	*Supercontinuum Generation*
SM	:	*Single Mode*
SPM	:	*Self Phase Modulation*
SRS	:	*Stimulated Raman Scattering*
TC	:	*Triangular Core*
TCGI	:	*Triangular Core Graded Index*
XPM	:	*Cross Phase Modulation*
ZDW	:	*Zero Dispersion Wavelength*

CHAPTER 1

Introduction

Albert Einstein in 1917 proposed the theoretical concept to achieve highly coherent and monochromatic beam of light. The first experimental demonstration of the LASER (Light Amplification by Stimulated Emission of Radiation) was carried out by T. H. Maiman in 1960 [1]. A synthetic ruby rod was used as an active medium in this laser. After the demonstration of the Ruby laser, various efforts have been made to increase the power of the output beam. There are various applications of high power lasers in different diverse fields such as defense, biological sciences, industry and scientific research. In industrial applications such as cutting, welding, drilling and marking, highly intense lasers are required with output power of 10 W – 10 kW. To increase the power level of the lasers different types of active medium (i.e. solid, liquid and gas) can be used. Ali Jawan invented a continuous wave (CW) laser by employing mixture of He and Ne gases as a gain medium [2]. In 1964, C. K. N. Patel invented more powerful carbon dioxide (CO_2) gas laser [3]. Willian Bridges in 1971 developed an Argon-Ion laser with output power of 1 – 20 W which makes it attractive for various applications such as lithography, retinal surgery and pumping [4]. Mercury ion laser, Krypton ion laser and Excimer laser are the few more important gas lasers. The drawback of these gas lasers include their regular cooling system and bulky in size. Solid state lasers are relatively compact in size. By providing suitable pumping, Nd: YAG rod laser is able to generate several kilowatts of power but limited to ~10 kW.

Solid-state lasers are having rod shaped rare earth doped active medium. The output beam quality of conventional rod-type lasers degrade due to power induced thermo-optical problems such as thermal lensing and thermally induced birefringence. To mitigate the thermal effects, various special types of architectures of lasing materials have been developed [5-7]. Among all these special designs, the fiber laser concept is most

suitable due to following reasons: i) the heat generated by lasing process is distributed over a long fiber length; ii) large surface to active volume ratio of fiber which leads to outstanding heat dissipation. Due to its special geometry, the fibers doped with rare earth elements have intrinsic property to eradicate the thermo-optical problems. Fiber has a good heat dissipation property due to its large surface to active volume ratio which is helpful to restrain the thermal lensing effect in fibers [8].

Since the fiber leads to the insignificant thermal distortion to the optical beam, the beam quality of the fiber laser output becomes power independent. In the fiber laser systems, the beam quality is defined by the fiber structure. In the fibre geometry it is possible to propagate the pump and laser radiation simultaneously inside the active doped core region, which maintains the intensity of the optical beam over the entire length of the fibre and is not limited to the Rayleigh length. Thus, the fibre lasers can be a good alternative of the bulk solid state lasers for numerous applications.

However, the idea of the development of fiber lasers and amplifiers by doping of rare earth elements is not new. This concept was first reported by *Snitzer* in 1961 [9]. After that Nd-doped fiber lasers were developed. Initially, the efficiency of the first Nd-doped fiber laser was very low and could only work in spatial multimode regime [10]. The longitudinal pumping was used to improve the efficiency of fiber laser [11]. In 1987, *Mears et a*l. demonstrated a high gain erbium doped fiber amplifier (EDFA) operating at 1.54 μm [12]. An EDFA has made significant contribution to the long distance optical communication and became the standard for long distance communication. However, EDFA does not go well with the high power fiber lasers and amplifiers where the high power density damages the fibre. Recently, the output power from fiber laser up to 101.3 kW at wavelength 1070 nm has been presented by *Shcherbakov* [13]. However, the challenges still exist. The performances of such laser systems are limited by the various unwanted nonlinear optical effects such as self phase modulation (SPM), cross phase modulation (XPM), four wave mixing (FWM), optical wave breaking (OWB), stimulated Brillouin scattering (SBS) and stimulated Raman scattering (SRS). At high power level, reduction in optical damage threshold due to tight confinement of light over the long interaction length in the fibers is also a serious problem. The temporal, spectral and spatial characteristics of the laser emission can be destroyed by these unwanted nonlinear effects.

To avoid the nonlinear effects at high power level, the preferred way is to use large-mode-area (LMA) fibers which allow a dramatic reduction of the guiding intensity. The large-mode-area can be achieved by increasing the core size of the fiber. However, too much large core size can allow the higher order modes to propagate through it. In multimode fiber laser the mode competition and intermodal dispersion can destroy the output of the fiber laser. Single mode (SM) operation provides good beam quality at the output of the fiber lasers. Therefore, LMA fibers or waveguides with single-mode operation are the preferred designs for high power delivery devices such as high power fiber lasers, amplifiers, high-power microwave detection and high-efficiency photovoltaic applications. Tremendous efforts have been made earlier to increase the effective-mode-area in fiber geometries with effective single-mode operation for applications in optical communications and high power fiber lasers and amplifiers [14-32]. The effective mode area of fiber can be enhanced by controlling the refractive index profile in the core or the relative index difference between core and cladding [16-18]. Using single material photonic crystal fiber is another way to design LMA fiber [19-22]. In most of these approaches, the effective SM operation have been achieved via higher-order mode discrimination techniques such as matched excitation [23], bending of fiber [24], using leaky cladding [25 – 27], resonant filtering [27, 28] and delocalization of higher order modes [29].

In matched excitation technique, the seed radiation is injected carefully in such a way that only fundamental mode of the fiber is excited. Mode matching technique is used for few-mode fibers. However, this technique of higher order mode discrimination is not efficient for high-power fiber lasers and amplifiers. Bending the fiber is another common technique for higher order mode discrimination. Bending introduces a differential propagation loss (bending loss) between the fundamental and higher order modes. Higher order modes can also be discriminate by using multiple leaky cladding of uniform refractive index. Resonant filtering of higher order modes can be achieved by designing the cladding in such a way that the effective indices of cladding modes match with the effective indices of higher order modes. However, realization of fiber based on this technique is more challenging. Higher order modes delocalization is used for very large mode area rod type fiber. It includes the concept that due to relatively larger overlap of the fundamental with potentially doped core region in comparison to higher order modes,

the higher-order modes get poorly amplified. This difference in the overlap leads to the discrimination of higher-order-modes.

Now-a-days a lot of attention has been made to design and analyses of special kinds of optical fibers such as photonic crystal fibers (PCFs) or holy fibers or microstructured optical fibers because of their unique properties which can not be achieved using conventional fibers [19-22, 33]. In 1996, after trying various different approaches, the first silica-air solid-core PCF (single material fiber having air holes in its cladding region) was demonstrated by staking 216 silica capillary [34]. Later this led to the discovery of endlessly single-mode PCF [35]. During the year of 2000, based on shape, size, position, arrangement and orientation of air holes in the cladding region, various PCF designs have been explored such as dispersion compensating PCF, multi-core PCF, polarization-maintaining PCF and rare-earth doped PCF laser [36 – 38]. By using the asymmetric design of air holes and/or the doped dielectric rods in air holes of PCF structure, researchers are able to control the bend loss of photonic crystal fibers which make it applicable in Fiber-To-The-Home technology [39]. The guiding mechanism of these PCFs is based on total internal reflection and photonic band gap guidance. For compact and portable high power devices we need to maintain the size of the devices as small as possible. For this purpose the LMA PCF has to be bent in the loops. Although in comparison to the conventional optical fibers the bending loss of PCF is very low. But, for LMA PCF the core size is very large (~ 40 μm or more) which increases the bend loss. The issue of bend loss of LMA PCF is tried to solve as a part of the research work in this thesis.

For several other applications such as optical coherence tomography (OCT), frequency comb generation, security and detection of bio-molecules a white light (broadband) laser sources are required [40 – 43]. Incandescent and fluorescent lamps have broad spectrum (>1000 nm) but limited by the low intensity, lack of spatial coherence and ordinary beam quality. However, laser sources have high spatial coherence and very high brightness which enables optimum coupling to the fiber and outstanding single-mode beam quality. But these laser systems are limited by their monochromatic nature. If we required more than one wavelength extra lasers of a specific wavelength are needed to cover a broad spectrum. Supercontinuum generation (the creation of broadband spectral components when an intense laser pulse passes through a highly nonlinear medium) bridges this gap by providing ultra broadband white-light spectrum, single-

mode beam characteristics, excellent pointing stability and brightness of a laser. The phenomenon of supercontinuum generation (SCG) has been reported first time in glass in the year of 1970 [44]. The spectral brightness of supercontinuum is million times brighter than that of the conventional light sources. SCG is the result of combined response of various nonlinear mechanisms including SPM, SRS, OWB, FWM and XPM along with the dispersion properties of the medium. Spectral broadening due to SPM is due to the maximum phase shift ($\phi_{max} = \gamma P_0 L_{eff}$) induced by SPM, where γ is the nonlinear coefficient of the medium, P_0 is the peak power of input pulse and L_{eff} is the effective length of medium. SRS creates the new frequency components on the longer wavelength side only. However, FWM is responsible for generating sidebands on both sides of the pulse spectrum when phase matching condition is satisfied.

The mid-infrared spectral domain ranging from 2 – 15 μm is mainly important because of not only it contains two important windows (3 – 5 μm and 8 – 13 μm) in which the earth's atmosphere is relatively transparent but also the strong characteristic vibration transitions of most of the molecules in this domain [42]. Mid-infrared molecular 'fingerprint region' is applicable in various important applications in different diverse fields such as medical, industry, security and astronomy [45 – 49]. Therefore, researchers are trying very hard to achieve mid-infrared broadband supercontinuum spectrum in various conventional, photonic crystal fibers [50 – 53] and waveguide geometries [54 – 60]. Among all non-silica glasses, the chalcogenide glasses are excellent candidates for mid-infrared region because some of its compositions possess optical transparency upto 25 μm in this region [61]. The As_2Se_3 glass has shown excellent optical transparency between 0.85 – 17.5 μm with attenuation coefficient of less than 1 cm^{-1} [61]. In addition to broadband mid-infrared transmission window, chalcogenide glasses have also very large linear and nonlinear refractive indices which make them promising candidates for mid-infrared SCG [62]. However, the spectral broadening of supercontinuum spectrum spanning 2 – 15 μm range in fiber or waveguide geometries has not been reported yet.

In this thesis, some novel PCF and waveguides geometries for the applications i) in which the nonlinearity need to be eliminated (such as high power fiber lasers and amplifiers); ii) in which the nonlinearity need to be enhanced (such as supercontinuum and slow light generation) have been reported. LMA PCF designs for high power fiber lasing and amplification have been achieved by tailoring the size of the air holes and introducing down doped fused silica rods in the selective air holes in the cladding region

of PCF. In the case of LMA waveguide design the trenches of lower refractive index in cladding region have been introduced in such a way that all the propagating modes become leaky. The basic principle behind the cladding profiles is to introduce the high leakage loss to the higher order modes while nominal leakage loss to the fundamental mode, which makes the designs effectively single-moded. All the PCF and waveguide designs which are applicable for supercontinuum and slow light generation have been designed such that the propagating mode is strongly confined in small core of the structure, which makes the designs highly nonlinear. Since dispersion is one of the most important parameter in the broadening of supercontinuum spectrum, PCF with all-normal dispersion characteristic is desirable for smooth and coherent SCG [63]. Therefore, PCF/waveguide designs have been engineered to achieve all-normal dispersion profile. Dispersion, leakage losses and effective area of the modes have been calculated by employing commercially available software 'COMSOL Multiphysics' based on full vectorial finite element method (FEM). Broadening of supercontinuum spectrum has been simulated by solving the generalized nonlinear Schrödinger equation (GNLSE).

Outline

The outcome of the research work carried out during the four years of PhD has been arranged in nine chapters of this thesis. First chapter is the Introduction, which presents the motivation for the designs of specialty fibers and waveguides and brief summary of literature review of the topic.

Chapter 2 reports a design of an asymmetric PCF for low bend loss large-mode-area with effective single-mode operation at 30 cm bend radius. The design works on the principle of bend induced mode filtering. The proposed fiber can be designed by i) introducing down doped material rods in place of nine air holes of inner ring near the core of structure; ii) increasing the diameter of rest of the three air holes of the same ring in the direction of bending. These three air holes together with nine down doped material rods control the mode field inside the core region and hence the bending losses of the modes. The single-mode operation is ensured by introducing high bend loss for first higher order mode and very low bend loss for fundamental mode. Numerical results show that effective-single-mode operation can be ensured with mode area as large as 1530 μm^2 at bend state with bend radius of 30 cm. The proposed PCF structure with such a large-

mode-area can have potential applications in compact high power delivery devices such as, high power fiber lasers and amplifiers

Chapter 3 provides two designs of triangular core large-mode-area photonic crystal fiber structure which offers low bending loss at 1.064 μm wavelength. One of the photonic crystal fiber structure is optimized for low bending loss even at 15 cm bending radius while other at 20 cm bending radius. The designs work on the principle of bend induced mode filtering. Effects of the design parameters have been numerically investigated using full vectorial finite-element method. In order to improve the effective mode area of fundamental mode along with the differential bending loss, five down-doped material rods have been introduced in place of five air holes in the first ring. And the diameters of rest three air holes are considered relatively larger than that of the others. First structure offers effective-mode-area of propagating mode as large as 875 μm^2 with bending loss of 0.038 dB/m at bend radius of 20 cm. Second structure supports effective mode-area of fundamental mode as large as 794 μm^2 with nominal bend loss of propagating mode 0.064 dB/m at the bend radius of 15 cm. Structures are able to suppress all unwanted nonlinear effects and can be a potential candidate for designing compact high power delivery devices such as high power fiber lasers and amplifiers.

Chapter 4 presents a multi-trench leaky channel waveguide design that supports effective single-mode operation even with large-core size. The proposed waveguide structure has uniform rectangular core and a cladding which is geometrically designed in such a way that all the confined modes become leaky. The effective single-mode operation has been achieved by choosing the geometrical parameters of proposed channel waveguide in such a way that it induces a very large leakage losses for higher order modes while very low leakage loss for fundamental mode. A profile for cladding geometry is considered based on power-law, which is solved by finite element method. By choosing the suitable cladding parameters, proposed channel waveguide structure ensure extended single-mode operation in the wavelength range 1.25 – 2 μm with the rectangular core area as large as 100 μm^2. Such large core area waveguide structure efficiently suppresses unwanted nonlinear optical effects. Proposed channel waveguide structure with large core size is suitable for high power delivery devices such as high power waveguide lasers and amplifiers.

Chapter 5 describes two dispersion engineered triangular-core photonic crystal fiber structures in As_2Se_3 based chalcogenide glass for supercontinuum generation. The first design is optimized for all-normal dispersion profile by tailoring the diameters of air holes in second ring of air holes in the cladding of the structure. Structure offers nonlinear coefficient as high as 5449 $W^{-1}Km^{-1}$ at pump wavelength (*i.e.* 4.5 μm) with effective mode area of 6.15 μm^2. The influences of PCF length, input pulse peak power and full-width at half maximum on output spectral intensity have been investigated. Ultra-broadband SC spectra have been generated in a very small length of PCF with relatively low peak power of incident pulse. Simulated results indicate that the ultra-broadband supercontinuum spectrum extending from 1.9 μm to 10 μm at the -30 dB level can be generated in only 6 mm long PCF with an input pulse peak power of 700 W in femtosecond regime. Second design is optimized for all-normal dispersion profile by taking the size of air holes in increasing order for successive rings. This design of PCF structure offers supercontinuum spectrum spanning 2 – 15 μm with peak power of 3.5 kW at 4.1 μm. Such broadband mid-infrared supercontinuum spectrum is obtained in relatively short length (*i.e.* 5 mm) of PCF, using a sub-harmonic generation source of the mode-locked thulium 50 fs pulsed fiber laser at 4.1μm. To the best of our knowledge the supercontinuum in PCF with such broadband spectra has been reported first time. These highly nonlinear photonic crystal fiber structures can be a good candidate for generating efficient supercontinuum which is applicable for various nonlinear applications such as optical coherence tomography, pump-probe spectroscopy, metrology, gas sensing, food quality control, frequency combs generation and early cancer diagnostics.

Chapter 6 explains the design and analysis of an equiangular spiral (ES) PCF in As_2Se_3 chalcogenide glass for mid-infrared supercontinuum generation. A full vectorial finite element method has been used to investigate the dispersion properties of the proposed fiber. Simulated results show that the proposed ES PCF structure is highly nonlinear with very low and flat dispersion characteristic. Proposed ES PCF structure is able to achieve broadband supercontinuum spectrum with femtosecond laser pulses of very low peak power. This is the first time to our knowledge that a new design of an equiangular spiral photonic crystal fiber in As_2Se_3 chalcogenide glass is used to generate an ultra-broadband, coherent and stable supercontinuum spectrum spanning from 1.2 – 15 μm in only 8 mm fiber length with very low peak power of laser pulses of 500 W at 3.5 μm.

Chapter 7 reports a dispersion engineered As_2Se_3 based chalcogenide rib waveguide which can be used for mid-infrared supercontinuum generation across molecular 'fingerprint region'. Proposed rib waveguide design offers nonlinear coefficient as high as 18250 W^{-1} Km^{-1} with effective mode area of 2.07 μm^2 at 2.5 μm pump wavelength. Supercontinuum spectrum spanning 2 – 15 μm, which not only covers the both atmospheric transparent windows (3 – 5 μm and 8 – 13 μm) in mid-infrared domain but also important molecular 'fingerprint domain', is obtained using only 4 mm long rib waveguide. To the best of our knowledge such broadband mid-infrared supercontinuum spectrum in As_2Se_3 based chalcogenide waveguide geometry is reported first time. Proposed design of rib waveguide has potential for robust, integrated and low cost supercontinuum sources for various applications including optical coherence tomography, frequency comb generation, chemical sensing, food quality control and early cancer diagnostics.

In chapter 8, the theoretical investigation of stimulated brillouin scattering-based tunable slow light in three different designs of (i) Er-doped tellurite fiber, (ii) undoped tellurite fiber and (iii) single mode photonic crystal fibers is provided. Using Er-doped fiber design Brillouin gain up to ~91 dB and time delay of 140 ns can be achieved with 1100 mW pump power in 2 m long fiber. While, using undoped tellurite fiber, Brillouin gain up to ~86 dB and time delay of ~227 ns with 23 mW pump power in 100 m long fiber can be achieved. We have found that Brillouin gain upto ~ 88 dB/m and time delay up to ~137 ns can be obtained from 1 meter long photonic crystal fiber pumped with 100 mW. Simulated results indicate that the time delay in fibers can be tuned with the pump power to obtain tunable slow light features in these fibers. We feel that detailed theoretical investigations and simulations carried out in the study have potential impact in the design and development of slow light-based photonic devices.

Chapter 9 presents the concluding remarks and the future research scope coming up from the current thesis work. In this thesis some novel specialty fiber and waveguide designs have been reported for the applications of high power fiber lasers and amplifiers, supercontinuum generation and tunable slow light generation. For high power applications the PCF and waveguide structures are designed based on the principle of bend induced mode filtering. The designed LMA PCF structures offer effective single-mode operation even with large core size. For supercontinuum generation (white light laser source) we have optimized the triangular core PCF and rib waveguide structures for

all-normal dispersion and large nonlinearity. Ultra broadband spercontinuum spectrum spanning 2 -15 μm is achieved first time in As_2Se_3 chalcogenide glass PCF and rib waveguide geometries. The numerical simulation for tunable slow light in doped and undoped tellurite fibers and As_2Se_3 based photonic crystal fiber geometries is carried out. The LMA PCF and channel waveguide designs presented in this thesis can be extended to active materials to access the actual performance of the device. In the future, the coherence property of supercontinuum spectrum from the proposed PCF and rib waveguide structures can be studied. The light can be further slowed down in graded index PCF structure.

CHAPTER 2

Design of Asymmetric Large Mode Area Photonic Crystal Fiber with Single Mode Operation*

2.1 Introduction

Designing of specialty optical fibers are one of the main exciting research topics because of their unique properties which cannot be achieved in conventional optical fibers [15, 39, 64 – 70]. The nonlinearity and low optical damage threshold arising due to high power density are the major challenges in designing of high power fiber laser systems. This problem can be mitigated by using LMA fiber because the nonlinearity is inversely proportional to the effective-mode-area (EMA). EMA of the fiber can be increased by increasing its core size. But, too much core size makes the fiber multi-moded, which affects the beam quality and the stability of the laser output.

To stripe off all the higher order modes from large-core of the optical fiber various methods are reported in the literature [71, 72]. Earlier, several efforts have been made in this direction using standard silica glass fibers [23 – 27, 73, 74]. It is difficult to achieve very LMA in standard silica fibers because of its large bending loss and limitation on index contrast. However, in case of PCF geometries it can be possible to attain simultaneously both the low bending loss and LMA characteristics. PCFs have large number of degree of freedom than those of standard silica glass fibers. The presence of air holes or lower index material doped silica rods in the cladding region of PCFs allow to have a very low numerical aperture (NA).

*A part of the results presented in this chapter has been submitted to *Optical Fiber Technology*.

Various novel LMA PCF designs have been reported earlier [75 – 79]. A novel type of effectively single-mode holy fiber with large effective-mode-area and low bending loss has been proposed based on the resonance of higher order mode in the outer ring core [75]. An LMA fiber structure with single-mode operation has been proposed using microstructured multi-core instead of a single large-core [76]. *Morasse et al*. proposed a multimode high NA ytterbium doped fiber which is used in single mode operation for high power lasers and amplifiers [77]. LMA leakage channel fibers are also reported in the literature using asymmetric structure with microstructured core [80, 81].

In this chapter an asymmetric design of solid core LMA PCF is presented. The proposed structure offers effective single-mode operation in spite of large core size. The design is based on introducing down doped (*i.e.*, fluorine doped) material rods in place of nine air holes in the opposite direction of bending and having relatively larger air holes in the direction of bending. Our aim is to increase the differential bend loss between the first two modes (*i.e.*, LP_{01} & LP_{11}) of proposed structure.

2.2 Proposed LMA PCF Structure

The transverse cross-sectional view of proposed LMA PCF structure has been shown in the Fig. 2.1.

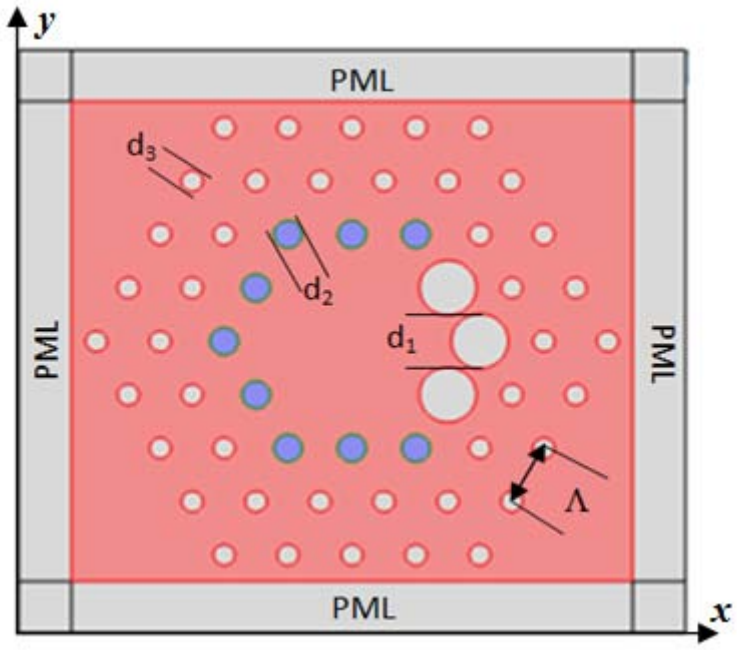

Fig. 2.1: The transverse cross-section view of proposed LMA PCF.

As shown in Fig.2.1, the design is characterized by the air holes arranged in triangular lattice in the silica dielectric. In order to construct the large core, seven air holes from the central part of PCF structure have been removed. The innermost ring located near the core has twelve holes. Out of which, nine air holes have been modified by introducing fluorine doped fused silica rods while rest three air holes are with relative larger diameters along the positive *x*-direction. The pitch is same for all the holes and it is represented by Λ. The diameters of three larger air holes in the first ring are taken as d_1; the diameters of nine fluorine doped diffuse silica rods in the same ring are considered as d_2. The diameters of air holes arranged in outer two rings are taken as d_3. The refractive indices of fluorine doped fused silica rods have been assumed as n_f. The PCF structure is simulated when it is in bent state having bend radius of *R* in positive *x*-direction. The refractive index of background material (*i.e.* fused silica) is taken as 1.45 at 1.064 μm wavelength.

2.3 Method of Analysis

The proposed PCF structure is simulated by well known computational technique finite element method (FEM) [82]. For this purpose we have used commercially available software 'COMSOL Multiphysics'. To calculate the accurate bend loss of the proposed PCF, An anisotropic perfectly matched layer (PML) has been used as a boundary condition [83]. In the bend state of PCF, the refractive index profile of structure gets deformed. In order to calculate bend loss of structure the bent structure is transformed into its equivalent straight structure with equivalent refractive index profile n_{eq}. The equivalent index profile n_{eq} of structure is defined by the following relation [84];

$$n_{eq} = n(x, y) exp\left(\frac{x}{R}\right) \qquad (2.1)$$

where, *R* is the bending radius, *x* is the transverse distance from the centre of the proposed PCF structure, and *n*(*x*, *y*) is the refractive index profile of the structure when it is in straight state.

In the finite element scheme the following Maxwell vector equation has to be solved [85]

$$\nabla \times ([s]^{-1} \nabla \times E) - k_0^2 \, n^2 [s] E = 0 \qquad (2.2)$$

$$[s] = \begin{pmatrix} s_y/s_x & 0 & 0 \\ 0 & s_x/s_y & 0 \\ 0 & 0 & s_x s_y \end{pmatrix} \qquad (2.3)$$

where, E is the electric field vector. $k_0 = \frac{2\pi}{\lambda}$, is the wave number in the vacuum, and λ is the operating wavelength. n is the refractive index, [s] is the PML matrix, s_x and s_y are the PML parameters.

For the PCF structure the solution of the Eq. (2.2) gives the complex propagation constant. The real part of the propagation constant provides the effective index of the mode while the imaginary part of propagation constant gives the bend loss of the mode. Bend loss of the PCF can be calculated by the imaginary part of propagation constant using the following relation [86]

$$L\left(\frac{dB}{m}\right) = \frac{40\,\pi}{\ln(10)\lambda} Im\left(n_{eff}\right) = 8.686 k_0\, Im\left(n_{eff}\right) \quad (2.4)$$

where, $Im(n_{eff})$ is the imaginary part of propagation constant and λ is the free space wavelength in µm.

The effective mode area of propagating mode of PCF structure can be calculated by transverse electric field of mode according to the following equation [41];

$$A_{eff} = \frac{(\iint |E|^2\, dx\, dy)^2}{(\iint |E|^4 dx\, dy)} \qquad (2.5)$$

where, E denotes the transverse electric field vectors.

2.4 Numerical Results and Discussion

An asymmetric PCF design has been presented to realize the bend induced mode filtering keeping in mind that such bending should not introduce significantly high bend loss to fundamental mode. To analyse the proposed LMA PCF structure, initially we have chosen the values of parameters as: d_1=16 µm, d_2 = 6 µm, d_3 = 6 µm, n_f = 1.448, R = 30 cm and λ = 1.064 µm. The effect of various parameters of the structure have been studied and summarized in Figs 2.2 – 2.8.

Figure 2.2 shows the variation of bend losses of the first two modes (*i.e.* LP_{01} & LP_{11}) on pitch (Λ) of the proposed PCF structure. The bend loss of first higher order mode (LP_{11}) is always quite large than that of LP_{01} mode. The bend losses of both the

modes increase on increasing the pitch of proposed structure. The effective mode area of LP_{01} mode is also increases on increasing the value of Λ. This is because of the increment in core size on increasing the value of Λ. Higher the value of pitch larger is the core size, *i.e.* higher is the effective mode area. The bend losses of both the modes increase on increasing the pitch. It is because the index contrast between the core and holy cladding decreases while increasing the value of pitch.

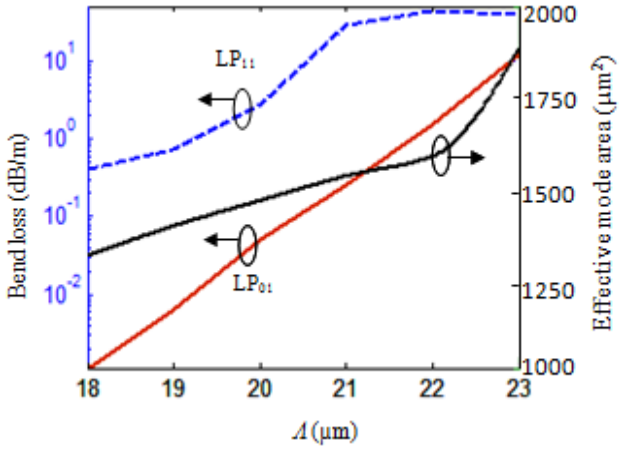

Fig. 2.2: Variation of the bend losses of LP_{01} and LP_{11} modes and the effective mode area of LP_{01} mode on pitch (Λ) of the structure at 1.064 μm wavelength with d_1 = 16 μm, $d_2 = d_3$ = 6 μm n_f = 1.448 and bend radius, R = 30 cm.

It has been observed that the loss of the first higher order mode is smaller than that of other higher order modes for this PCF structure. Therefore, only first two modes (*i.e.* LP_{01} and LP_{11}) have been included in our study to investigate the bend performance of the proposed PCF structure. It is quite evident from the Fig. 2.2 that, if the value of Λ is below 20 μm, the bend loss of both LP_{01} and LP_{11} mode is small. It means, below 20 μm value of Λ, proposed PCF structure would be multi mode even in bent state with 30 cm bend radius. When Λ > 21 μm, the value of bend loss of first higher order mode is larger and fundamental mode also attenuate rapidly.

At Λ = 21μm, the value of bend loss for LP_{01} mode is 0.25 dB/m, while the value of the bend loss of LP_{11} mode is as large as 29.22 dB/m. The bend loss of LP_{11} mode is large enough to leak out from the fiber core while the LP_{01} mode is the guiding mode with a little attenuation. Such a bending can introduce more than 55 dB loss to LP_{11} mode and only 0.47 dB loss to LP_{01} in a single turn of bending. Therefore, the proposed PCF structure would offer effective single-mode operation with effective mode area as large as 1530 μm^2. Using the same parameters in straight state, the proposed structure

offers confinement losses 4.64×10^{-5} dB/m and 1.28×10^{-3} dB/m for LP_{01} and LP_{11} modes respectively with mode area of LP_{01} mode as large as 2388 μm^2. Therefore, the PCF would be multimode at straight state.

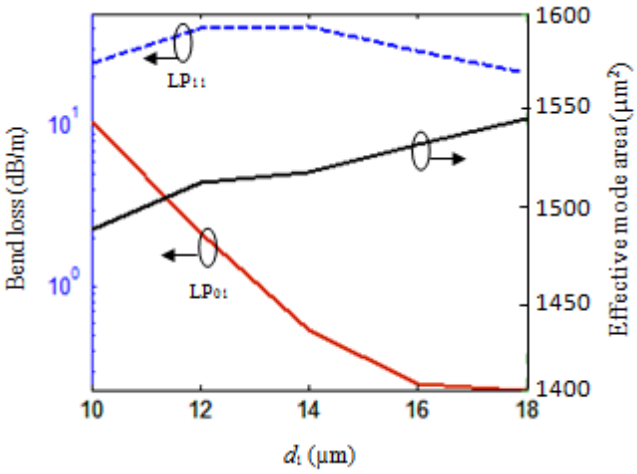

Fig. 2.3: Variation of the bend losses of LP_{01} and LP_{11} modes and the effective mode area of LP_{01} mode on d_1 at 1.064 μm wavelength with Λ = 21 μm, $d_2 = d_3$ = 6 μm n_f = 1.448 and bend radius, R = 30 cm.

Figure 2.3 illustrates the variation of the effective mode area of LP_{01} mode and the bend losses of LP_{01} and LP_{11} modes of the proposed PCF structure with the parameter d_1. The bend losses of LP_{01} and LP_{11} modes decrease on increasing the value of d_1. It is because of the fact that when d_1 increases the index contrast also increases which compel the field to tightly confine within the core, thus, resulting in reduction of bend losses of both the modes. As shown in Fig. 2.3, it is clear that for $d_1 > 14$ μm, the proposed design introduces more than 21 dB/m loss to higher order modes and less than 0.5 dB/m loss to the fundamental mode. Thus, $d_1 > 14$ μm would be favourable for designing the fiber for effective SM operation.

The effects of the diameter of fluorine doped diffuse silica rods (*i.e.* d_2) on single-mode performance of the proposed design have been investigated and presented in Fig. 2.4. The effective mode area of LP_{01} mode and bend losses of LP_{01} and LP_{11} modes decreases on increasing d_2, however, the differential bending loss would remain almost same in the order of magnitude. This property can be used to tune the absolute losses of the modes without much changing the differential loss.

Figure 2.5 shows the effect of cladding parameter d_3 on effective SM operation of the structure. The effective mode area of LP_{01} mode decreases with d_3 and the bend losses of first two modes also decrease very sharply on increasing the value of d_3. This

is due to increment in the index contrast between core and cladding on increasing the value of d_3. However, care should be taken while choosing this parameter as bending loss sharply changes with this parameter. For example: at d_3 = 4 µm, even LP_{01} mode suffers from 2.7 dB/m bending loss which is large enough to leak even LP_{01} mode. Further increase in d_3 reduces the bending losses of both the modes; however, at d_3 beyond 7 µm, the bending loss of LP_{11} mode becomes even smaller than 7 dB/m. In both the cases structure would not be able to show SM operation. Thus for given design parameters 4 µm < d_3 < 7 µm would be appropriate value of d_3 for filtering the higher order modes. Therefore, care should be taken while optimizing the value of d_3.

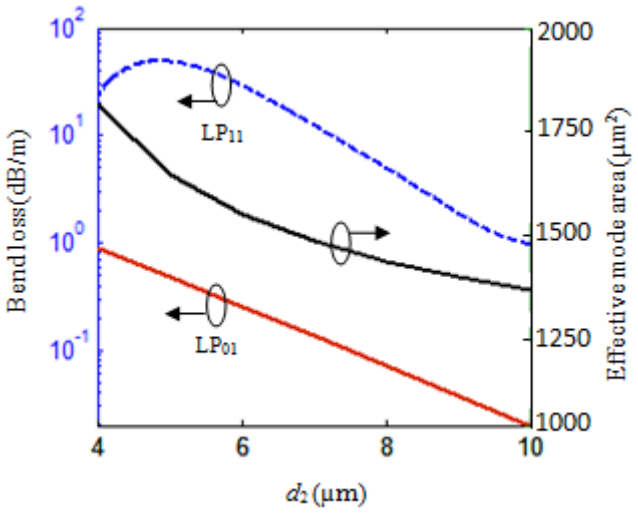

Fig. 2.4: Variation of the bend losses of LP_{01} and LP_{11} modes and the effective mode area of LP_{01} mode on d_2 at 1.064 µm wavelength with Λ = 21 µm, d_1 = 16 µm, d_3 = 6 µm, n_f = 1.448 and R = 30 cm.

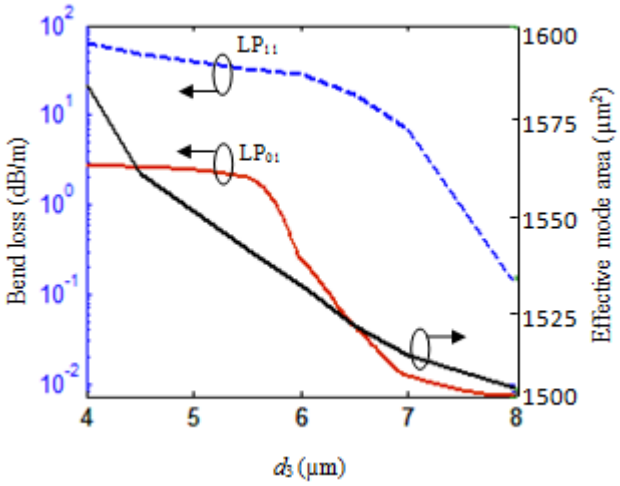

Fig. 2.5: Variation of the bend losses of LP_{01} and LP_{11} modes and the effective mode area of LP_{01} mode on d_3 at 1.064 µm wavelength with Λ = 21 µm, d_1 = 16 µm, d_2 = 6 µm n_f = 1.448 and R = 30 cm.

The variation of effective mode area of LP_{01} mode and bend losses of first two modes with the refractive index of fluorine doped fused silica rods (*i.e.* n_f) have been shown in Fig. 2.6. Bend losses of first two modes of structure increase on increasing the value of n_f. If n_f= 1.442, the bend loss of LP_{11} mode is 3.31 dB/m and the bend loss of LP_{01} mode is 0.05 dB/m. If n_f = 1.448, the bend loss of LP_{01} mode is 0.25 dB/m, which is within its acceptable range and the bend loss of LP_{11} mode is 29.22 dB/m which is large enough to leak out from the fiber. The effective mode area also increases on increasing the value of n_f. The reason of increasing bent losses of modes on increasing the refractive index of fluorine doped material rods is that the index contrast between core and cladding decreases, which allow the field to spread and hence bend losses and effective mode area increases.

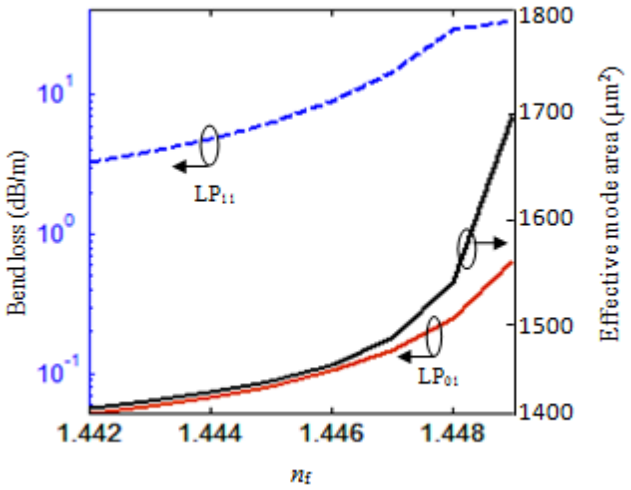

Fig. 2.6: Variation of bend losses of LP_{01} and LP_{11} modes and the effective mode area of LP_{01} mode on the refractive index of fluorine doped fused silica rods (i.e. n_f) at 1.064 μm wavelength, when Λ = 21 μm, d_1 = 16 μm, d_2 = d_3 = 6 μm and R = 30 cm.

The effect of different bend radii of the proposed PCF structure on the bend losses of LP_{01} & LP_{11} modes and the effective mode area of LP_{01} has been depicted in Fig.2.7 at 1.064 μm. The bend losses of LP_{01} & LP_{11} modes decrease on increasing bend radius. However, the differential bend loss between LP_{01} & LP_{11} modes increases on increasing the bend radius. At R = 30 cm, the differential bend loss is sufficiently large ($> 10^2$) and reaches$> 10^3$ for bend radius larger than 40 cm. Below 30 cm bend radius, the differential bend loss between LP_{01} & LP_{11} modes is small. Therefore, bend radius of 30 cm is the critical radius at which the higher order mode can be strike out

from the core of the proposed PCF structure. The effective mode area of LP_{01} mode increases with bend radius which is quite obvious.

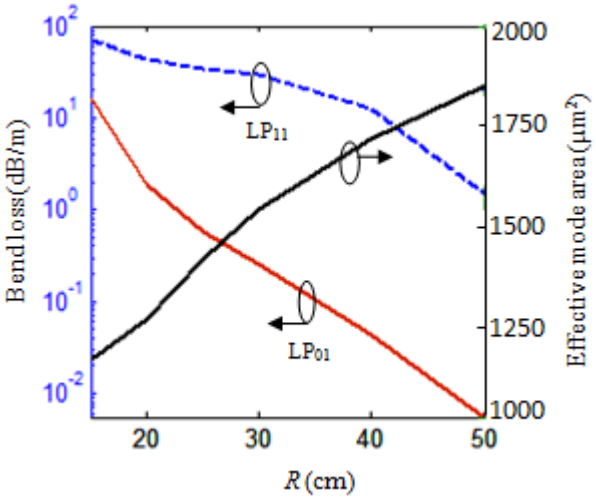

Fig. 2.7: Variation of bend losses of LP_{01} and LP_{11} modes and the effective mode area of LP_{01} mode on the bending radius (i.e. R) at 1.064 μm wavelength, when Λ = 21 μm, d_1 = 16 μm, d_2 = d_3 = 6 μm.

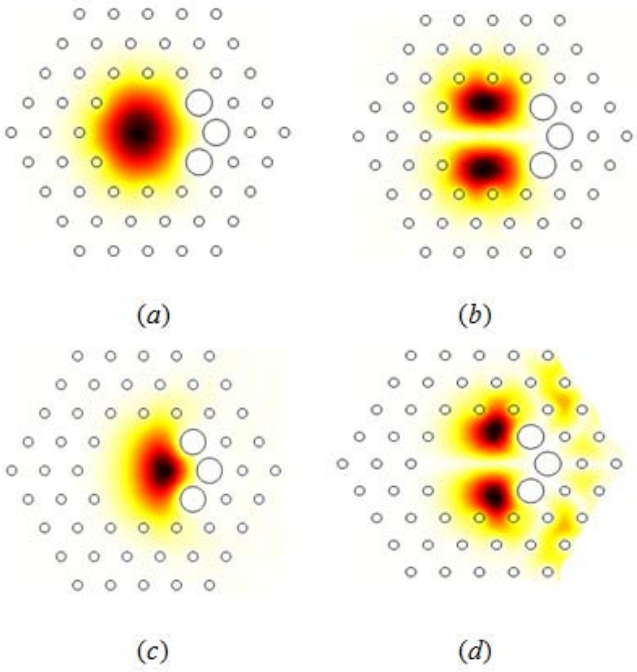

Fig. 2.8: The surface plot of (a) LP_{01} and (b) LP_{11} mode; when proposed PCF is in straight state; (c) LP_{01} and (d) LP_{11} mode when proposed PCF is bend with 30 cm bend radius at 1.064 μm wavelength; with Λ = 21 μm, d_1 = 16 μm, d_2 = d_3 = 6 μm and n_f = 1.448.

Figure 2.8 illustrates all the features of proposed PCF structure which have already been described in the above discussion. Fig. 2.8 (*a* & *b*) show the surface plot of LP_{01} and LP_{11} respectively when the proposed fiber is in straight state. Fig. 2.8 (*c* & *d*) illustrate the surface plot of LP_{01} and LP_{11} modes respectively in bent state of PCF with bend radius of 30 cm. It is clear from these figures that the LP_{01} mode is less leaky and well confined while the LP_{11} mode leaks significantly in the cladding region. The bend losses of both the modes are very less when the proposed PCF structure is in straight state.

2.5 Tolerance Analysis:

It is also very important for fabrication purposes, to investigate the tolerance of the proposed PCF design with respect to the various design parameters. After investigating the effect of variations in the values of d_1, d_2, d_3 and Λ we have found that the magnitude of bend losses of first two modes of the design and the effective mode area of LP_{01} modes are less sensitive to the structure parameters. For example, 1% variation in d_1 changes the bend losses of LP_{01} and LP_{11} modes by 2.4% and 2.5% respectively and changes the effective mode area of LP_{01} mode by 1%. Similarly, 1% variation in Λ changes the bend losses of LP_{01} and LP_{11} modes by 5% and changes the effective mode area of LP_{01} by 3%.

Finally, from the manufacturing point of view our proposed PCF structure can be fabricated using popularly known ‘stack and draw’ technique.

2.6 Conclusions

An asymmetric design of LMA PCF with SM operation and low bend loss is proposed in this paper. The SM operation is achieved by optimizing the structure parameters in such a way that it introduces very low bend loss for fundamental mode while very large bend loss for higher order modes. The effective mode area of LP_{01} mode of proposed PCF is as large as 1530 μm^2 with bend radius of 30 cm. In spite of such large effective mode area the proposed fiber structure offers very low bend loss for LP_{01} mode (*i.e.* 0.25 dB/m) while very large bend loss for LP_{11} mode (*i.e.* 29.22 dB/m). Therefore, such a bending can introduce more than 55 dB loss to LP_{11} mode, while only ~ 0.47 dB loss to LP_{01} in a single turn of bending with 30 cm bend radius. All the structural parameters *i.e.* d_1, d_2, d_3, Λ and n_f have effective control over the bend losses of fundamental and

first higher order mode. Proposed PCF structure has potential applications in compact high power delivery devices such as high power fiber lasers and amplifiers.

CHAPTER 3

Triangular Core Large Mode Area Photonic Crystal Fibers*

3.1 Introduction

LMA in fiber geometry can be achieved by increasing its core size. However, a large core size can allow the higher order modes to propagate through it. Tremendous efforts have been made earlier to enlarge the effective mode area in fibers for applications in optical communications and high power fiber lasers and amplifiers [15 – 31, 87, 88]. *Rastogi et al*. presented LMA fiber structure by using azimuthally segmented cladding profile [30, 31]. LMA waveguide design with effective SM operation has also been analyzed in rectangular geometry [89]. Recently, LMA PCF with a triangular core (TC) structures have been proposed for compact high power fiber lasers [79, 90]. However, these TC PCF structures are restricted by bending radius up to 30 cm. Therefore, for design and development of compact high power delivery devices, it is desirable to design a new PCF structure which offers the LMA at even below 30 cm bending radius.

In this chapter, two geometries (I & II) of TC LMA PCF which offer effective SM operation with low bending loss at 1.064 μm are reported. Geometry-I is able to offer a low bending loss at 20 cm bend radius with effective mode area of 875 μm^2. While, the geometry-II is able to offer effective SM operation even at 15 cm bending

*Parts of the results presented in this chapter have been reported in research publications:

1. T. S. Saini, A. Kumar, R. K. Sinha, "Triangular-core large-mode-area photonic crystal fiber with low bending loss for high power applications," *Applied Optics* 53(31), 7246-7251 (2014);
2. T. S. Saini, A. Kumar, R. K. Sinha, "Design of large-mode-area microstructured optical fiber with single-mode operation for high power fiber lasers" *Advanced Science Letters*, In Press (2015).

radius with EMA as large as ~800 μm^2. Simulated results indicate that the proposed structure can be a useful candidate for design and development of compact high power delivery devices such as high power fiber lasers and amplifiers.

3.2 TC LMA PCF Geometry-I

The transverse cross-sectional view of proposed TC LMA PCF geometry-I is shown in Fig. 3.1. The air holes are drawn in triangular lattice pattern in the silica glass along the length of the PCF. Three air holes are removed to make the triangular core of the structure. Six air holes of the first ring are replaced by six down-doped silica material rods (gray circles in Fig. 3.1) and rest three air holes have relatively larger diameters. The diameter of three bigger air holes in the first ring is considered as d_0 while the diameter of smaller air holes and the down doped silica rods in the cladding is considered as d_1. The centre to centre distance (*i.e.* pitch) of the air holes is constant and represented by Λ. To insure LMA with effective SM operation, the structural parameters of PCF geometry are optimized accordingly. The optimized structural parameters are summarized in Table-3.1. The refractive indices of fused silica and down doped material rods are taken as 1.45 and 1.4462 respectively at operating wavelength. All the simulations in this chapter are carried out at operating wavelength of 1.064 μm. The method of analysis is the same as described in the Section-2.3.

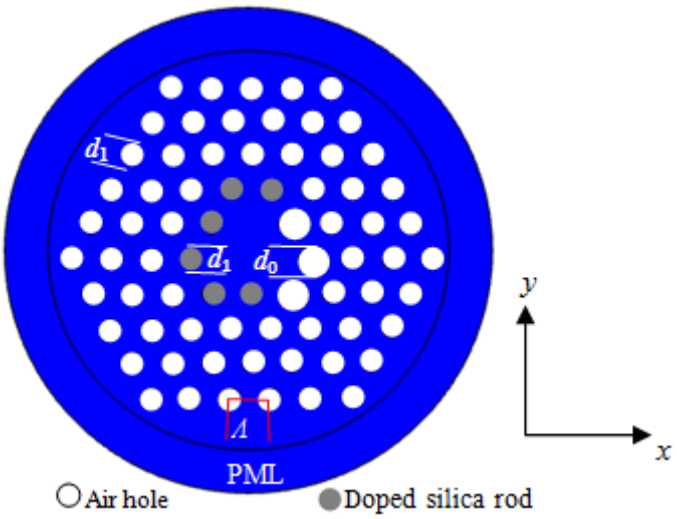

Fig. 3.1: The transverse cross-sectional view of proposed TC LMA PCF geometry-I.

3.2.1 Results and discussion

TC LMA PCF design has been presented to realize the bend induced mode filtering keeping in mind that such bending should not introduce significant bend loss to fundamental mode. It is worthwhile to mention here that the bending loss of proposed structure increases on increasing the mode-order. Therefore, only first two modes (*i.e.* LP_{01} & LP_{11}) of the fiber structure have been included in the study. For optimization of structural parameters, the effects of bending losses of LP_{01} & LP_{11} modes and effective-mode-area of LP_{01} mode have been studied by varying a particular parameter while keeping other parameters fixed.

The influence of pitch (Λ) on bending losses of LP_{01} & LP_{11} modes and the effective-mode-area of LP_{01} mode is illustrated in Fig.3.2. It can be noted that, in general, the bending losses of LP_{01} & LP_{11} modes increases with Λ.

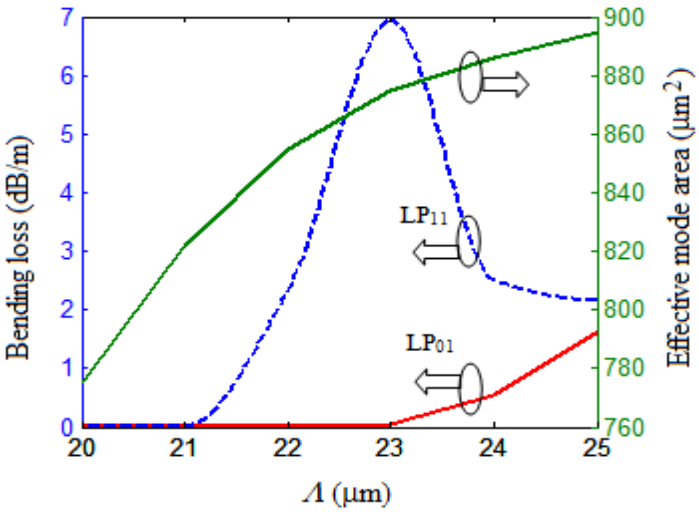

Fig. 3.2: The variation of bending loss of LP_{01} & LP_{11} modes and the effective mode area of LP_{01} mode with Λ (when d_0 =14 μm, d_1 =10 μm, R = 20 cm, n_f = 1.4462, and λ = 1.064 μm).

There is a resonance peak in the bending loss of LP_{11} mode at Λ = 23 μm, which is the signature of strong resonance of LP_{11} mode to the cladding at this value of Λ. Below this value of Λ, the bending loss of the first higher order mode decreases sharply. This indicates that the SM operation is difficult to achieve with the values of Λ below 22.5 μm. At higher value of the Λ, the LP_{01} mode attenuated rapidly. At Λ = 23 μm the bending loss of LP_{11} mode is~7 dB/m, which is sufficient to stripe off the LP_{11} mode from the core. The effective mode area of LP_{01} mode increases with Λ. It is due

to increase in core size while increasing the pitch. The effective mode area of LP_{01} mode is 875 μm^2 at Λ = 23 μm.

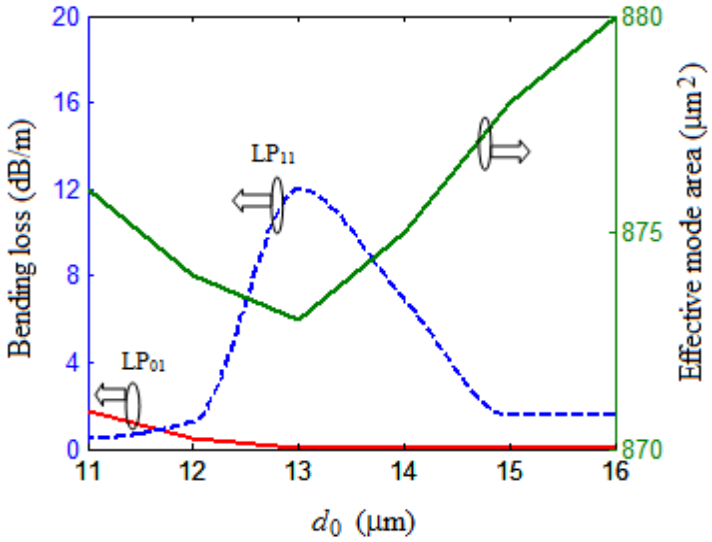

Fig. 3.3: The variation of bend loss of LP_{01} and LP_{11} mode and the effective mode area of LP_{01} mode with d_0 (when Λ = 23 μm, d_1 =10 μm, R = 20 cm, n_f = 1.4462, and λ = 1.064 μm).

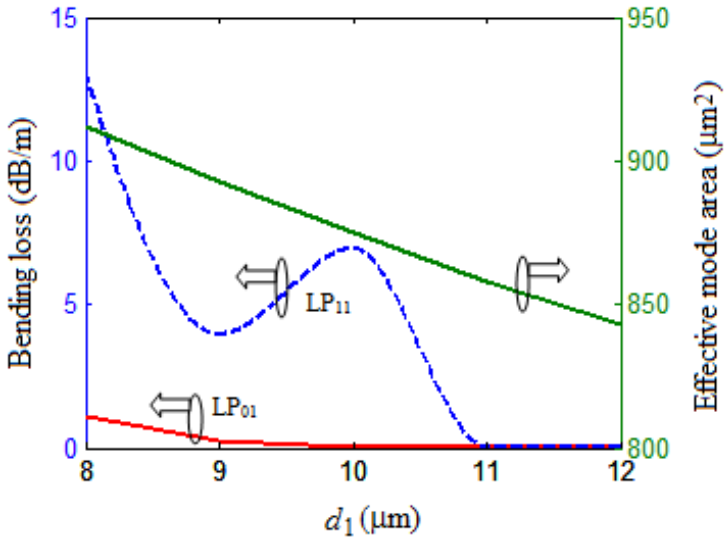

Fig. 3.4: The variation of bending loss of LP_{01} and LP_{11} mode and the effective mode are of LP_{01} mode with d_1 (when Λ = 23 μm, d_0 =14 μm, R = 20 cm, n_f = 1.4462, and λ = 1.064 μm).

The variation of the diameter of bigger air holes (*i.e.* d_0) on bending losses of LP_{01} & LP_{11} modes and effective-mode-area of LP_{01} mode is shown in Fig. 3.3. The bending loss of LP_{01} mode is decreases with d_0. The bending loss of LP_{11} mode shows a peak at d_0 = 13 μm, which is the indication of resonance of the LP_{11} mode to the outer

cladding at this value. At the same time the bending loss of LP_{01} mode is ~0.62 dB/m, which is also relatively high loss for fundamental mode. The bending loss of LP_{01} and LP_{11} modes are 0.038 dB/m and 6.94 dB/m at d_0 = 14 µm. The bending loss of LP_{11} mode is sufficiently large to leak out from the core of proposed TC PCF after travelling 3 meter distance. The effective mode area of LP_{01} mode is 875 μm^2 at d_0 = 14 µm. The effective-mode-area of LP_{01} mode is not changing significantly with variation of d_0. Throughout the range of d_0, the effective-mode-area varies between 873 μm^2 – 880 μm^2.

The variations of the diameter of smaller air holes (*i.e.* d_1) on the bending losses of LP_{01} & LP_{11} modes and the effective-mode-area of LP_{01} mode have been illustrated in Fig. 3.4. The bending loss of LP_{01} mode decreases on increasing d_1. It is clear from the Fig. 3.4 that the bending loss of LP_{11} mode shows a resonance peak at d_1 = 10 µm. For d_1 < 10 µm, bending losses of both the modes are significantly large. The bending loss of LP_{01} and LP_{11} modes at d_1 = 10 µm are 0.038 dB/m and 6.94 dB/m respectively with effective-mode-area of 875 μm^2. The bending losses of both the modes are less on the higher values of d_1. At the higher values of d_1 the proposed TC PCF structure would be multimode. Therefore, d_1 = 10 µm is the optimized value for insuring LMA with effective SM operation. The effective-mode-area of LP_{01} mode varies between 843 μm^2 to 912 μm^2 with throughout the range of d_1.

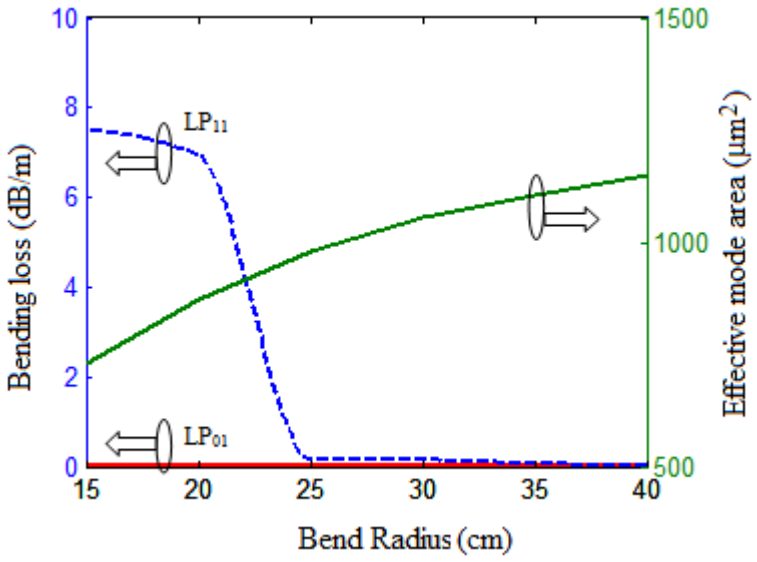

Fig. 3.5: The variation of bending loss of LP_{01} and LP_{11} mode and the effective mode are of LP_{01} mode with R (when Λ = 23 µm, d_0 =14 µm, d_1 =10 µm, n_f = 1.4462, and λ = 1.064 µm).

The performance of proposed TC PCF structure on the bend state has been depicted in Fig. 3.5. As the bend radius (*i.e. R*) increases the bend losses of LP_{01} & LP_{11} modes decrease while the effective-mode-area of LP_{01} mode increases. At R = 10 cm the bend loss of LP_{11} mode is large and the effective mode area is less (*i.e.* 732 μm^2). When R is greater than 20 cm the bending loss of LP_{11} mode decreases rapidly. The proposed fiber structure becomes multimode for the value of R more than 20 cm.

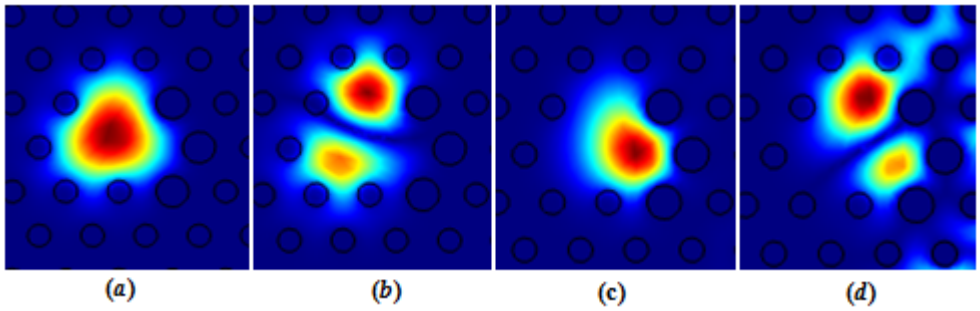

Fig. 3.6: Electric field distribution of (a) LP_{01} mode; (b) LP_{11} mode; when proposed PCF is in straight state; (c) LP_{01} mode; (d) LP_{11} mode; when proposed PCF is in bend state with bend radius of 20 cm in x-direction at operating wavelength of 1.064 µm.

At R = 20 cm the bending losses of LP_{01} & LP_{11} modes are 0.038 dB/m and 6.94 dB/m respectively with effective-mode-area of 875 μm^2. The loss of LP_{11} mode becomes more than 20 dB after travelling 3 m long fiber. While, the LP_{01} mode suffer with 0.11 dB loss in same length of proposed TC PCF. Therefore ~3 m long proposed TC PCF is sufficient to offer effective SM operation with effective mode area of 875 μm^2.

All the features of proposed TC PCF structure which have already been described in the above discussion have been depicted in Fig. 3.6. The surface plots of LP_{01} and LP_{11} when the proposed TC PCF is in straight state are shown in Fig. 3.6(*a*) and Fig. 3.6(*b*) respectively. The surface plots of LP_{01} and LP_{11} modes in bent state of TC PCF with bend radius of 20 cm are illustrated in Fig 3.6(*c*) and Fig. 3.6(*d*) respectively. It is clear from these figures that the LP_{01} mode is less leaky and well confined in the fiber core, while the LP_{11} mode leaks significantly in the cladding region. The bend losses of both the modes are small when the proposed fiber is in straight state.

3.2.2 Tolerance analysis of geometry-I

It is also very important for fabrication purposes to investigate the tolerance of the proposed design with respect to the various design parameters. After investigating the effect of variations in the values of d_0, d_1, and Λ we have found that the magnitude of bend loss of first two modes of design and the effective mode area of LP_{01} modes are less sensitive to the structure parameters. For example, 1% variation in d_0 changes the bend losses of LP_{01} and LP_{11} modes by ~2% and ~3% respectively and changes the effective mode area of LP_{01} mode by 1%.

Table-3.1: The optimized structural parameters of proposed TC PCF.

Parameter name	d_0 (µm)	d_1 (µm)	Λ (µm)	R (cm)
Parameter value	14	10	23	20

3.3. TC LMA PCF Geometry-II

The transverse cross-section of the proposed TC LMA PCF geometry-II has been shown in Fig. 3.7.

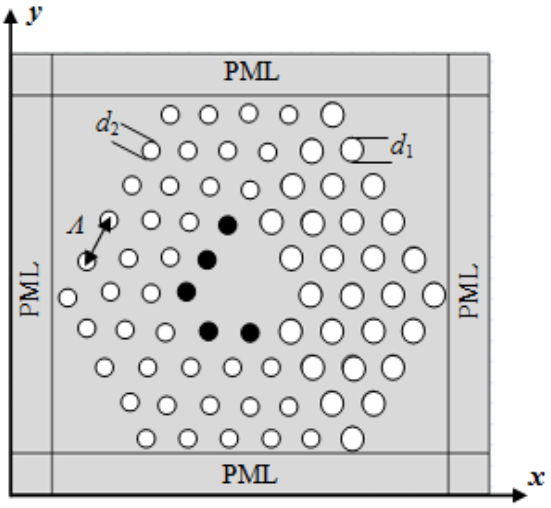

Fig. 3.7. The transverse cross-section of the proposed TC LMA PCF geometry-II

As shown in Fig. 3.7, proposed structure consists of two different sizes of air holes. Relatively larger air holes on the right side (along positive x-direction) of the core have diameter d_1, while the smaller air holes on the left side of the core have diameter d_2. All the simulations have been performed by considering that the PCF structure is bent at bending radius of 15 cm along positive x-direction. However,

bending the fiber reduces the mode area. To avoid the reduction in mode area, five down doped material rods (black circles in Fig.3.7) of refractive index, n_f = 1.4474 have been introduced in place of five air holes of first ring in the opposite direction of bending. Larger air holes in the bending direction reduce bending losses of the modes. The centre to centre distance, i.e., pitch (Λ) for all the holes are same. The operating wavelength is taken as 1.064 μm. The method of analysis of this TC PCF structure is same as discussed in Section 2.3.

3.3.1 Results and discussion

In our simulation, we have taken following parameters unless stated otherwise: d_1 = 10 μm, d_2 = 3.6 μm, Λ = 20 μm, and R = 15 cm. To investigate the possibility of LMA with effective SM operation of the proposed structure, the effects of various structure parameters on the bending losses of first two modes have been investigated. Full vectorial finite element method has been employed to investigate the modal properties of the proposed TC PCF structure.

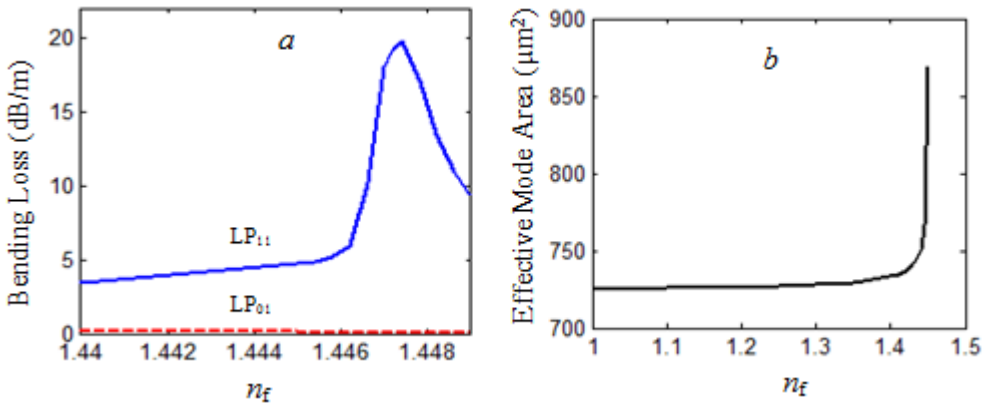

Fig. 3.8: Effect of n_f on (a) the bending loss and (b) Effective mode area.

It is very important to optimize the n_f in terms of bending loss and EMA. To optimize the n_f, we have studied the effects of n_f on bending loss and EMA and presented in Fig. 3.8(a) & (b). Bending loss of LP_{01} mode is almost constant; however, we can see a clear peak in the loss curve of LP_{11} mode. This peak in the bending loss of LP_{11} mode is due to the resonance coupling of LP_{11} mode to cladding mode for n_f =1.4474. Such a strong resonance coupling improves the differential bending loss and makes the fiber able to leak all the higher-order modes by introducing more than 20 dB loss within ~ 1 m of propagation length. We have also calculated the bending loss of

the LP_{11} mode for n_f =1 (air holes). Our calculation shows that with five air holes, LP_{11} mode suffers from only 2.72 dB/m bending loss, and would not leak out from the fiber. Thus the fiber with five air holes would not be a single mode fiber. We have also studied the effect of n_f on EMA and presented in Fig. 3.8(b). One can note that the EMA increases from 735 to 800 μm^2 by replacing the five air hole with the doped rods of n_f = 1.4474. From above discussion one can conclude that n_f is very important parameter for achieving effective SM operation with improved LMA.

The variation of bending loss of the fundamental mode and first higher order mode with fiber pitch (Λ) is shown in Fig. 3.9. It can be noted that, the bending losses of modes increase with mode order. Therefore, the bending losses of only first two modes (*i.e.* LP_{01} and LP_{11}) have been included in the investigation of the proposed PCF structure. The EMA and the bending losses of modes increase with Λ. It is because of increasing the core size while increasing Λ.

The loss ratio, which is defined as the ratio of the first higher order mode to fundamental mode, is greater than the order of 10^2 in the entire range of pitch and reaches to the value greater than the order of 10^3 for Λ = 18 μm. However, at smaller pitch, the bending loss of the LP_{11} mode becomes too small to leak the unwanted modes. Thus, the suitable parameters are those parameters which can ensure the higher-order mode filtering with nominal loss to fundamental mode. For example: at Λ = 20 μm, the loss of LP_{01} is only 0.064 dB/m and LP_{11} mode is ~20 dB/m. A fiber design with such parameter ensures the effective SM operation in the proposed structure only after 1 meter of propagation length. Thus, we have chosen 20 μm pitch of the structure to achieve larger loss ratio with minimum loss of fundamental mode in further analysis of structure. The EMA of fundamental mode is 794 μm^2 with 15 cm bending radius.

Next, the diameter of bigger air holes d_1 within the range of 8 -12 μm is varied and the effect on the EMA of LP_{01} mode and the bending losses of LP_{01} and LP_{11} modes have been investigated. This feature of proposed PCF structure has been illustrated in Fig. 3.10. The figure indicates that the parameter d_1 has good control over the bending losses of LP_{01} and LP_{11} modes. The bending loss of LP_{11} mode is always larger than 6 dB/m during the entire variation range of d_1. The large bending loss ratio ($\geq 10^2$) between LP_{11} to LP_{01} mode has been achieved when d_1 is near about 10 μm. Therefore, at this value of d_1, the proposed PCF structure offers effective SM operation in spite of large EMA. The variation of EMA with d_1 shows an oscillatory nature which

is due to the weak resonance of the LP_{01} mode with cladding mode in the direction of bending. The signature of small resonance can also be seen in the corresponding loss of LP_{01} mode. However, the EMA remains in the range of ~800-875 μm^2 and maintain the LMA operation.

The variation of structure parameter d_2 has been illustrated in Fig. 3.11. The parameter d_2 plays an important role for keeping the bending loss of fundamental mode very low with very high bending loss ratio (~10^3) throughout the range of d_2 within 3.2 – 5.2 µm. The minimum loss of LP_{11} mode is ~18 dB/m while the maximum bending loss of LP_{01} is only ~0.1 dB/m. The EMA of LP_{01} mode varies from 752 - 800 μm^2. The PCF structure of such large EMA is able to suppress all unwanted nonlinear effects efficiently.

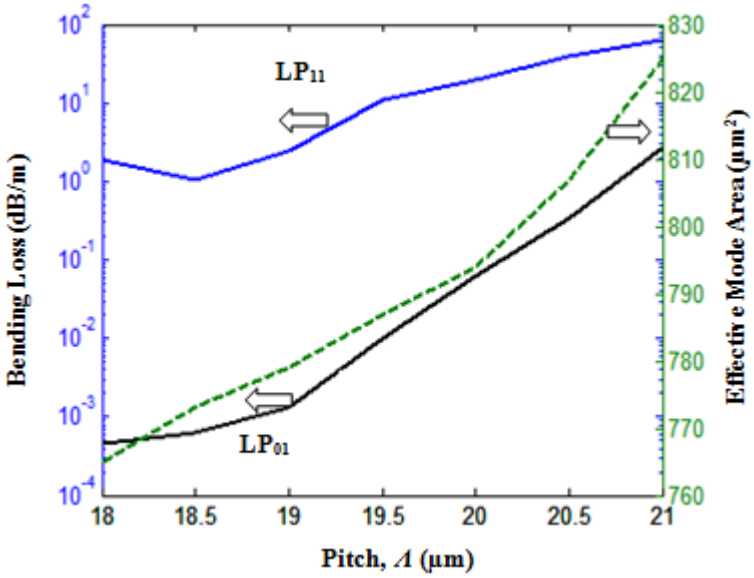

Fig. 3.9: The variation of effective mode area of LP_{01} mode and bending losses of LP_{01} and LP_{11} modes with fiber pitch (Λ).

From Fig.3.12 it is clear that the bending has a critical effect on the LMA operation of proposed TC PCF. Bending losses of the modes decrease on increasing the bending radius, but, the differential bending loss increases with bending radius. The loss ratio is sufficiently large (~10^2) when bending radius is equal to 15 cm and reaches to more than 10^3 for bending radius larger than 20 cm. It is important to note that there is a sharp variation in the bending losses of both the modes around R = 15 cm. This feature of proposed PCF informs that the bending radius below 15 cm will cause the rapid decay in fundamental mode and the bending above 15 cm will support the LP_{11}

mode to propagate. Therefore, 15 cm is the appropriate bending radius for proposed TC PCF structure. The EMA of LP_{01} mode increases on increasing the bending radius which is quite obvious and shown in Fig. 3.12.

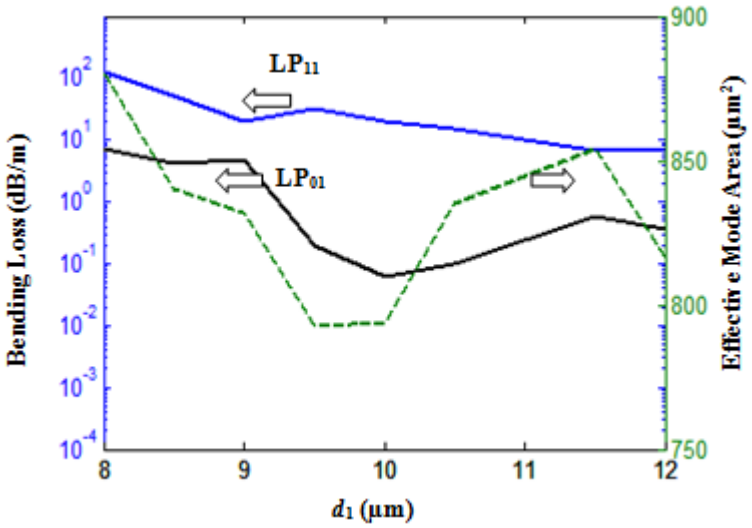

Fig.3.10: The variation of the effective mode area of LP_{01} mode and the bending losses of LP_{01} and LP_{11} modes with d_1.

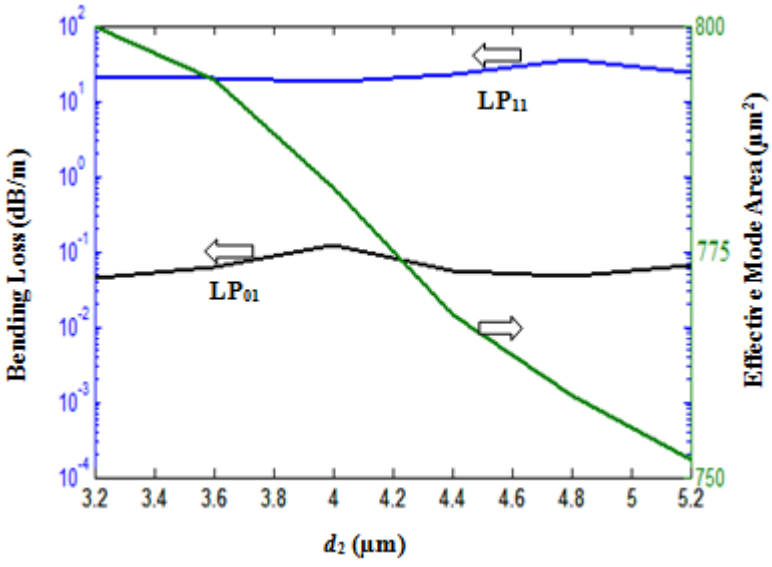

Fig. 3.11: The variation of the effective mode area of LP_{01} mode and the bending losses of LP_{01} and LP_{11} modes with d_2.

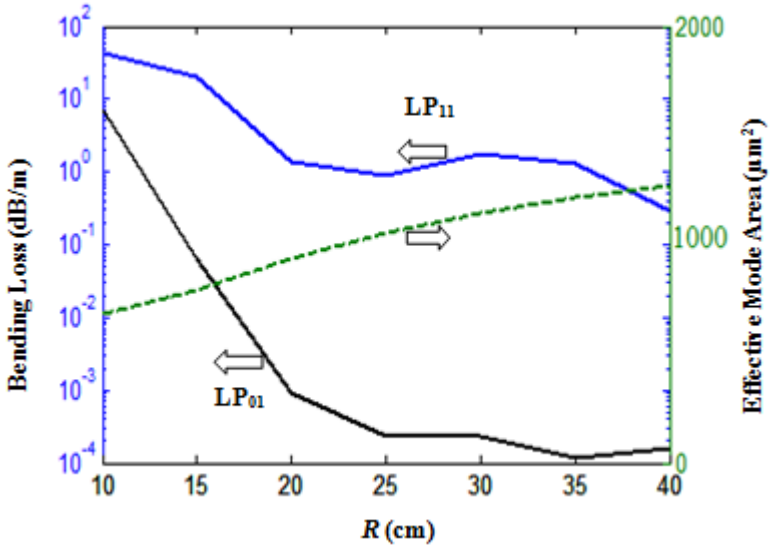

Fig. 3.12: The variation of the effective mode area of LP_{01} mode and the bending losses of LP_{01} and LP_{11} modes with bending radius, R.

Finally, the contour plots of LP_{01} and LP_{11} modes have been shown in Fig.3.13 at wavelength, λ = 1.064 μm. It is noticed that LP_{01} mode is well confined within the core with nominal bending loss while LP_{11} mode suffers from larger bending loss.

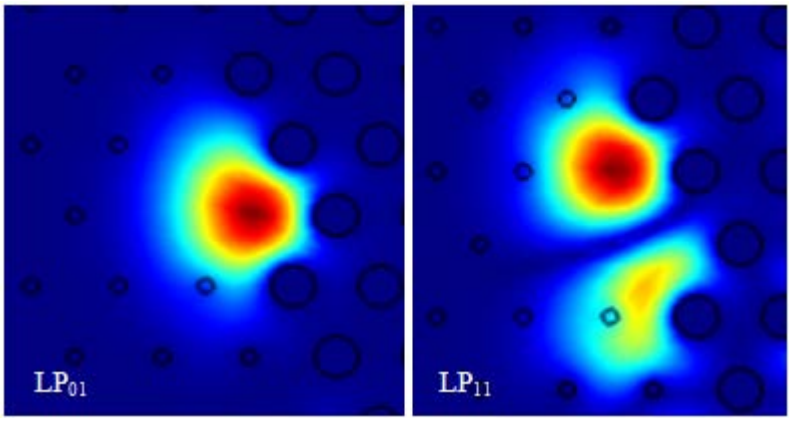

Fig. 3.13: Contour plot of LP_{01} and LP_{11} at optimized parameters (i.e. d_1 = 10 μm, d_2 = 3.6 μm, Λ = 20 μm, n_f = 1.4474 and bending radius, R = 15 cm).

3.3.2 Tolerance Analysis of Geometry-II

After investigating the effect of small variations in the values of d_1, d_2, d_3 and Λ, it is found that the magnitude of bending loss of first two modes and the effective mode area of LP_{01} mode are less sensitive to the structural parameters.

From the manufacturing point of view the proposed structures can be fabricated using popularly known 'stack and draw' technique.

3.4 Conclusions

Two TC LMA PCF structures offering low bending loss with effective single mode operation have been presented in this chapter. For geometry-I the effective mode area of LP_{01} mode is as large as 875 μm^2 with bend radius of 20 cm. In spite of such large effective mode area the proposed TC PCF structure offers very low bend loss for LP_{01} mode (*i.e.* 0.038 dB/m) while very large bend loss for LP_{11} mode (*i.e.* 6.94 dB/m). Therefore, such a bending can introduce more than 20 dB loss to LP_{11} mode, while only ~ 0.11 dB loss to LP_{01} in a three meter length of PCF. For geometry-II the effective mode area of LP_{01} mode has been achieved as large as ~800 μm^2 with 15 cm bend radius at 1.064 μm; which confirms the elimination of unwanted nonlinear effects. Proposed geometry-II offers very low bending loss (*i.e.* 0.064 dB/m) for LP_{01} and very large bending loss (*i.e.* ~20 dB/m) for LP_{11} mode. The loss ratios of LP_{01} and LP_{11} modes for both the structures have been achieved as large as the order of 10^2 which confirms the effective SM operation. These features of proposed TC PCF structures have made it applicable for compact high power delivery devices such as high power fiber lasers and amplifiers.

CHAPTER 4

Large Mode Area Multi-trench Leaky Channel Waveguide*

4.1 Introduction

Integrated optic waveguide lasers have always been a matter of inquisitiveness for their compactness and possibility of integrating several components [91 – 96]. Significant efforts have already been made to enhance the output power of waveguide lasers. Use of competent pumping schemes, suitable rare earth materials, and LMA waveguide designs with SM operation are some of the schemes to raise the power output of waveguide laser [89, 97 – 101]. In this regard, during the last two decades, researchers are trying very hard to attain LMA waveguides with SM operation for applications in compact integrated optical devices and high power waveguide lasers and amplifiers [98 – 101]. Single-mode operation in large-core waveguide has been achieved by deep etching in semiconductor waveguide and using small index contrast in polymer waveguide [98, 99]. A large core polymer waveguide has been demonstrated for large alignment tolerance and high attenuation efficiency [98]. Use of rib waveguide and shallow rib waveguide are another method to enlarge core dimension for effective single-mode operation [99]. However, these waveguides are sensitive to severe corner losses, crosstalk and background scattering [100]. Controlling the mode shape is also a challenging task in shallow rib waveguide. Single-mode performance of the shallow etched waveguide is very sensitive to the etch depth and is difficult to achieve precisely over the entire wafer. In order to overcome, these problems, *Heaton et al*. have

*A part of the results presented in this chapter has been reported in a research publication:
T. S. Saini, A. Kumar, R. K. Sinha, "Design and analysis of large-core multi-trench channel waveguide for high power applications," *Applied Optics* 54(19), 6134 – 6139 (2015).

presented theoretical and experimental demonstration of deep etched GaAs/AlGaAs waveguides with core thickness and width of 4.8 and 5.7 μm [100]. The advantage of deep-etched waveguides is that the etching depth is not a critical parameter for SM operation and etching can be done using conventional reactive ion etching method. However, a more complex cladding design is required to achieve SM operation by this deep etched waveguide. Recently, leaky cladding has been utilized to achieve the LMA SM operation in slab geometries [89, 101, 102]. A graded index design is utilized in planar and channel waveguide to show effective waveguide geometry [89, 101]. These designs provide more than twice the mode-area for SM operation in comparison to convention design. However, fabrication of graded-index profile is difficult. In order to simplify the design, a leaky planar waveguide structure with alternatively low and high index multi-layered in cladding is proposed [102]. This multilayered geometry of waveguide is easier to fabricate in contrast to the waveguide geometries proposed in [89, 101].

In this chapter, a large-core multi-trench rectangular channel waveguide structure for effective single-mode operation has been designed. This design offers the SM operation with relatively two times larger mode area than that of deep-etched waveguide and can be fabricated by reactive-ion etching technique. The design is based on the principle of higher-order mode filtering. The effective single-mode operation has been achieved by choosing the waveguide parameters in such a way that it induces a very high leakage loss for higher order mode while very low leakage loss for fundamental mode. A power law profile for trench-assisted cladding is considered, which is solved by using commercially available software 'COMSOL Multiphysics' based on FEM. With suitable cladding parameters, proposed structure ensures extended SM operation in the spectral range of 1.25 – 2.0 μm with the rectangular core-area as large as 100 μm^2.

4.2. Proposed Channel Waveguide Design

Figure 4.1 shows the transverse cross-sectional view of the proposed large-core size channel waveguide structure, which is characterized by a rectangular core and trench - assisted geometrically shaped cladding. The refractive index of core is high which is taken as n_f and it is formed on substrate of lower refractive index n_s. The thickness of core is h and width is taken as $2a$.

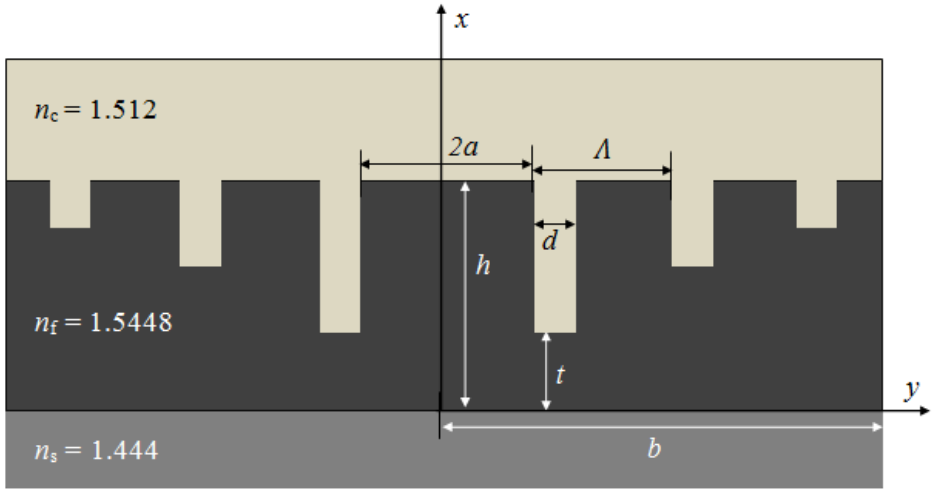

Fig. 4.1: Transverse cross-sectional view of the proposed large-core size channel waveguide structure.

To make the cladding, we inserted low-index multi-trenches around both sides of the core. The width of low index trenches is taken as d and the distance between two trenches is taken as $\Lambda - d$. Where, Λ is the pitch of the trench. The cladding is made by the same material as that of the core. The structure is covered by another lower index material of refractive index n_c. As shown in the Fig. 4.1, the height of first trench from the core-substrate interface is taken as constant and it is represented by t at $y = \pm a$. The height of other trenches are decided by the following power-law equation:

$$x^2(y) = h^2 - (h^2 - t^2)\left\{\left[\frac{b-y}{b-a}\right]^q\right\}, \quad a \le y \le b \qquad (4.1)$$

where, q is a cladding parameter which characterized the shape of the profile and hence the heights of the trenches. A similar expression can be written for $-a \le y \le -b$ *i.e.* for the left side of the core. In order to have the comprehensive study of the multi-trench cladding (*i.e.* the position and height of the trench) on the single-mode performance of waveguide we have utilized a more general power-law profile. The profile with $q = 0$ will represent a multi-trench waveguide in which all the trenches will start from the same height t. The profile, $q = \infty$ will represent a W-shaped channel waveguide. The other possible shape of the cladding is shown in the Fig. 4.2. All the modes which exist in this structure are leaky due to the high-index cladding reaching at the same height as that of the core. The cladding parameters t, q and b control the leakage losses of the modes in the core of the waveguide. Such cladding structure allows us to achieve effective SM operation with a large-core size waveguide structure

for extended range of wavelengths. The method of analysis is the same as shown in Section 2.3 of Chapter 2.

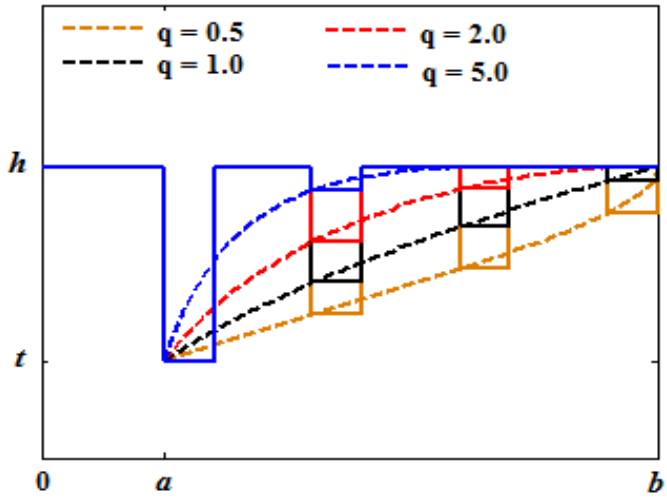

Fig. 4.2: Representation of various profiles of the multi-trench cladding according to the power–law expression Eq (4.1).

4.3. Numerical Results and Discussion

The parameters which we use for designing of the proposed waveguide structure are: n_f =1.5448, n_s = 1.444, n_c = 1.512, Λ = 6 µm, d = 1 µm, h = 10 µm, a = 5 µm, b = 25 µm and t = 4 µm. These parameters are typical of a polymer waveguide fabricated on silica substrate. This proposed large-core size channel waveguide can be fabricated by well known reactive ion etching technique. All the simulating results illustrated in the Figs. 4.3 – 4.10 are performed at 1.55 µm wavelength. In order to choose the allowed operating range of parameters, the maximum loss for E_{11}^x mode is set to 1.0 dB/mm while the minimum loss for E_{21}^x mode is set to 4.0 dB/mm. Thus, a waveguide of length less than 5 mm is required to show effective SM operation.

Figure 4.3 shows the variations of effective mode indices of fundamental and first higher order mode of waveguide with the cladding profile parameter q at 1.55 µm. It is clear from this figure that the leaky cladding has trivial effect on the effective indices of the modes. It is observed that the leakage losses of other higher-order modes are higher than that of E_{21}^x mode. Therefore, in order to achieve effective SM operation, it is sufficient to show the filtering of E_{21}^x mode from the waveguide. The x-polarized mode is studied to illustrate the properties of the proposed channel waveguide.

From Fig. 4.4 it is clear that leakage losses of the both the modes increase with q and saturates for $q > 1$. Differential leakage loss can be made as large as 10^2. It is clear that for $q > 1$, the loss of E_{11}^x mode becomes higher than 1.0 dB/mm, however, for $q < 0.25$, the loss of E_{21}^x becomes lower than 4 dB/mm. Hence $0.25 < q < 1.0$ meets the criteria of effective SM operation with the proposed waveguide parameters. In order to explain the process of effective-single-mode (ESM) operation, the current study only considers the leakage losses of the first two modes of the waveguide structure. Material loss and surface roughness have not been included in the present study for ESM. However, the additional losses (material and roughness) would further help in filtering the unwanted modes.

For example, a channel waveguide with a = 5 μm, h = 10 μm, q = 0.5, t = 4 μm and b = 25 μm introduces a loss of 0.25 dB/mm for E_{11}^x mode and a loss of 8.73 dB/mm for the E_{21}^x at 1.55 μm wavelength. A 2.3 mm long such waveguide introduces more than 20 dB loss to E_{21}^x mode, while the E_{11}^x mode suffers only by 0.57 dB loss. Therefore, the waveguide is practically SM after the short propagation length of 2.3 mm. We have taken q = 0.5 to study the effects of other parameters for effective SM operation.

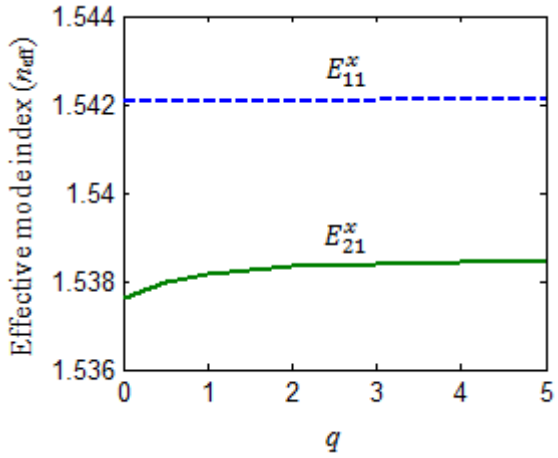

Fig. 4.3: Effect of the profile parameter q on the effective indices of the first two modes of the waveguide at 1.55 μm wavelength when a =5 μm, b = 25 μm, h = 10 μm, d = 1 μm Λ = 6 μm and t = 4 μm.

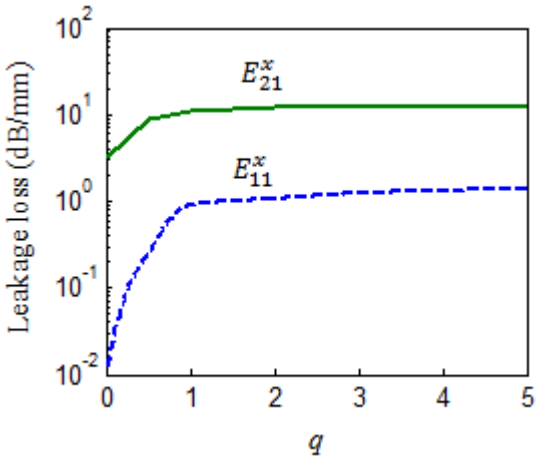

Fig. 4.4: Effect of the profile parameter q on the leakage losses of the first two modes of the waveguide at 1.55 μm wavelength when a =5 μm, b = 25 μm, h = 10 μm, d = 1 μm, Λ = 6 μm and t = 4 μm.

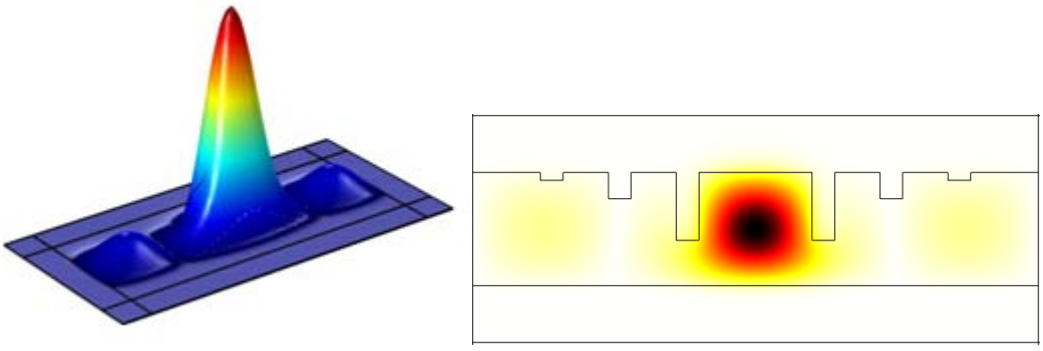

(a) (b)

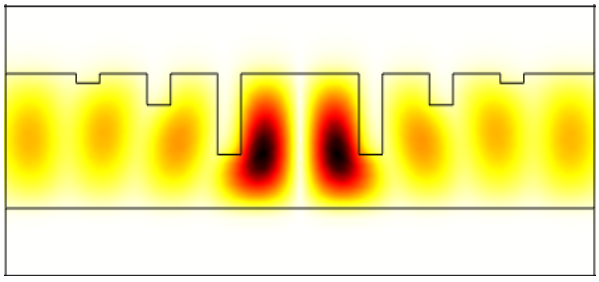

(c)

Fig. 4.5: Normalized electric fields of the (a) E_{11}^x mode, (b) contour plot of the E_{11}^x mode, (c)the contour plot of the E_{21}^x mode; when a =5 μm, b = 25 μm, h = 10 μm, q = 0.5, d = 1 μm, Λ = 6 μm and t = 4 μm and λ = 1.55 μm.

To show the leakage mechanism in proposed waveguide, the normalized electric field and surface plot of the E_{11}^{x} mode have been shown in Figs. 4.5(*a*) & (b). Fundamental mode is well confined inside the core region. The calculated effective mode-area of the E_{11}^{x} mode is 68.5 μm^2. Waveguide with such a large mode area is suitable for high power applications such as high power waveguide lasers and amplifiers. In Fig. 4.5(*c*) the surface electric field of E_{21}^{x} mode along with the waveguide structure is shown. It is quite obvious from the contour plot of E_{21}^{x} mode that sufficient field is spreading in the leaky cladding region. This makes the mode highly leaky.

4.3.1 Effect of the cladding parameters

In the proposed waveguide structure the cladding parameters are *q*, *t*, and *b*. These parameters control the SM operation of the waveguide. The effects of the profile parameter *q* on the effective index and leakage loss of E_{11}^{x} and E_{21}^{x} modes have already been shown in Figs. 4.3 & 4.4. Parameter *q* does not affect the dispersion properties of the waveguide. However, the leakage losses of both the modes are significantly affected by *q*. Leakage losses of the modes increase on increasing the value of *q*, while the differential leakage loss decreases with *q*. The leakage loss of the particular mode depends upon the distance between core and leaky cladding. Larger the distance, smaller is the leakage loss. The differential leakage loss between first two modes of proposed waveguide structure depends on the relative leaking distances of the modes. From above discussion, we can conclude that *q* is an important parameter for designing the waveguide for SM operation.

The effect of the parameter *b* on the leakage losses of first two modes is shown in Fig. 4.6. The figure indicates that leakage losses of both the modes decrease with *b*. This is due to fact that at large value of *b*, the leaky cladding moves away from core and reduces the loss of individual mode. It is also to be noted that the differential leakage loss of modes decrease on increasing *b*. One can conclude that $18 < b < 36$ μm are the allowed values for LMA SM operation. Figure 4.7 illustrates the effect of cladding parameter *t* at 1.55 μm wavelength. As the value of parameter *t* increases the leakage loss of first two modes of waveguide increases. It is because of the index contrast between core and cladding decreases on increasing the value of *t*. From Fig. 4.7 we conclude that $2 < t < 5$ μm are the allowed values of *t* to achieve SM operation.

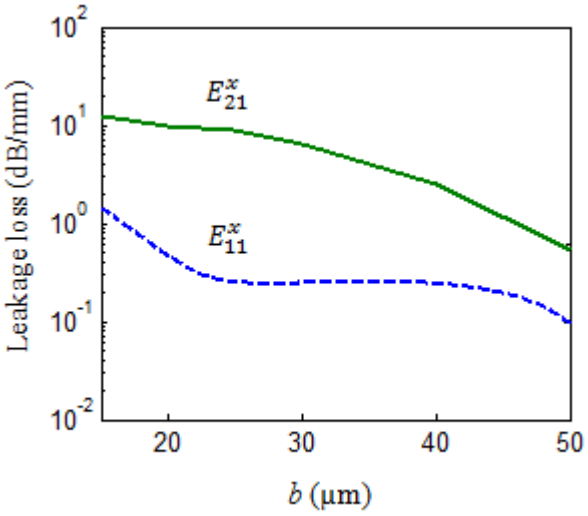

Fig. 4.6: The effect of the cladding parameter b on the leakage losses of the first two modes of the waveguide structure at 1.55 μm wavelength; when a =5 μm, q = 0.5, h = 10 μm, d = 1 μm, Λ = 6 μm and t = 4 μm.

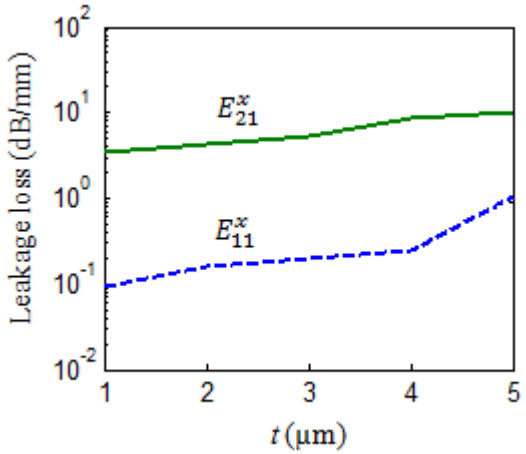

Fig. 4.7: The effect of the cladding parameter t on the leakage losses of the first two modes of the waveguide at 1.55 μm wavelength; when a = 5μm, b = 25 μm, h = 10 μm, q = 0.5, d = 1 μm and Λ = 6 μm.

4.3.2 Effect of the core parameters

The effect of the core parameters (*i.e.* core thickness *h* and width of core *a*) are studied and shown in Figs. 4.8 & 4.9, with cladding parameter *b* = 25 μm, *q* = 0.5 μm, *t* = 4 μm and λ = 1.55 μm. From Fig.4.8 it is clear that the leakage losses of both the modes decrease with increase in the thickness of core. High value of *h* provides better confinement to the modes inside the rectangular core. Thus, only a small portion of electrical field penetrates into the leaky cladding and reduces the loss of the mode.

Differential leakage loss increases with increase in h. $8 < h < 15$ µm are the allowed values of h for the designers to fabricate the waveguide for LMA SM operation.

Further, the effect of core width a is studied to find out the allowed range of core width for effective LMA operation. As illustrated in Fig. 4.9, due to enhancement in the confinement of the both the modes, the leakage losses decrease with core size. The absolute leakage loss reduces more rapidly with a. Thus, one has to be very careful while choosing the core width. The allowed values of core width for LMA SM are $4.3 < a < 5.6$ µm.

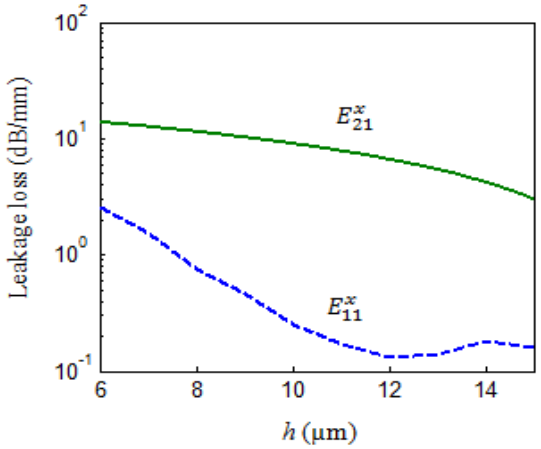

Fig. 4.8: The effect of the core parameter h on the Leakage losses of the first two modes of the waveguide at 1.55 µm wavelength when a = 5 µm, b = 25 µm, t = 4 µm, q = 0.5, d = 1 µm and Λ = 6 µm.

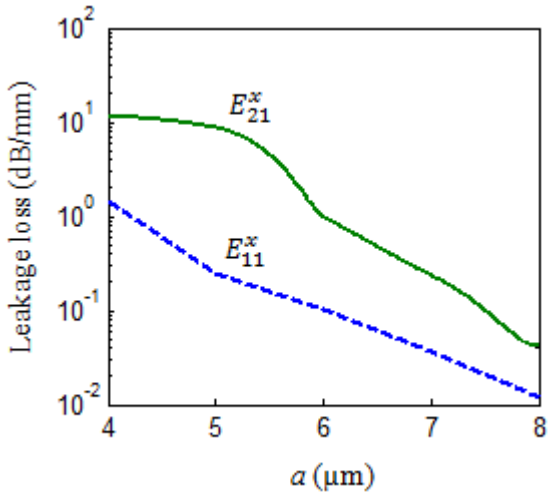

Fig. 4.9: The effect of the core parameter a on the Leakage losses of the first two modes of the waveguide at 1.55 µm wavelength when b = 25 µm, h = 10 µm, q = 0.5, t = 4 µm, d = 1 µm, and Λ = 6 µm.

4.3.3 Extended single-mode operation

The proposed channel waveguide exhibits extended SM operation due to dispersive cladding. To explain the extended SM operation characteristics of waveguide, the spectral variation of the leakage loss is studied and summarized in Fig. 4.10. The leakage loss of E_{21}^{x} mode is always larger than that of the E_{11}^{x} mode throughout the spectral range. At λ = 2.0 μm, E_{11}^{x} mode experiences 0.46 dB/mm, however, 4 dB/mm loss is experienced by E_{21}^{x} mode at λ = 1.25 μm. Thus, a 5 mm long waveguide is able to demonstrate the effectively SM over the entire spectral range of 1.25 – 2.0 μm without introducing more than 1 dB loss to fundamental mode. The core area of this channel waveguide structure is 100 μm^2. At λ = 1.55 μm, the E_{11}^{x} mode of waveguide suffers with 0.25 dB/mm leakage loss and E_{21}^{x} mode suffers with 8.73 dB/mm leakage loss. Therefore, 2.3 mm long waveguide can stripe off all the higher-order modes and ensure effective SM operation at 1.55 μm.

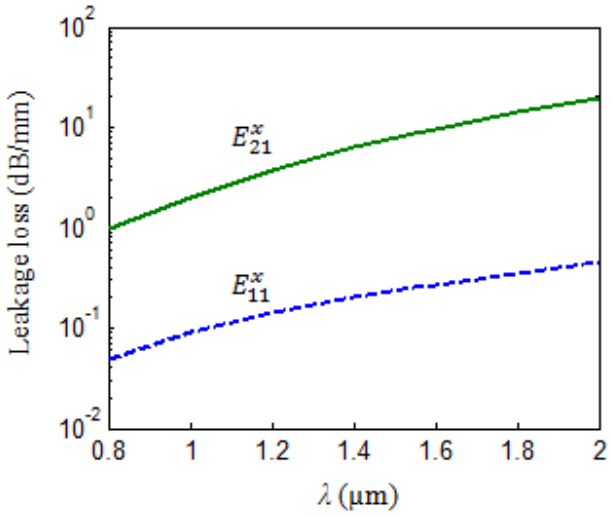

Fig. 4.10: The spectral variation of leakage losses on the first two modes of the waveguide when a = 5 μm, b = 25 μm, h = 10 μm, t = 4 μm, q = 0.5, d = 1 μm and Λ = 6 μm.

4.4. Conclusions

In this chapter, a large-mode-area multi-trench leaky channel waveguide structure has been reported. The proposed waveguide structure offers effective SM operation. The waveguide consists of a uniform rectangular large-core and the low-index trench assisted leaky multi-cladding. Initially waveguide is multimode. After a short distant when the entire higher order mode stripe off, the waveguide becomes single-mode. The effective mode-area of fundamental mode of the proposed channel waveguide

design is as large as 68.4 μm^2 at 1.55 μm wavelength. Simulated results show that the waveguide with core area as large as 100 μm^2 can provide effective SM operation over the spectral range from 1.25 – 2.0 μm. Such large-core channel waveguide can effectively able to suppress nonlinear optical effects and increase the power handling capability of the waveguide. This kind of waveguide structure has potential applications in high power delivery devices such as high-power waveguide lasers and amplifiers, high-power microwave detection and high-efficiency photovoltaic applications.

CHAPTER 5

Supercontinuum Generation in Photonic Crystal Fibers*

5.1 Introduction

SCG in optical fibers is an active and exciting research topic since last decade. Large number of new light sources have been created which are finding applications in different diverse fields such as optical coherence tomography [43, 103], optical communications [41], frequency metrology [104], fluorescence lifetime imaging [105], gas sensing [46, 106], food quality control [107] and early cancer diagnostics [47]. Supercontinuum is generated when a large number of nonlinear processes such as SPM, XPM, SRS and FWM act together upon a pump beam in order to cause extensive spectral broadening of the original pump beam. The breakthroughs in recent years have raised scientific concerns to understand and model how all these nonlinear processes interact together to generate supercontinuum and how parameters can be engineered to control and enhance the supercontinuum (SC) spectra.

The mid-infrared region is important because the fundamental molecular vibration absorption bands are stronger than the overtones and combination vibration absorption bands situated in the near-infrared region. Mid-infrared spectroscopy is able

*Parts of the results presented in this chapter have been reported in the research publications:

1. T. S. Saini, A. Kumar, R. K. Sinha, "Broadband mid-IR supercontinuum generation in As_2Se_3 based chalcogenide photonic crystal fiber: A new design and analysis," *Opt. Commun*. 347, 13 – 19 (2015)
2. T. S. Saini, A. Kumar, R. K. Sinha, "Broadband mid-infrared supercontinuum spectra spanning 2 – 15 μm using As_2Se_3 chalcogenide glass triangular-core graded-index photonic crystal fiber," *Journal of Lightwave Technol*. 33(18), 3914 – 3920 (2015)

to provide thorough understanding of the molecular structure of matter and to perform non-intrusive diagnostics of composite systems of physical, chemical and biological interest. SC spectra spanning visible to near-infrared in silica based fibers have been generated previously for various applications [108 – 110]. However, the broadening of SC spectra in silica fibers is limited by the strong material absorption beyond 2.5 μm wavelength, which effectively limits the spectral evolution into the mid-infrared region. For this reason a large number of non-silica glasses such as tellurite, ZBLAN, bismuth, fluoride and chalcogenide have been proposed for SCG in mid-infrared region [111 – 114].

Among all non-silica glasses, the chalcogenide glasses are excellent candidates for mid-infrared region because some of its compositions possess optical transparency upto 25 μm in this region [61]. The As_2Se_3 glass has shown excellent optical transparency between 0.85 – 17.5 μm with attenuation coefficient of less than 1 cm^{-1} [61]. In addition to broadband mid-infrared transmission window, chalcogenide glasses have also very large linear and nonlinear refractive indices which make them promising candidates for mid-infrared SCG [62]. *Shaw et al.* [115] presented an experimental demonstration of SCG in the spectral range from 2.1 to 3.2 μm using hexagonal structure of As_2Se_3 based chalcogenide PCF. Recently, *Hu et al*. [116] gave a design procedure, which can be used to maximize the band-width of supercontinuum generation in As_2Se_3 chalcogenide PCFs, for more than 4 μm band-width of SC. *Kubat et al.* [117] presented a numerical design optimization of ZBLAN fibers for mid-infrared SC sources using direct pumping with 10 ps pulses from mode-locked Yb and Er lasers to obtain broad spectra ranging from 1– 4.5 μm. *Klimczak et al.* [63] achieved SC broadening between 930 nm to 2170 nm spectral range using all-solid soft glass microstructured optical fiber. In Ref. [118] the authors have experimentally demonstrated the SCG covering 0.9− 9 μm with the help of commercially available ZBLAN fiber and commercially available chalcogenide PCF. Recently, *Kubat et al.* [52] presented numerical modelling of broadband mid-infrared SCG spanning from 3 – 12.5 μm in step-index fiber pumped at 4.5 μm with 0.75 kW pump power. *Petersen et al.* [53] demonstrated broadband mid-infrared supercontinuum spectra covering the range of 1.4 – 13.3 μm in mid-infrared regime using ultra-high NA chalcogenide step-index fiber.

In comparison to SCG in standard optical fibers, PCF requires input laser pulses

with very less initial peak power. The higher order dispersion effects are stronger in PCF and play a much more significant role in pulse propagation. The dramatic spectral broadening with relatively low-intensity laser pulses in PCF is very interesting phenomena and can be used in various fascinating applications such as frequency metrology.

The broadening mechanism of supercontinuum spectrum mainly depends upon the dispersion profile of optical fiber structure as well as input pulse characteristics. In the anomalous group velocity dispersion regime when highly intense laser pulse incident on nonlinear medium it evolves towards the higher-order solitons [41]. For the femtosecond pumping, the higher-order solitons are affected by the higher-order dispersion and stimulated Raman scattering. Consequently, the higher order solitons become unstable and breakup into several fundamental solitons through the fission process. Such chaotic soliton fission process causes shot-to-shot noise in the supercontinuum spectrum [119, 120]. But in case of normal group velocity dispersion regime, for femtosecond pulses SPM is the only reason for ultra wide spectral broadening [120]. This makes such broad-band SC suitable for time-resolved applications such as optical coherence tomography, pump-probe spectroscopy and nonlinear microscopy. One of the possibilities for generating SC in the normal dispersion regime is to pump the fiber far below the zero dispersion wavelength (ZDW), so that the generated spectrum does not extend into the anomalous dispersion region. However, this would require high power or very short pulses to overcome the short effective interaction length due to high value of dispersion. It is worthwhile to mention here that the broadening of SC demonstrated in [53] is the largest achieved in fiber geometry till date. However, possibility of broadening of SC spectra beyond 20 μm is being discussed in scientific news and views [121].

Mid-infrared domain in the range of 2 – 15 μm of electromagnetic spectrum is of particular importance because of the molecular fingerprint of biological tissue lie within this domain. This domain is useful to determine a tissue spectral map which provides very important information about the existence of diseases such as cancer. Therefore, it is necessary to develop broadband supercontinuum sources in mid-infrared domain. The chalcogenide glasses have this potential to provide such broadband mid-infrared supercontinuum sources.

In this chapter, analysis, design and numerical modeling of two novel PCF geometries (i.e., triangular-core PCF and triangular-core-graded-index PCF) are

presented for ultra broadband mid-infrared supercontinuum spectra spanning 2 – 15 μm. To obtain efficient broadband supercontinuum spectrum in mid-infrared regime, proposed structures have been specifically designed for all-normal dispersion characteristic. Such broadband mid-infrared supercontinuum spectrum is obtained in relatively short length (*i.e.* 5 mm) of PCF, using a sub-harmonic generation source of the mode-locked thulium 50 fs pulsed fiber laser at 4.1μm [122].

5.2 Method of Analysis

5.2.1 Linear characteristics of PCF structure

To simulate the effective index of fundamental mode propagating through proposed triangular-core graded-index photonic crystal fiber, a full vectorial FEM based software 'COMSOL Multiphysics' has been employed. For calculating the wavelength dependent refractive index of As_2Se_3 based chalcogenide material following two terms Sellmeier equation has been used [123].

$$n^2 - 1 = A_0 + \sum_{n=1}^{2} \frac{A_n \lambda^2}{\lambda^2 - a_n^2} \qquad (5.1)$$

In above Eq. (5.1) A_0, A_n and a_n are the sellmeier coefficients with A_0=3.3344, A_1=3.3105, A_2=0.89672, a_1=0.43834 μm and a_2=41.395 μm for As_2Se_3 based chalcogenide glass which we have used as a fiber material in this work.

The group velocity dispersion plays an important role in SCG because it determines the extent to which different spectral components of an ultra-short pulse propagate at different phase velocities in the photonic crystal fiber. The group velocity dispersion $D(\lambda)$ is calculated from wavelength dependent effective indices of propagating mode using the following relation [41]

$$D(\lambda) = -\frac{\lambda}{c} \frac{\partial^2 Re(n_{eff})}{\partial \lambda^2} \qquad (5.2)$$

where, c is the velocity of light in free space, $Re(n_{eff})$ is the real part of the effective index. Both material and waveguide dispersion are included in the above equation as Sellmeier equation is taken into account while calculating n_{eff}.

The effective area of propagating mode in the PCF is calculated using the relation given below [41, 52].

$$A_{eff} = \frac{\left(\iint_{-\infty}^{\infty} |E|^2 \, dx \, dy\right)^2}{\left(\iint_{-\infty}^{\infty} |E|^4 dx \, dy\right)} \qquad (5.3)$$

where, E is the electric field distribution derived by solving the eigenvalue problem drawn from Maxwell's equations.

5.2.2 Nonlinear characteristics of PCF structure

Nonlinearity in PCF is the most important parameter which must be studied more rigorously in order to get accurate results. The nonlinear coefficient (γ), offered by PCF structure, related to the nonlinear refractive index of material of PCF and the effective area of propagating mode as follows [41]

$$\gamma = \frac{2\pi n_2}{\lambda A_{eff}(\lambda)} \qquad (5.4)$$

where, n_2 is the nonlinear refractive index of material (n_2 = 5.2×10^{-18} m^2/W at 4.5 μm wavelength [52]), λ is the pump wavelength and A_{eff} is the effective area of fundamental mode and its value depends on the wavelength. For broader supercontinuum spectra the nonlinear refractive index (*i.e.* n_2) should be as high as possible and A_{eff} should be as small as possible. Wavelength dependent effective mode area is obtained using Eq.(5.3) as mentioned in Ref. [52]. The value of γ can be enhanced by taking material with high non linear refractive index and/or by designing a PCF with lower effective mode area.

To simulate SC spectrum, the following GNLSE has been solved for output pulse envelope, A (z, t) using split-step Fourier method [108]

$$\frac{\partial A}{\partial z} + \frac{\alpha}{2}A - \left(\sum_{n\geq 2} \beta_n \frac{i^{n+1}}{n!}\frac{\partial^n A}{\partial t^n}\right) = i\gamma\left(1 + \frac{i}{\omega_o}\frac{\partial}{\partial t}\right)\left[A(z,t)\int_{-\infty}^{\infty} R(t') \; |A(z,t-t')|^2 dt'\right] \qquad (5.5)$$

The left hand side of Eq. (5.5) deals with linear propagation effects while the right hand side of this deals with nonlinear effects of PCF structure. α represents the power losses in the PCF as the light travels through it. We have included both the material and confinement losses in all the simulations. A constant material loss coefficient of 0.6 cm^{-1} has been considered for 2 – 15 μm spectral range [61]. For designed triangular core graded index (TCGI) PCF the typical value of simulated

confinement loss is ~3.9×10^{-5} dB/mm at 4.1 μm. The propagation constant (β) at any frequency (ω), relative to pulse central frequency(ω_0), can be expanded as Taylor series expansion [108]

$$\beta(\omega) = \beta(\omega_0) + \beta_1(\omega_0)(\omega-\omega_0) + \frac{1}{2!}\beta_2(\omega_0)(\omega-\omega_0)^2 + \frac{1}{3!}\beta_3(\omega_0)(\omega-\omega_0)^3 + \cdots \quad (5.6)$$

where, $\beta_n(\omega_0) = \frac{d^n\beta}{d\omega^n}$, first term in the right hand side of Eq. (5.6) gives the effective refractive index of the propagating mode and the second and third terms are related to the group velocity and the group velocity dispersion (GVD) of the pulse respectively. We have evaluated higher order dispersion up to the order of 9th from the group velocity dispersion curve.

R (t') is the nonlinear response function and takes account of the electronic and nuclear contributions and expressed as follows:

$$R(t') = (1-f_R)\delta(t'-t_e) + f_R\, h_R(t') \quad (5.7)$$

where, f_R is the fractional contribution of the Raman response to the total linear response. For As_2Se_3 chalcogenide glasses the fractional contribution f_R=0.115 [124]. The electronic contribution is treated in this analysis as occurring instantaneously because $t_e \approx 1$ fs. $h_R\,(t')$ is the Raman response function and contains information on the vibration of material molecules as light passes through the fiber.

The Raman response function $h_R\,(t')$ can be calculated by most common and approximate analytic form which is given by the following relation:

$$h_R(t') = \frac{\tau_1^2+\tau_2^2}{\tau_1\tau_2^2}\, exp\left(-\frac{t'}{\tau_2}\right)\sin\left(\frac{t'}{\tau_1}\right) \quad (5.8)$$

where, Raman period τ_1=23.1fs and life time τ_2=195 fs for As_2Se_3 based glasses [124].

In our study, we consider the hyperbolic secant pulse as input pulse which is expressed as the relation given below:

$$A(z=0,t) = \sqrt{P_0}\,.sech\left(\frac{t}{t_o}\right) \quad (5.9)$$

where, $t_0=T_{FWHM}/1.7627$ and P_0 is peak power of input pulse. T_{FWHM} is pulse width (*i.e*. the full-width at half maximum of input pulse).

5.3 Design of Triangular Core PCF

A new TC PCF structure with four layers of air holes arranged in triangular lattice pattern in As_2Se_3-based chalcogenide glass has been designed as shown in Fig. 5.1 (a). Three air holes have been removed from the centre to make triangular-core of the PCF. The center to center distance of holes is taken as constant and represented by Λ. The diameter of air holes in first, third and fourth rings have been considered identical and defined by d_1, while the diameter of air holes in second ring is d_2, which is comparatively larger than d_1. Simulated electric field distribution of propagating mode in proposed TC PCF at operating wavelength of 4.5 μm has been shown in Fig.5.1 (b).

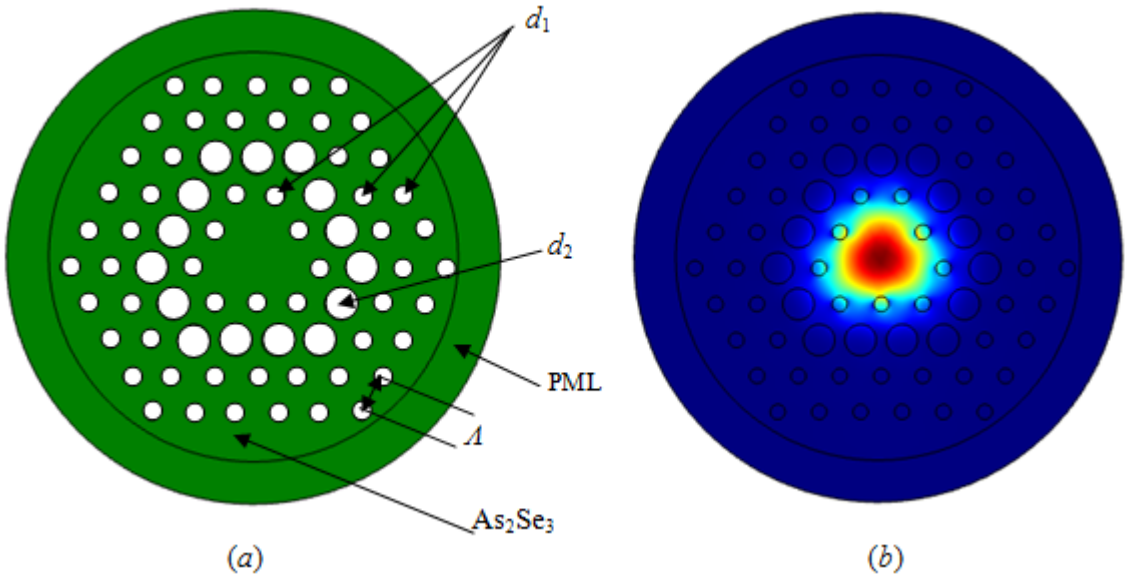

Fig. 5.1: (a) The transverse cross-section of the proposed TC PCF structure; (b) The electric field distribution of the propagating mode at 4.5 μm.

5.3.1 Results and discussion

In order to obtain efficient ultra-broad-band SC in proposed TC PCF, the structural parameters (*i.e.* Λ, d_1 and d_2) are optimized for all-normal flat-top dispersion. For this purpose, initially the effect of various values of pitch (Λ) on dispersion characteristic have been simulated while keeping other parameters fixed (*i.e.* d_1 = 420 nm and d_2 = 820 nm) within the spectral range from 2.5 μm to 5.5 μm. This feature of structure has been shown in Fig. 5.2. It is to be noted that, at Λ = 1 μm the dispersion curve lies in both normal and anomalous dispersion regime and it start to shift towards normal

dispersion regime on increasing the value of Λ. When Λ = 1.2 μm the dispersion curve lies in normal regime within the entire spectral range of 2.5 – 5.5 μm.

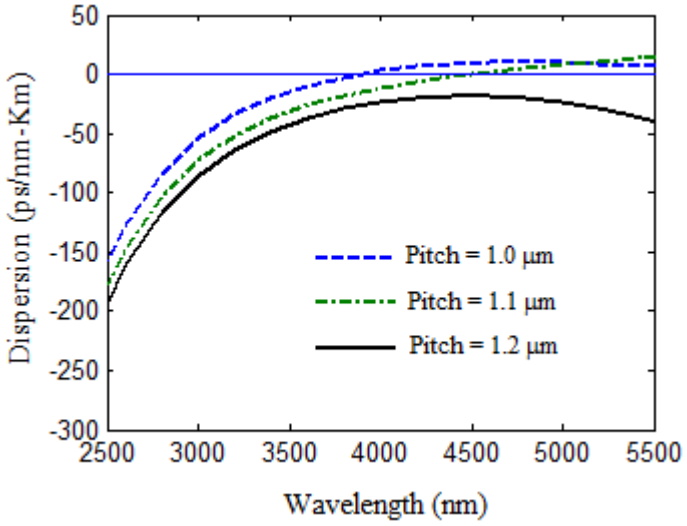

Fig. 5.2: Influence of the pitch (Λ) on dispersion characteristics of proposed structure while keeping other parameters fixed (i.e. d_1= 420 nm and d_2 = 820 nm).

Now, influence of the hole diameter, d_1 (while keeping other parameters fixed; *i.e.* Λ = 1.2 μm and d_2 = 820 nm) on the dispersion characteristics of proposed structure has been illustrated in Fig. 5.3. It is clear from this figure that the dispersion characteristic does not change significantly on changing d_1. Therefore, it seems very difficult to get desire dispersion characteristic of structure using d_1. However, dispersion characteristic of structure can be tuned easily with air hole diameter d_2 in second ring of PCF structure. This feature of proposed structure has been illustrated in Fig. 5.4. The dispersion curve starts to shift toward the anomalous dispersion regime from normal dispersion regime on increasing d_2. It is to be noted that all-normal flat-top dispersion characteristic with dispersion value approximately -2 ps/(nm.km) within the spectral range from 4.4 μm to 4.8 μm can be achieved when d_2 = 900 nm. The above analysis and simulated results lead us to conclude that by careful choice of the structural parameter d_2 one can control and obtain the desired dispersion characteristic of proposed TC PCF.

The confinement loss of propagating mode in the spectral range of 2 – 10 μm is shown in Fig. 5.5. At pump wavelength, (*i.e.* 4.5 μm) the structure offers 0.03 dB/mm loss for propagating mode. For optimized geometrical parameters (as shown in Table-5.1), the wavelength dependent effective mode area of propagating mode and

corresponding nonlinear coefficient have been illustrated in Fig. 5.6. Simulated results show that the proposed TC PCF structure offers nonlinear coefficient (γ) as high as 5449 $W^{-1}km^{-1}$ with effective mode area of 6.15 μm^2 at 4.5 µm input pulse wavelength.

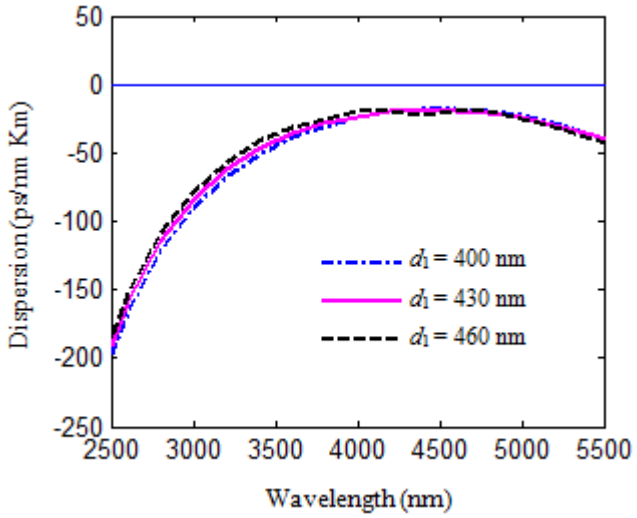

Fig. 5.3: Influence of the hole diameter (d_1) on dispersion characteristics of proposed structure while keeping other parameters fixed (i.e. Λ = 1.2 µm and d_2 = 820 nm).

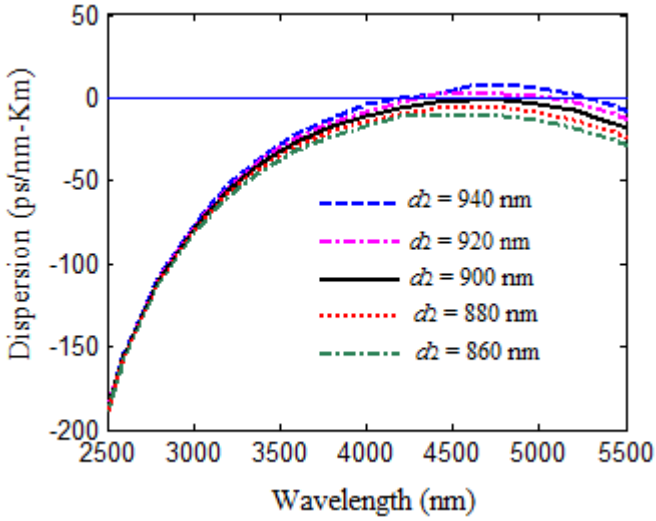

Fig. 5.4: Influence of the hole diameter (d_2) on the dispersion characteristics of proposed structure while keeping other parameters fixed (i.e. Λ = 1.2 µm and d_1 = 430 nm).

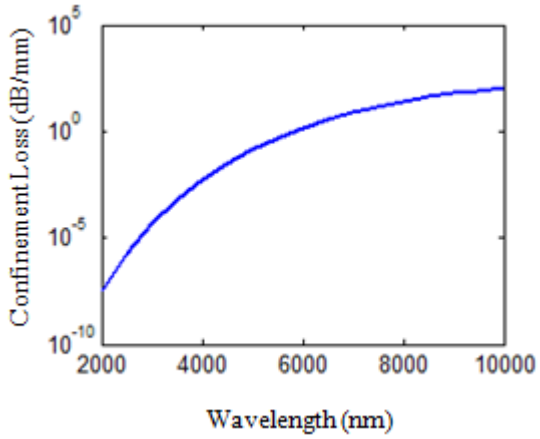

Fig. 5.5: The confinement loss of propagating mode of proposed TC PCF when Λ = 1.2 μm, d_1 = 430 nm and d_2 = 900 nm.

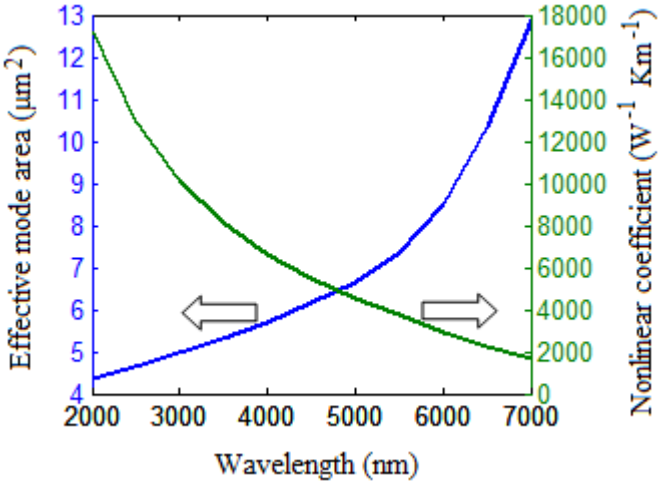

Fig. 5.6: The variation of effective mode area of propagating mode and corresponding nonlinear coefficient of proposed TC PCF with optimized parameters.

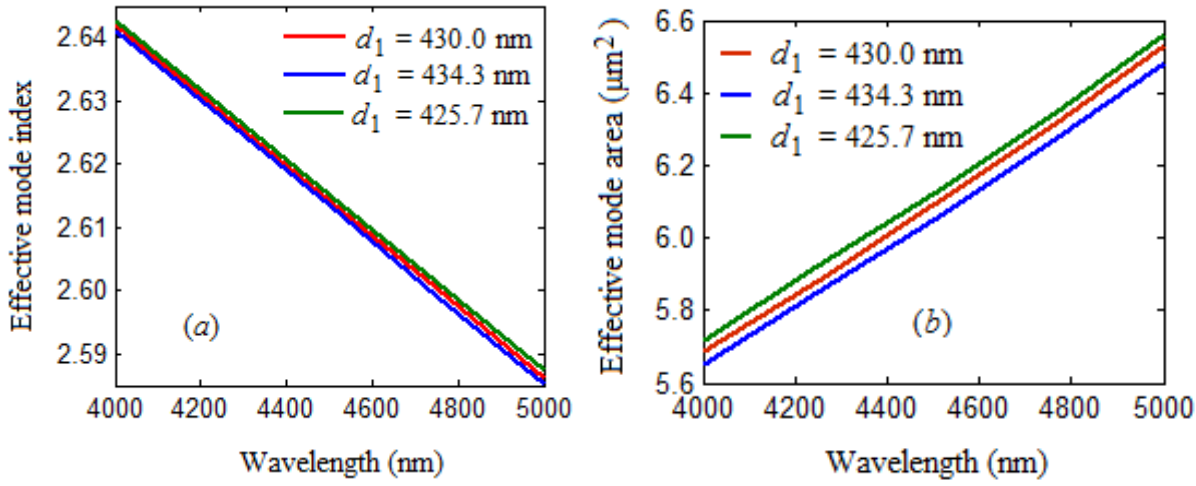

Fig. 5.7: Tolerance analysis of d_1: (a) The effect on the effective mode index with ±1% deviation in d_1; (b) effect on the effective mode area with ±1% deviation in d_1.

In order to get flat, smooth and broad supercontinuum spectra the pump wavelength is selected at 4.5 μm in normal dispersion regime with very small dispersion value of -2 ps/nm×Km for the proposed TC PCF. In the simulation study, the peak power of incident pulse is 700 W with full-width at half maximum of 50 fs. The calculated output spectra with different propagating length of PCF have been shown in Fig. 5.8. It has been observed that the spectral bandwidth starts to be broadened in only a few millimeter of propagation length.

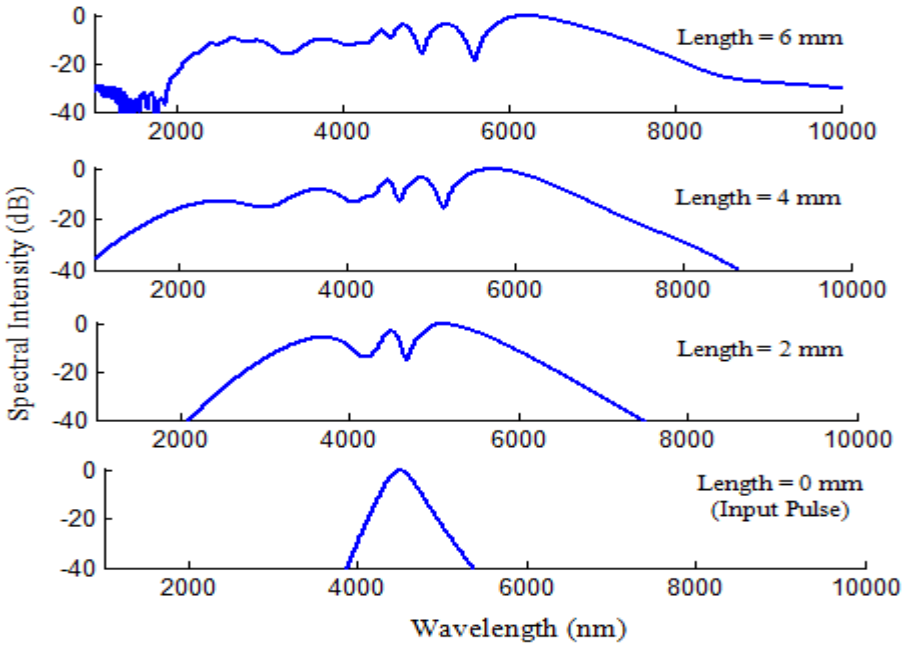

Fig. 5.8: Broadening of output spectra obtained at various lengths of TC PCF when peak power of incident pulse = 700 W and pulse duration = 50 fs.

This feature of structure can be interpreted by comparing the nonlinear and dispersion length. The calculated values of nonlinear length ($L_{NL} = 1/\gamma P_0$) and dispersion length ($L_D = t_0^2/\beta_2$) for proposed TC PCF are 2.62×10^{-4} m and 6.49×10^{-2} m respectively at 4.5 μm pump wavelength. Since the nonlinear effect is stronger than dispersion effect, many of the new spectral components would be generated in a short length. After that the spectrum gets broadened due to the group velocity dispersion (GVD) effect. It is to be noted that the output spectrum becomes constant in the 1.9 – 10 μm spectral range at the PCF length of 6 mm. In the initial phase of pulse propagation, SPM is responsible for symmetrical spectral broadening. As the PCF length is further extended, the Raman effect comes into account and extends the SC.

Within 6 mm length of PCF an ultra-broadband SC extending from 1.9 – 10 μm at -30 dB level has been generated with peak power of 700 W and 50 fs duration of input pulse. The power level up to -30 dB is considered to compare the results with Ref. [45]. With further propagation the SC spectra does not change anymore.

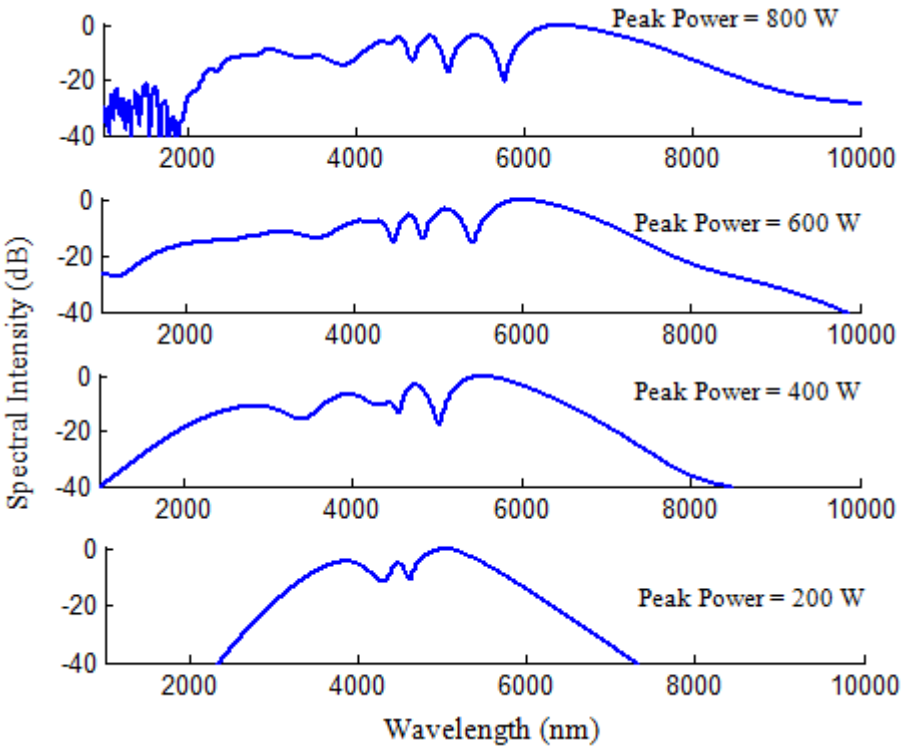

Fig. 5.9: Influence of input peak power on the broadening of output spectra with 50 fs incident pulse in 6 mm length of TC PCF.

Figure 5.9 illustrates the influence of input peak power on the bandwidth of output spectral intensity in 6 mm long PCF. The full-width at half maximum of the input pulse is fixed at 50 fs. Initially, the output spectra get broadened as the peak power of incident pulse increases. At high peak power, SPM effect dominants over dispersion effect. It has been observed that the maximum broadening in SC spectra is achieved at 700 W. Beyond this, no significant change in broadening has been observed, however, the flatness of SC spectra increases with further increase in peak power.

Finally, the influence of T_{FWHM} on the bandwidth of output spectral intensity in 6 mm long PCF has been shown in Fig. 5.10. The input peak power is fixed at 700 W. It is clear from the figure that output spectra become narrow with increase in T_{FWHM}. This

is due to SPM effect. It is to be noted that the short pulse is better to get broader SC spectra. The optimized values of input pulse are summarized in Table 5.2. It is to be mentioned that the coherence is also an important property of the SC spectra. However, in the current work, our focus is on the broad bandwidth of SC spectra using low pump power in a very small length of proposed TC PCF. Flatness and the coherence property is the subject of further investigation.

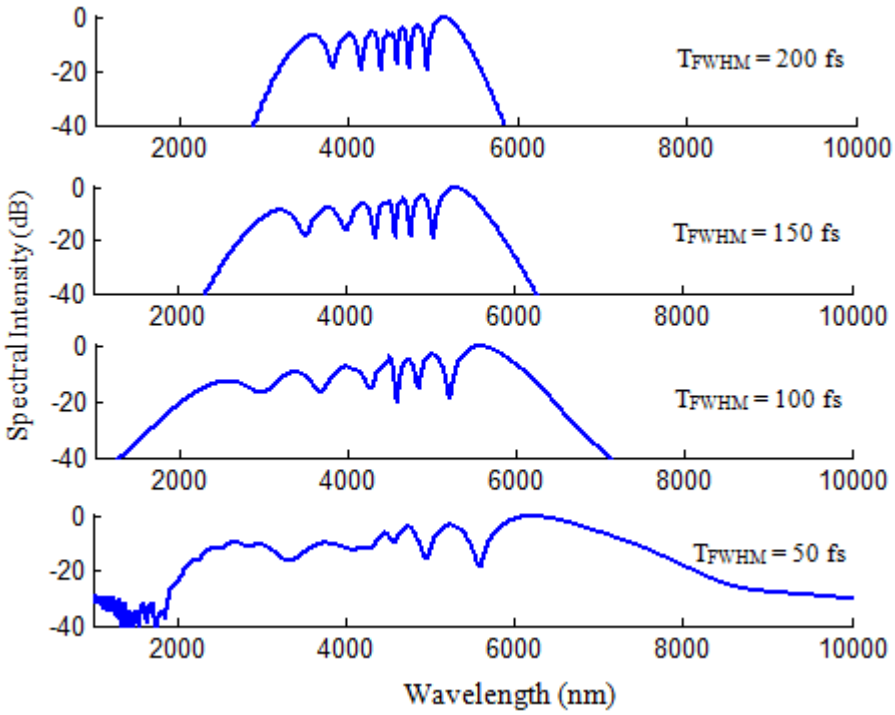

Fig. 5.10: Influence of full-width at half maximum of the input pulse on the broadening of output spectra with 700 W peak power in 6 mm length of PCF.

Table 5.1: Geometrical parameters of proposed TC PCF

Parameter name	Pitch	d_1	d_2
Parameter value	1.2 µm	430 nm	900 nm

Table 5.2: Input pulse parameters for proposed TC PCF

Parameter name	Peak power	T_{FWHM}	Pulse shape
Parameter value	700 W	50 fs	hyperbolic secant

5.3.2 Tolerance analysis of TC PCF strucrue

For fabrication purposes it is also very important to investigate the tolerance of the proposed structure with respect to the various design parameters. After investigating the effect of small variations in the values of d_1, d_2 and Λ, it is found that the magnitude of dispersion and the effective mode area of propagating mode are less sensitive to the structural parameters. As shown in Fig. 5.7 (*a* & *b*), at 4.5 μm wavelength 1% deviations in d_1 changes the effective index value by ~ 0.03 % and it also changes the effective mode area by ~ 0.56 %. Similarly, 1% deviation in d_2 changes the effective index by ~ 0.01 % and changes the effective mode area by 0.40% while, 1% deviation in Λ changes the effective index by 0.13 % and changes the effective mode area by 2.31 %. From the manufacturing point of view our proposed structure can be fabricated by standard extrusion and stacking methods.

5.4 Design of Triangular Core Graded Index PCF

A novel TCGI PCF structure with four layers of air holes arranged in triangular lattice pattern in As_2Se_3-based chalcogenide glass is presented. As shown in Fig. 5.11 (*a*) three air holes have been removed from the centre to construct a triangular-core of the PCF. The center to center distance of air holes is taken as constant and represented by Λ. The diameters of air holes in first, second, third and fourth ring are d_1, d_2, d_3 and d_4 respectively. For our design $d_1 < d_2 < d_3 < d_4$, *i.e.* the air filling fraction (d_n/Λ, n = 1, 2, 3, 4) of cladding increases with *'n'*. Where *'n'* is the number of rings of air holes. In other words the effective refractive index of cladding successively decreases for first, second, third and fourth rings of air holes. That is why the structure of PCF is named as 'graded-index'. The structure is surrounded by the cylindrical perfectly matched layer (PML) for eliminating the back reflection effect at the boundary. The reason of designing triangular-core of PCF is to get all-normal and nearly zero dispersion characteristic at desire pump wavelength. Graded index profile increases the confinement which gives higher nonlinearity and therefore TCGI PCF is selected for ultra broadband SCG. Simulated electric field distribution of propagating mode in proposed triangular-core graded-index PCF at 4.1 μm has been illustrated in Fig.5.11 (*b*).

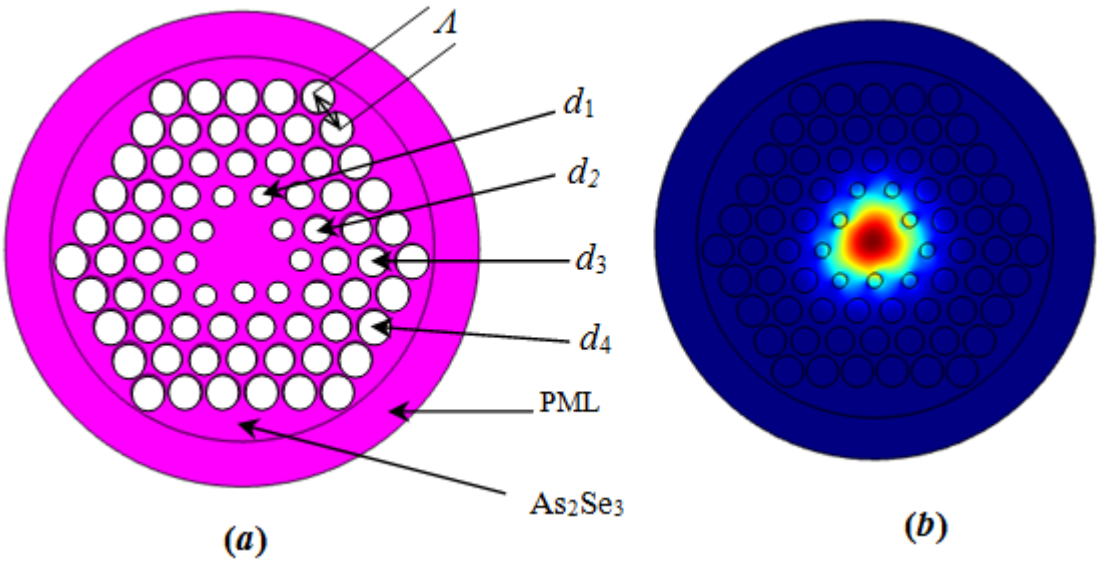

Fig. 5.11: (a) The transverse cross-section of proposed TCGI PCF; (b) the electric field distribution of propagating mode in PCF at 4.1 μm.

5.4.1 Results and discussion

In order to obtain ultra broadband SC in proposed PCF structure, the structural parameters (*i.e.* Λ, d_1, d_2, d_3 and d_4) have been optimized to achieve all-normal chromatic dispersion profile. The effect of various values of air hole diameter in first ring, d_1 on dispersion characteristic, while keeping other parameters fixed, is illustrated in Fig. 5.12. Similarly the effect of diameter of air holes in second ring on the dispersion profile of proposed triangular-core PCF is shown in Fig. 5.13. It is to be noted here that the effect of the diameter of air holes in third and fourth ring are relatively less sensitive on dispersion characteristic of proposed PCF structure (not shown in figure).

For optimized geometrical parameters (as shown in Table-5.3), the chromatic dispersion profile of proposed TCGI PCF is shown in Fig. 5.14. The proposed PCF structure offers flat dispersion across 3.35 – 4.20 μm spectral range within the dispersion value of approximately –2 ps/(nm×Km). Confinement loss is very improtant parameter for generating SC spectra in fibers. We have simulated the confinement loss of our proposed PCF structure and shown in Fig. 5.15. Proposed PCF structure offers low confinement loss of ~ 3.9×10^{-5} dB/mm at pump wavelength (*i.e.* 4.1μm). However, the loss at 10 μm is ~14 dB/mm. Since the higher wavelengths (> 8 μm) generate at 5

mm length of the PCF, the broadening of supercontinumm spectrum would not be affected by higher losses at higher wavelengths.

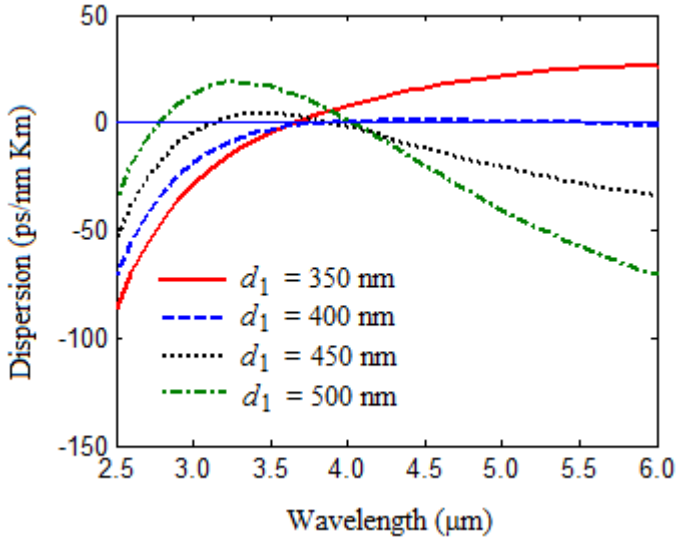

Fig. 5.12: The effect of the diameter of the air holes in first ring (i.e. d_1) on chromatic dispersion profile while keeping other parameters fixed as: d_2 = 700 nm, d_3 = 800 nm, d_4 = 900 nm, and Λ = 1000 nm.

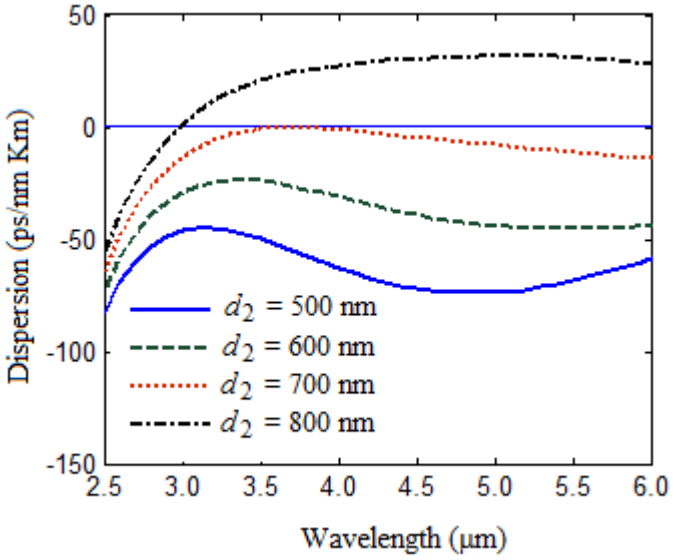

Fig. 5.13: The effect of the diameter of the air holes in second ring (i.e. d_2) on chromatic dispersion profile while keeping other parameters fixed as: d_1 =420 nm, d_3 =800 nm, d_4 =900 nm, and Λ =1000 nm.

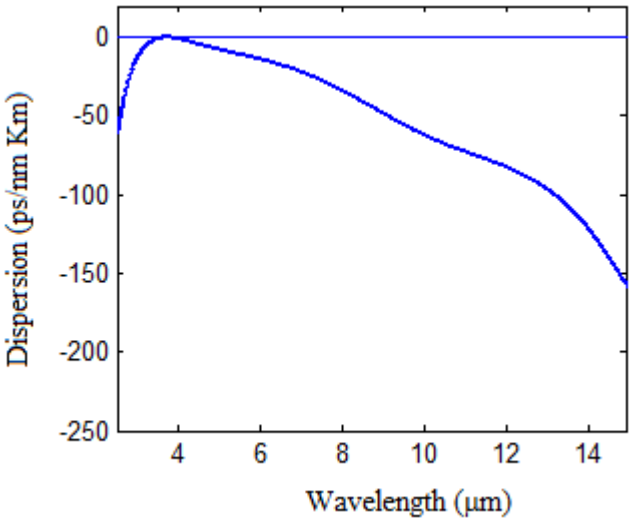

Fig. 5.14: The chromatic dispersion characteristic of proposed TCGI PCF structure with optimized parameters (i.e. d_1 = 420 nm, d_2 = 700, d_3 = 800 nm, d_4 = 900 nm, and Λ = 1000 nm).

The wavelength dependent EMA of propagating mode and corresponding nonlinear coefficient is illustrated in Fig. 5.16. Simulated results show that the proposed TCGI PCF structure offers nonlinear coefficient (γ) as high as 1944 $W^{-1}\times Km^{-1}$ with EMA of 4.1 μm^2 at 4.1 μm input pump wavelength. As illustrated in Fig. 5.17, by launching the laser pulses of proper parameters (pulse parameters are shown in Table-5.4) we are able to obtain broadband spectra ranging 2 – 15 μm in only 5 mm length of proposed TCGI PCF. The calculated values of nonlinear length ($L_{\mathrm{NL}} = 1/\gamma P_0$) and dispersion length ($L_{\mathrm{D}} = \frac{T_0^2}{\beta_2}$; $T_0 = T_{\mathrm{FWHM}}/1.763$), for proposed TCGI PCF are 1.47×10^{-4} m and 5.2×10^{-2} m respectively for 50 fs laser pulse at 4.1 μm. Within 5 mm length of the TCGI PCF an ultra-broadband SC extending from 2 – 15 μm has been generated with 50 fs laser pulses of peak power of 3.5 kW. As shown in Fig. 5.17, beyond 5 mm length of the proposed structure, the broadening of SC spectra does not increase significantly. This is because of the lower nonlinearity and higher losses corresponding to higher wavelengths (> 15 μm) for proposed TCGI PCF structure.

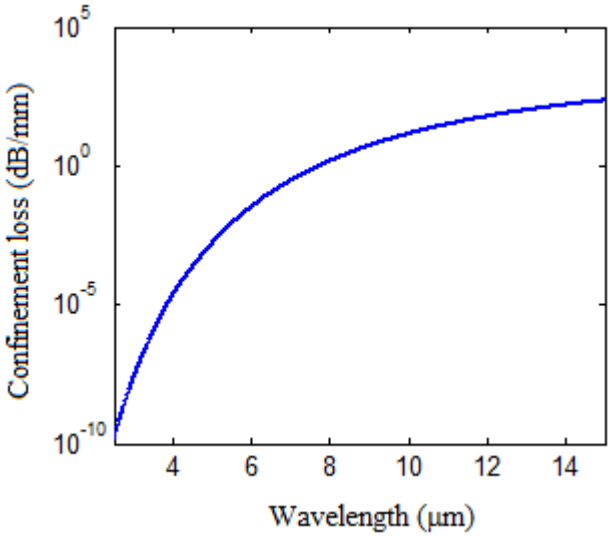

Fig. 5.15: The confinement loss of proposed triangular-core graded-index photonic crystal fiber structure with optimized parameters (i.e. d_1 = 420 nm, d_2 = 700, d_3 = 800 nm, d_4 = 900 nm, and Λ = 1000 nm).

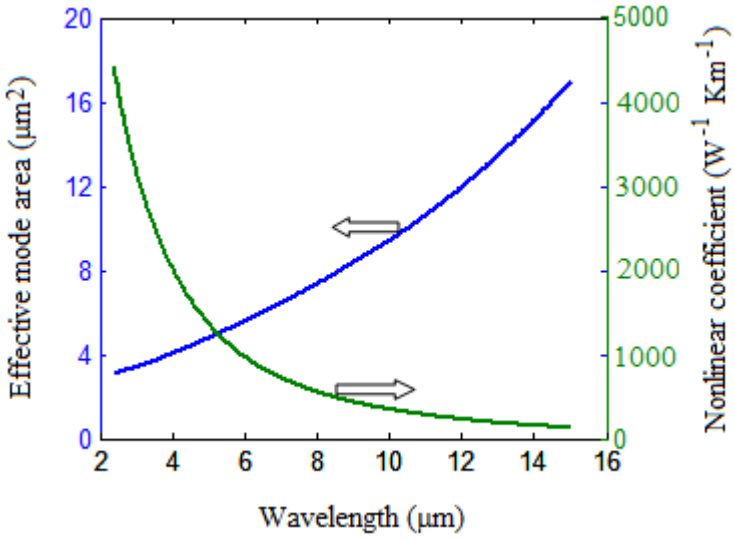

Fig. 5.16: The variation of effective mode area of propagating mode and corresponding nonlinear coefficient of proposed triangular-core graded-index photonic crystal fiber with optimized parameters (i.e. d_1 = 420 nm, d_2 = 700, d_3 = 800 nm, d_4 = 900 nm, and Λ = 1000 nm).

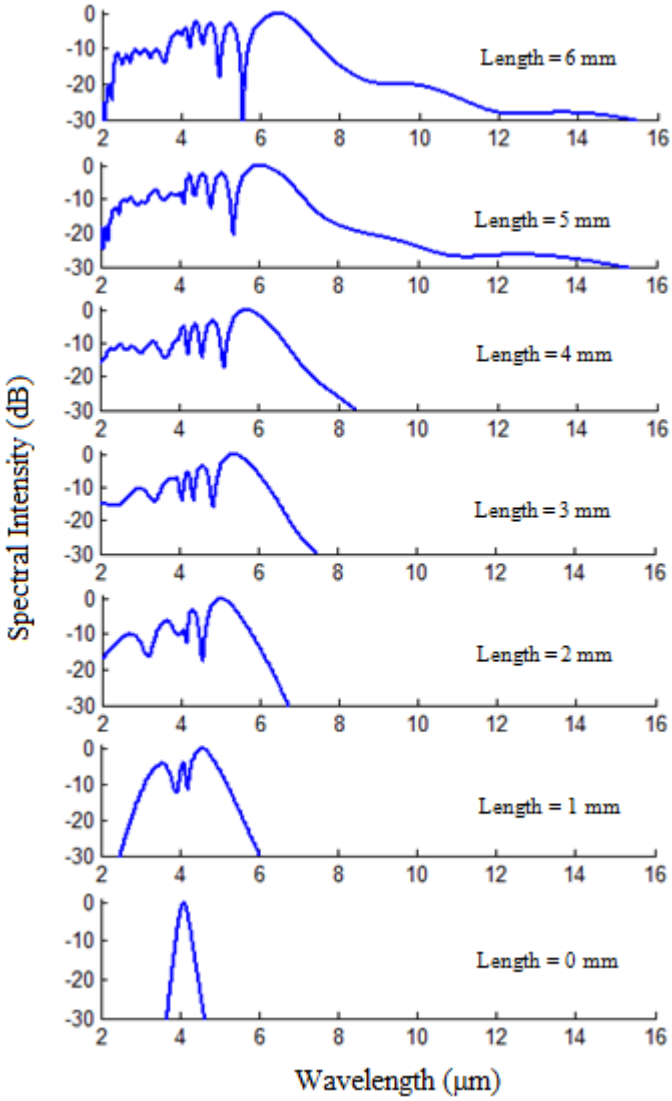

Fig. 5.17: Spectral broadening of supercontinuum spectra from various length of PCF; when 50 fs laser pulses with peak power of 3.5 kW launched at proposed triangular-core graded-index PCF structure.

Finally, the influence of the input pulse width *i.e.* full width at half maximum on the bandwidth of output spectrum in 5 mm long TCGI PCF has been revealed in Fig. 5.18. The input peak power is fixed at 3.5 kW. When the value of T_{FWHM} increases the output spectra start to get narrower. This is due to the SPM effect. It is to be noted here that the short pulse is better to get broader SC spectra. The optimized values of input pulse are summarized in Table-5.4.

5.4.2 Tolerance analysis of TCGI PCF structure

After investigating the effect of small variations in the values of d_1, d_2, d_3, d_4 and Λ we have found that the magnitude of dispersion and the EMA of propagating mode are less sensitive to the structural parameters. For example, at 4.1 μm wavelength 1% variation

in d_1 changes the dispersion value by ~ 4 % and changes the effective mode area by 0.8%. These changes produce only ~1% changes in the spectral broadening of SC spectra. Proposed TCGI PCF structure can be fabricated by standard extrusion and stacking based methods.

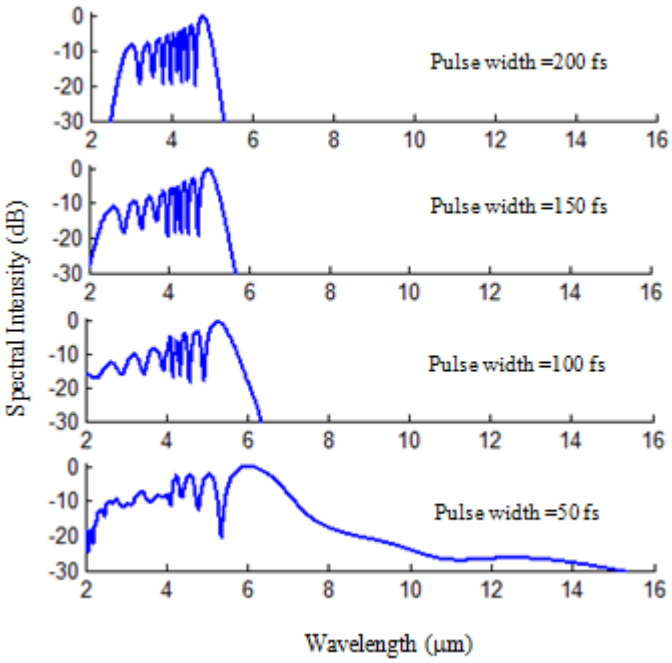

Fig. 5.18: Broadening of output spectra from 5 mm long TCGI PCF obtained at various values of T_{FWHM} when peak power of incident pulses = 3.5 kW.

Table 5.3: Geometrical parameters of proposed TCGI PCF

Parameter name	Pitch	d_1	d_2	d_3	d_4
Parameter value	1000 nm	420 nm	700 nm	800 nm	900 nm

Table 5.4: Input pulse parameters for proposed TCGI PCF

Parameter name	Peak power	T_{FWHM}	Pulse shape
Parameter value	3.5 kW	50 fs	hyperbolic secant

5.5 Conclusions

Two new designs (*i.e.*, TC PCF & TCGI PCF) of PCFs in As_2Se_3 based chalcogenide glass have been presented in this chapter for mid-infrared supercontinuum generation. Proposed TC PCF structure is able to offer ultra-broadband SC spectrum spanning 1.9 – 10 µm at the -30 dB level using only 6 mm long PCF pumped with 50 fs laser pulses of peak power of 700 W at 4.5 µm. Ultra-broadband SCG in mid-infrared regime covering atmospheric transparent windows (*i.e.* 3 – 5 µm, and 8 – 13 µm of spectrum region) and the molecular ‘fingerprint region’ from 2 – 15 µm, is achieved using 5 mm long PCF pumped with 50 fs laser pulses from mode-locked Tm-doped fiber laser of peak power of 3.5 kW at 4.1 µm. These PCF structures can be a good candidate for generating efficient supercontinuum which is applicable for various nonlinear applications such as optical coherence tomography, metrology, and frequency combs generation, gas sensing, food quality control and early cancer diagnostics.

CHAPTER 6

Equiangular Spiral Photonic Crystal Fiber for Supercontinuum Generation*

6.1 Introduction

Mid-infrared SCG is one of the most exciting research topics due to its major impact on spectroscopy, security and molecular sensing. In order to obtain broadband supercontinuum spectra in mid-infrared region, several efforts have been made during the last few years. Supercontinuum spectrum extending from 800 – 2500 nm has been observed in a regular hexagonal – lattice tellurite PCF using 150 fs long pulses at 1580 nm [125]. Mid-IR SC spectra spanning 1.795 – 6.525 μm has been achieved using only 8 mm length of As_2Se_3 nanofiber with input pulse energy of 100 nJ [126]. SCG covering 0.9– 9 μm has been demonstrated experimentally with the help of commercially available ZBLAN fiber and commercially available chalcogenide PCF [118]. In Chapter-5 of this thesis two novel PCF geometries for ultra broadband mid-infrared supercontinuum spectrum have been reported.

In this chapter, an ES PCF in As_2Se_3 chalcogenide glass has been designed for mid-infrared supercontinuum generation. A full vectorial finite element method has been used to investigate the dispersion properties of the proposed fiber. Simulated results show that the proposed ES PCF structure is highly nonlinear with very low and flat dispersion characteristic. Proposed ES PCF structure is able to achieve broadband supercontinuum spectrum with femtosecond laser pulses of very low peak power. This

*A part of the results presented in this chapter has been reported in a research publication:

T. S. Saini, A. Kumar, R. K. Sinha, "Design and Analysis of Equiangular Spiral Photonic Crystal Fiber for Mid-infrared Supercontinuum Generation," *J. Modern Optics,* In Press (2015).

DOI: 10.1080/09500340.2015.1051600

is the first time to our knowledge that a new design of an ES PCF in As_2Se_3 chalcogenide glass is used to generate an ultra-broadband, coherent, and stable supercontinuum spectrum. Ultra broadband SC spectrum spanning 1.2 – 15 µm has been generated using only 8 mm long ES PCF pumped with laser pulses of peak power of 500 W at 3.5 µm.

6.2. Design of Proposed ES PCF Structure

The transverse cross-sectional view of proposed ES PCF has been shown in Fig. 6.1. Eight spiral arms (having five air holes in each) are arranged in As_2Se_3 chalcogenide glass. The diameter of each air hole is taken as d_h. The position of the first air hole of each arm is at a distance r_0 from the centre of PCF structure. The radial and angular position of other air holes in each arm are represented by r_n and θ_n (n =1,2,3,4). θ_n is the angle between the first and $(n+1)^{th}$ air hole in each arm. In general, the n^{th} air hole in each arm is at a distance $r_n = (r_{n-1} + 0.9\ d_h)$. In the simulations the values of r_h and r_0 have been optimized to obtain all-normal dispersion characteristic of the proposed ES PCF structure. The method of analysis is the same as described in Section 5.2 of Chapter 5.

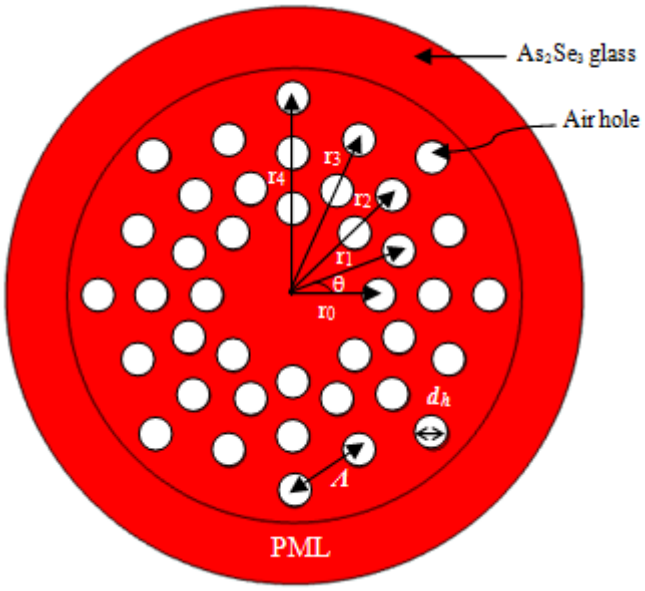

Fig. 6.1: The transverse cross-sectional view of the proposed ES PCF structure.

6.3 Numerical Results and Discussion

In order to acquire efficient ultra-broadband SC in proposed ES PCF, the structural parameters (*i.e.* r_0 and d_h) have been optimized for all-normal and flat-top dispersion profile. For this purpose, initially the effects of various values of r_0 and r_h on dispersion characteristic have been simulated while keeping other parameter fixed. Careful optimization of these parameters provides better control over dispersion profile of proposed ES PCF structure.

The variations of the structural parameters on the dispersion characteristic of the proposed ES PCF have been illustrated in Figs. 6.2 and 6.3. As shown in Fig. 6.2, the dispersion profile of the structure is shifting in the normal dispersion region and becoming flat more and more as the value of r_0 increases. At r_0 = 1.4 µm the structure offers all normal dispersion characteristic with very low dispersion value of approximately -2.9 ps/(nm.km) at 3.5 µm wavelength. Therefore, the wavelength of 3.5 µm has been considered as a pump wavelength in the simulation of supercontinuum spectrum. The variations of dispersion characteristics on r_h are shown in Fig. 6.3. When the value of r_h increases the dispersion curve shifts from normal to anomalous dispersion region.

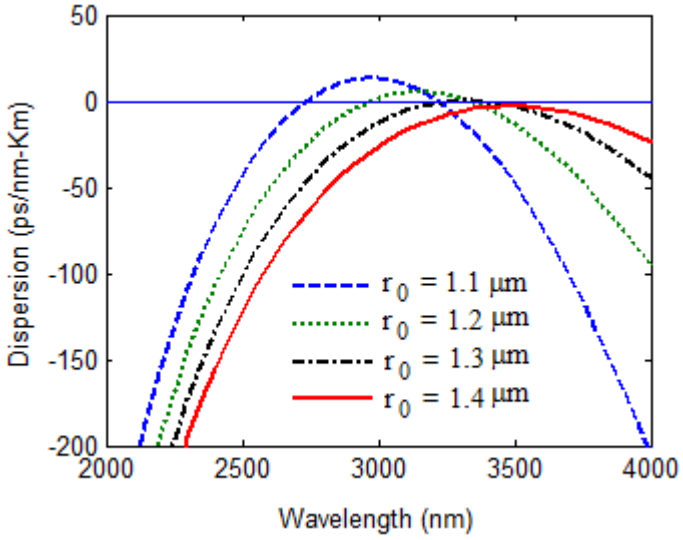

Fig. 6.2: Dispersion characteristics of proposed ES PCF with r_0.

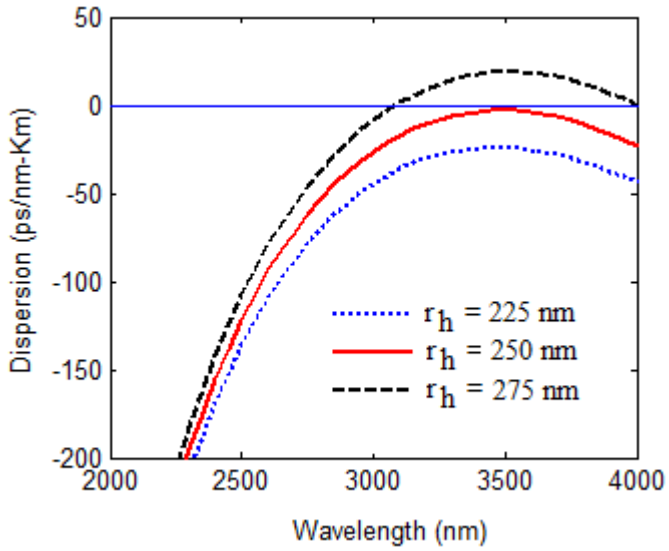

Fig. 6.3: Dispersion characteristics of proposed ES PCF with r_h.

The confinement loss of the structure is also a very important parameter to study the supercontinuum generation. The confinement loss of the proposed ES PCF structure is simulated and shown in Fig.6.4. The proposed structure introduces a confinement loss of ~ 0.17 dB/mm at the pump wavelength.

The effective mode area and nonlinear coefficient of proposed ES PCF structure is shown in Fig. 6.5. The nonlinear coefficient decreases when effective mode area increases. At pump wavelength (*i.e.* 3.5 μm) the proposed structure possesses nonlinearity as high as 12474 W^{-1} km^{-1} with an effective mode area of 3.31 μm^2.

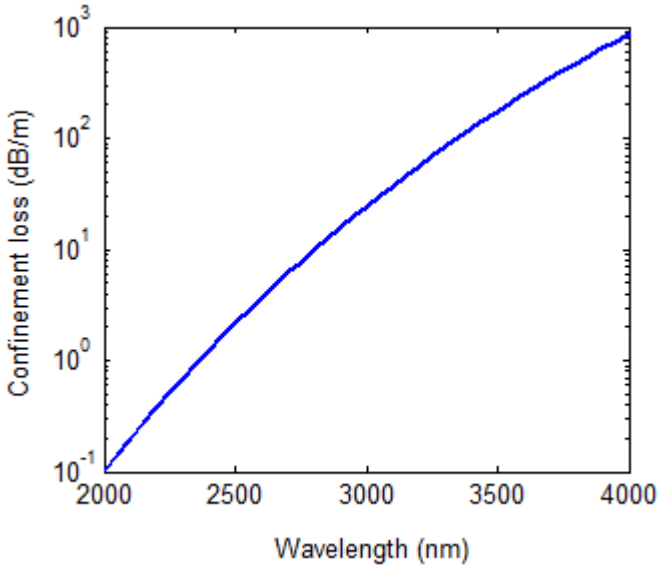

Fig. 6.4: Confinement loss of proposed ES PCF structure

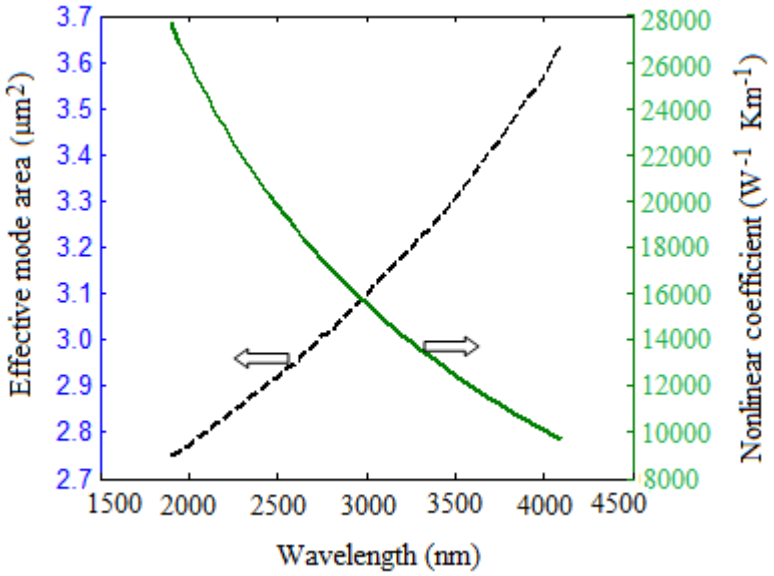

Fig. 6.5: Spectral variation of effective mode area of propagating mode and nonlinear coefficient of proposed ES PCF structure.

Figure 6.6 shows the SC spectra as the pulse propagates through the proposed ES PCF. It has been found that during the initial phase of its propagation, the pulse undergoes a symmetrical spectral broadening under the effect of self-phase modulation (SPM). Within 8 mm fiber length a broadband SC spectrum spanning 1.2 – 15 μm is generated. The primary reason behind the flatness of SC generated for our structure lies in dispersion curve and non-linearity.

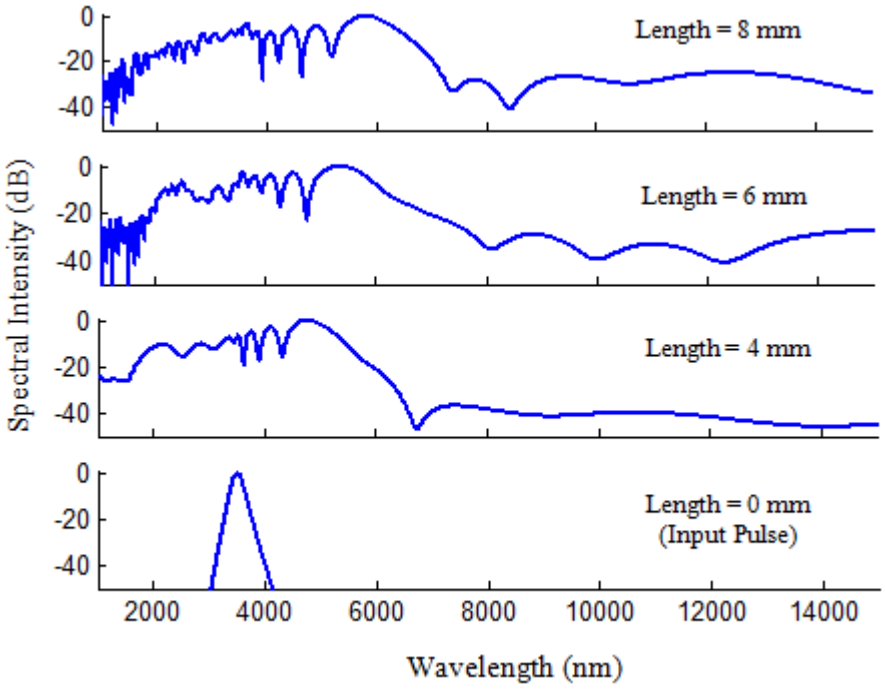

Fig. 6.6: Supercontinuum generation at different lengths of ES PCF pumped at 3.5 μm.

6.4 Conclusions

In this chapter an ES PCF in As_2Se_3 chalcogenide glass is reported for mid-infrared supercontinuum generation. Proposed structure possesses very high nonlinearity (γ = 12474 W^{-1} Km^{-1}) at 3.5 µm with very low and flat dispersion -2.9 ps/(nm.Km). We have generated a broadband supercontinuum spectrum spanning 1.2 – 15 µm in only 8 mm length of proposed ES PCF with very low peak power of laser pulses of 500 W at 3.5 µm. Such ultra-broadband supercontinuum spectrum demonstrates perfect coherence property over the entire bandwidth and is applicable for mid-infrared spectroscopy, gas sensing, early cancer diagnostics and free space communication.

CHAPTER 7

Dispersion Engineered Rib Waveguide for Supercontinuum Generation*

7.1 Introduction

Supercontinuum generation is one of the most fascinating nonlinear effects due to its major impact on spectroscopy, security and molecular sensing [41]. The selection of the pump wavelength acts a very critical role in the process of SCG [127]. In most of the attempts the spectral broadening is achieved using pump pulses of the wavelength near to the zero dispersion wavelength in the anomalous dispersion region. When pump wavelength belong to the anomalous dispersion regime, the spectral broadening is mainly due to the solitons fission or modulation instability (MI). The mechanism of solitons fission is highly sensitive to the laser shot noise [108]. The supercontinuum generation in fiber/waveguide exhibiting all-normal dispersion characteristic is another approach [63]. When we select input wavelength within the normal group velocity dispersion region of waveguide, the process of solitons fission and broadband noise amplification by modulation instability is absent [63]. In normal group velocity dispersion region the FWM process can produce a broadband SC spectrum [41].

Foster et al. showed that an octave spanning supercontinuum can be generated using sub-wavelength dimension optical waveguides with pulses of 250 pJ energy from a femtosecond modelocked Ti:sapphire oscillator [128]. *Yin et al*. numerically reported a design of silicon waveguide for supercontinuum spectrum extending over 400 nm using femtosecond laser pulses of low energy [129]. *Lamont et al*. demonstrated experimentally supercontinuum generation with a -30 dB bandwidth of 750 nm using

*A part of the results presented in this chapter has been submitted to IEEE *J. Sel. Top. Quant. Elecron.* (2015).

610 fs laser pulse with peak power of 68 W [130]. *Zhang et al.* reported two octave supercontinuum spectra spanning 630 nm to 2650 nm using a silicon nitride slot waveguide [54]. *Halir et al.* demonstrated supercontinuum spectrum ranging from 665 nm to 2025 nm using silicon nitride waveguides with pulse energy of 160 pJ [55]. *Karim et al*. proposed numerically a design of $Ge_{11.5}As_{24}Se_{64.5}$ nano-wire for supercontinuum spectrum of 1300 nm bandwidth [131]. *Hu et al*. designed and analysed numerically a tapered rib waveguide (air-SF57 glass-SiO2) for supercontinuum spectrum extending from 1000 nm to 4600 nm [58]. *Safioui et al*. reported more than 550 nm broad supercontinuum spectrum in 1 cm long CMOS compatible hydrogenated amorphous silicon waveguide using picosecond pulses with peak power as low as 4 W [59]. *Karim et al*. designed numerically a dispersion-engineered air clad, $Ge_{11.5}As_{24}Se_{64.5}$ chalcogenide glass channel waveguide for mid-infrared supercontinuum spectrum spanning 1800 nm to 7700 nm using pulse power of 500 W [60].

For mid-infrared supercontinuum spectrum chalcogenide fibers/waveguides are suitable because it has a number of unique properties such as high linear and nonlinear refractive indices, broad infrared transparency, low photon energy and large ultra fast third order optical nonlinearity [132]. The recent progress in chalcogenide photonics has been extensively reviewed in several research articles [132 – 135].

In this chapter, a dispersion engineered channel rib waveguide structure is reported for mid-infrared supercontinuum application. Proposed waveguide structure has been engineered to get all-normal dispersion characteristic. Structure is able to show a very high nonlinearity with lower negative and flat dispersion profile around the pump wavelength. Simulation results indicate that the waveguide structure is capable to realize ultra broadband mid-infrared supercontinuum spectrum using femtosecond laser pulses with relatively lower peak power.

7.2 Proposed Rib Waveguide Structure

A rib waveguide structure in highly nonlinear material (*i.e.* As_2Se_3) for supercontinuum generation in mid-infrared region is reported in this chapter. The transverse cross-sectional view of the proposed rib waveguide geometry is shown in Fig. 7.1(*a*). As shown in this figure, *2a* is the core width, *h* is the core height and *t* represents the slab

width. This is an As_2Se_3 based chalcogenide core deposited on silica substrate. MgF_2 is used as a cladding material. All the geometrical parameters of the waveguides have been tailored for getting all normal dispersion characteristic. Figure 7.1(*b*) illustrates the normalized electric field distribution of propagating mode in the core of the rib waveguide at pump wavelength. In the simulation of proposed rib waveguide structure a constant material loss coefficient of 0.6 cm^{-1} is considered for entire range of supercontinuum spectrum [61]. The Kerr nonlinear coefficient of the material, $\gamma = 2\pi n_2/\lambda A_{eff}$ with nonlinear refractive index, n_2 = 1.5×10^{-17} m^2/W at 2.5 μm for As_2Se_3 glass [116] is taken in the simulation of the structure.

To solve the GNLSE we have used Fourth order Runge-Kutta interaction picture (RK4IP) method. In comparison to other numerical methods this method is most efficient, accurate, and faster integration method. It is closely related to the split-step Fourier method. The procedure of solving GNLSE using the RK4IP is based on transforming the problem into an interaction picture which allows the use of the explicit techniques to progress the solution forward.

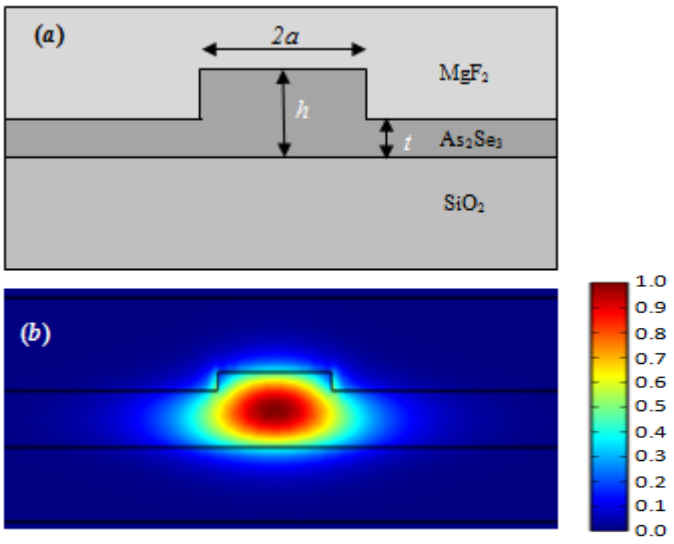

Fig. 7.1. (a) The transverse cross-sectional view of proposed rib waveguide structure; (b) the normalized electric field distribution of propagating mode in the core region at pump wavelength.

7.3 Numerical Results and Discussion

It is well known that waveguide dispersion strongly depends upon the geometry of the waveguide, thus, total dispersion of waveguide can be controlled by tailoring the geometry of waveguide. In order to achieve the suitable waveguide parameters to achieve the all-normal and flat dispersion, which is desirable for supercontinuum generation [63], several simulations have been performed by changing the waveguide geometrical parameters such as '*t*', '*h*' and '2*a*'. The effect of '*t*' on dispersion has been illustrated in Fig. 7.2. From this figure it is clear that the dispersion profile move towards the normal dispersion region on increasing the value of '*t*'. When '*t*' increases the refractive index contrast between the core and cladding region decreases. As a results, the value of dispersion decreases and shifts towards normal dispersion region.

The effect of the core height '*h*' on the chromatic dispersion has been shown in Fig. 7.3. At larger value of core height the dispersion curve starts to shift towards anomalous dispersion region. Increase in '*h*' increases the mode index of fundamental mode and hence tailor the dispersion towards anomalous region. Similarly, increase in core width '*a*' also shifts the dispersion towards anomalous region as shown in Fig. 7.4. Thus, by tailoring the geometrical parameters we can achieve desired dispersion profile.

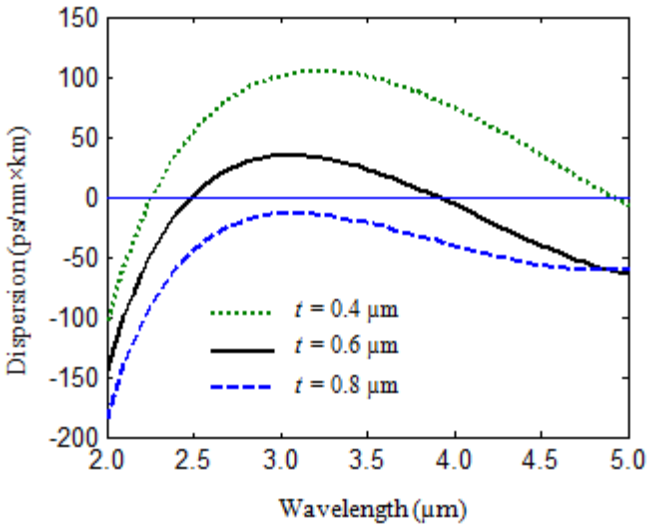

Fig.7.2: The effect of the geometrical parameter 't' on chromatic dispersion profile while keeping other parameters fixed as: a = 1 μm, h = 1 μm.

For optimized geometrical parameters (see Table-7.1) the dispersion characteristic of rib waveguide is exposed in Fig.7.5. All-normal and flat dispersion profile with the dispersion value of about -5 ps/(nm×Km) between the spectral range from 2.925 – 3.2 µm is obtained. The spectral variation of effective-mode-area and corresponding nonlinear coefficient is revealed in Fig.7.6. Simulated results prove that the proposed waveguide structure offers Kerr nonlinear coefficient (γ) as high as 18250 $W^{-1}\,Km^{-1}$ with effective-mode-area (A_{eff}) of 2.07 μm^2 at 2.5 µm.

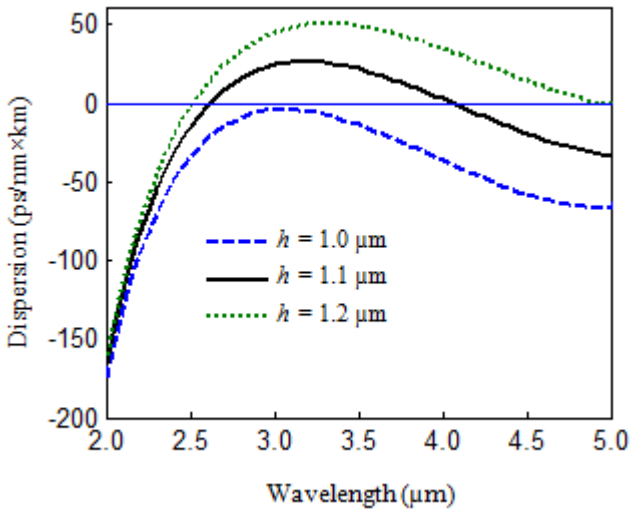

Fig. 7.3: The effect of the core height (i.e. h) on chromatic dispersion profile while keeping other parameters fixed as: a = 1 µm, t = 0.75 µm.

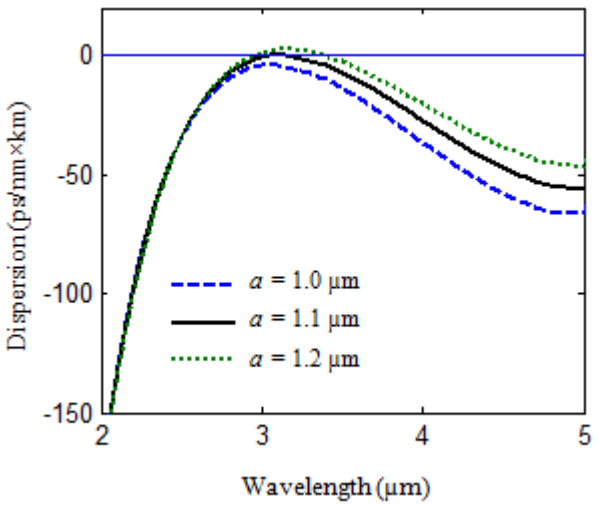

Fig. 7.4. The effect of the core width (i.e. 2a) on chromatic dispersion profile while keeping other parameters fixed as: t = 0.75 µm, h = 1 µm.

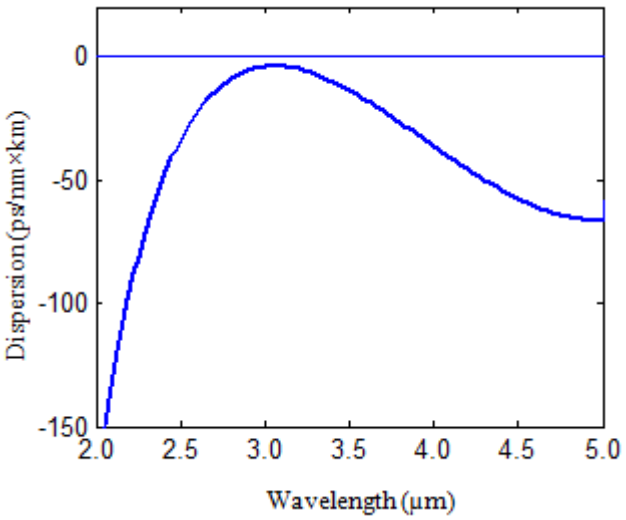

Fig. 7.5: The chromatic dispersion characteristic of proposed rib waveguide structure with optimized parameters (i.e. a = 1.0 μm, t = 0.75 μm, h = 1 μm).

As reported in Fig. 7.7, when we launch the femto-second laser pulses of appropriate pulse parameters (see Table-7.2) a broadband SC spectrum spanning 2 – 15 μm at -30 dB power level is obtained in only 4 mm length of proposed rib waveguide. The calculated values of nonlinear length ($L_{\mathrm{NL}} = 1/\gamma P_0$) and dispersion length ($L_{\mathrm{D}} = \frac{T_0^2}{\beta_2}$; $\tau_0 = T_{\mathrm{FWHM}}/1.763$), for proposed rib waveguide are 4.9×10^{-5} m and 3.89×10^{-2} m respectively for 50 fs laser pulse at 2.5 μm. Within 4 mm length of the rib waveguide an ultra broadband supercontinuum spectrum spanning 2 – 15 μm is generated by launching a 50 fs laser pulses at peak power of 1.1 kW.

The broadening of supercontinuum spectrum also depends on the input pulse width. The influence of the pulse width *i.e.* full width at half maximum (T_{FWHM}) on spectral broadening of supercontinuum spectrum in 4 mm long rib waveguide is revealed in Fig. 7.8. The initial peak power of pulse is fixed at 1.1 kW. As illustrated in Fig.7.8, when the value of pulse width increases the output spectra starts to be narrower. It is clear from this figure that the shorter pulse is better to obtain broader SC spectrum. Tabel-7.2 provides the optimized values of input pulse parameters.

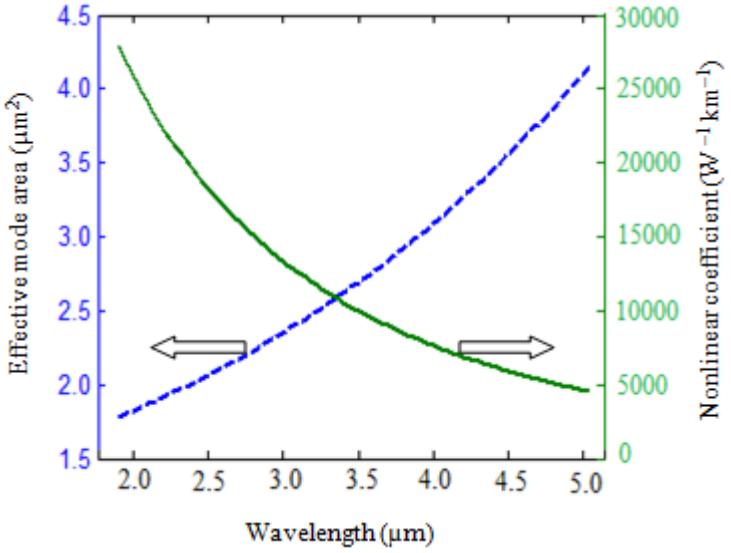

Fig. 7.6: The variation of effective mode area of propagating mode and corresponding nonlinear coefficient of proposed rib waveguide with optimized parameters (i.e. a = 1.0 μm, t = 0.75 μm, h = 1 μm).

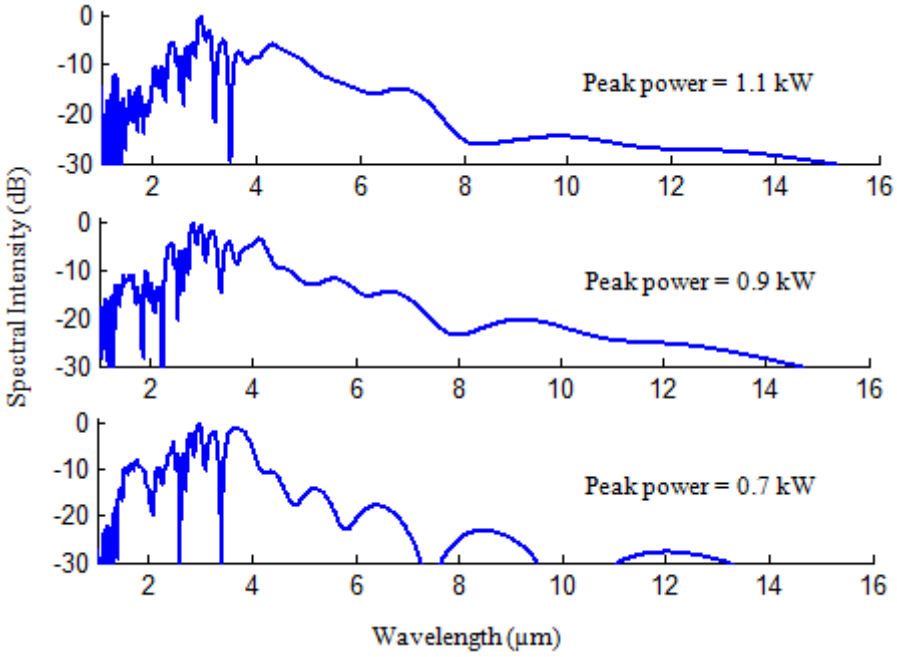

Fig. 7.7: Spectral broadening of supercontinuum spectra from 4 mm long rib waveguide at different peak power; when 50 fs laser pulses at 2.5 μm launched at proposed rib waveguide structure.

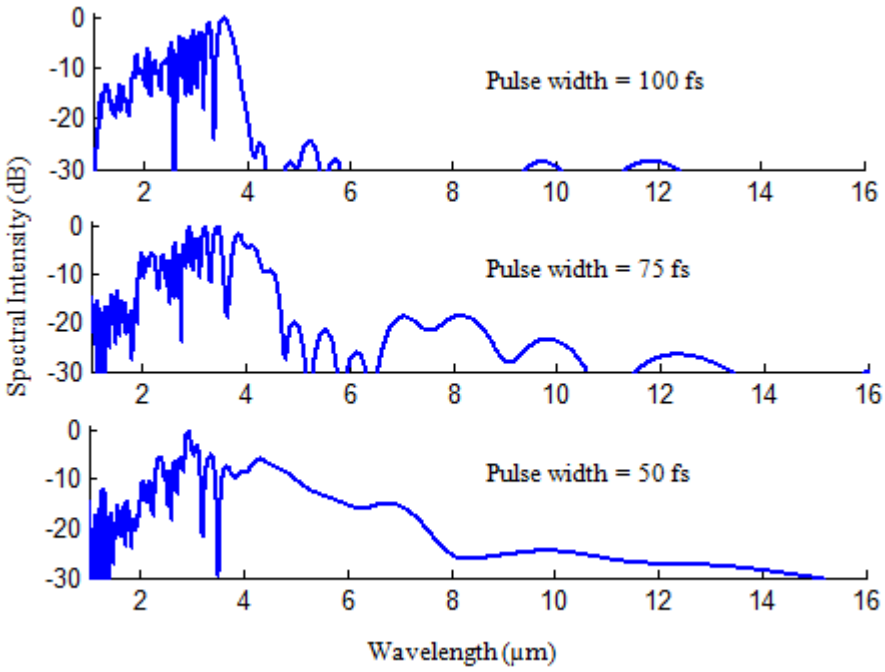

Fig.7.8: Broadening of output spectra from 4 mm long rib waveguide obtained at various values of pulse width (T_{FWHM}) when peak power of incident pulses = 1.1 kW.

7.4. Tolerance Analysis of Rib Waveguide

For fabrication purposes it is very important to investigate the tolerance of the rib waveguide structure with respect to geometrical parameters. We have found that the magnitude of effective mode area, nonlinear coefficient and dispersion are not much sensitive to the structural parameters. For example: at pump wavelength of 2.5 μm 1% variation in 'a' changes effective mode area by 0.6% and change in nonlinear coefficient by 0.4%. These small changes produce only ~1% changes in the spectral width of the supercontinuum spectrum. Proposed rib waveguide structure can be fabricated by photolithography and inductively coupled plasma reactive ion etching technique.

Table 7.1: Geometrical parameters of proposed rib waveguide

Parameter name	*a*	*h*	*T*
Parameter value	1.0 µm	1.0 µm	0.75 µm

Table 7.2: Input pulse parameters for proposed rib waveguide

Parameter name	Peak Power	T_{FWHM}	Pulse shape
Parameter value	1.1 kW	50 fs	hyperbolic secant

7.5 Conclusions

In this chapter a dispersion engineered channel rib waveguide structure is reported for ultra broadband mid-infrared supercontinuum spectrum spanning 2 – 15 µm at -30 dB power level. Such broadband spectral range of supercontinuum spectrum is achieved using only 4 mm long channel rib waveguide when 50 fs laser pulses of 1.1 kW peak power at 2.5 µm are incident on it. Simulated outcomes revealed that the proposed rib waveguide structure offers nonlinear coefficient as large as 18250 W^{-1} Km^{-1} at pump wavelength of 2.5 µm with the effective-mode-area of 2.07 μm^2. This waveguide structure can be a good candidate for generating efficient supercontinuum which is applicable for various nonlinear applications such as frequency comb generation, gas sensing, food quality control and early cancer diagnostics.

CHAPTER 8

Tunable Slow Light Generation in Specialty Optical Fibers*

8.1 Introduction

Slow light is the topic of rapidly increasing interest in the past decade because of its many applications such as optical buffering, data synchronization, optical memories, optical signal processing, microwave photonics, and precise interferometric instruments [136 – 139]. Slow-light means the possibility of controlling and reducing the group velocity of optical signal. The technique based on slow-light provides the hopeful solutions of the broadband and tunable time-delay for microwave and milli-meter wave systems. By controlling and storing the light and enhancing nonlinearity, it is possible to design on-chip all-optical signal processing photonic crystal devices. When one allows light to interact with an optically resonant media, it is possible to control the speed of light and its other propagation characteristics [140]. Slow-light can be obtained by the various methods including SBS and SRS in standard single mode fiber [141 – 146], electromagnetically induced transparency, Raman-assisted optical parametric amplification [147], coherent population oscillation [148] and slow-light relying on dispersive medium [149]. The main advantage of the SBS over other methods is the possibility of controlling the pulse delay all optically only by tuning the pump power [146]. SBS in optical fiber is much more gorgeous because it leads to the

*Parts of the results presented in this chapter have been reported in the research publications:

1. T. S. Saini, A. Kumar, R. K. Sinha, "Analysis and Design of Single-Mode As_2Se_3-Chalcogenide Photonic Crystal Fiber for Generation of Slow Light with Tunable Features," IEEE *J. Sel. Top. Quant. Electron*. In press (2015);
2. T. S. Saini, A. Kumar, R. K. Sinha, "Slow light generation in single mode tellurite fibers," *J. Modern Optics* 62(7), 508 – 513 (2015).

application of slow-light in telecommunication systems with moderate pump power and operation at room temperature.

The slow-light can be used for various applications in optical communication systems, optical storage, buffering, and signal processing. Various kinds of fibers have been reported for generating slow-light. *Schneider et al*. employed a step index optical fiber in silica material for generation of millimeter waves [150]. To acquire effective time-delay and Brillouin gain in silica based optical fibers, we need the fiber length of the order of kilometer. For this purpose, lot of work have been performed to shrink the length of the fiber by choosing higher refractive index media [151 – 156] and designing photonic crystal fibers [157, 158] to achieve desired time-delay and Brillouin gain. The shape and strength of Brillouin gain depends on overlap between the optical and acoustic modes. More effective control over acousto-optic interaction can be achieved in photonic crystal fiber geometries.

Small-core PCF is an excellent medium to slow down the light with a moderate pump. Large-delay slow light based on stimulated Brillouin scattering in a short length of small-core pure silica photonic crystal fiber has been realized by *Yang et al*. [157]. SBS of visible light in silica based small-core photonic crystal fiber pumped with 532 nm has been characterized by *Woodward et al*. [158]. *Corcoran et al*. demonstrated the emission of green light in silicon photonic crystal waveguides using slow light enhanced third harmonic generation [159]. *Heidari et al*. presented dispersion engineering of slow-light photonic crystal waveguide based on the selective microfluidic infiltration technique [160]. *Monat et al*. presented a review on various nonlinear phenomenon enhanced by slow light in silicon based photonic crystal waveguides [161]. *Pant et al*. reported first time the maximum delay of ~23 ns in 7 cm long chalcogenide rib waveguide [162] Numerical modeling of SBS in standard silica fibers for slow-light applications have been made earlier in different research and review articles [163 – 165]. However, there is a need to investigate features of tunable slow-light in higher refractive index based PCFs. Because of its larger refractive index contrast, PCFs can have tighter confinement of both light and the sound and hence enhance acousto-optic interactions. Since chalcogenide glasses have the high third-order nonlinearity, therefore it can be used as a functional optical fiber.

In this chapter, the theoretical investigation of stimulated Brillouin scattering-based tunable slow light in three different designs of (i) Er-doped tellurite fiber, (ii) undoped tellurite fiber, and (iii) photonic crystal fibers is provided. Simulated results indicate that the time delay experienced by pulse in fiber structure can be tuned with pump power and thereby tunable slow light features can be obtained.

8.2 Principle of Slow Light Based on SBS

When highly intense pump wave interact with the counter propagating, weak signal wave, then a slowly travelling wave is generated. This creates travelling density variations (*i.e.* acoustic wave) in the medium. Consequently, as illustrated in Fig. 8.1, acoustic wave leads to a travelling grating of refractive index variation in the medium. When phase matching condition is satisfied, the travelling refractive index grating can couple optical power in between pump and signal waves.

Let, ω_p and ω_s are the frequencies of pump and counter propagating signal wave of intensities I_p and I_s respectively.

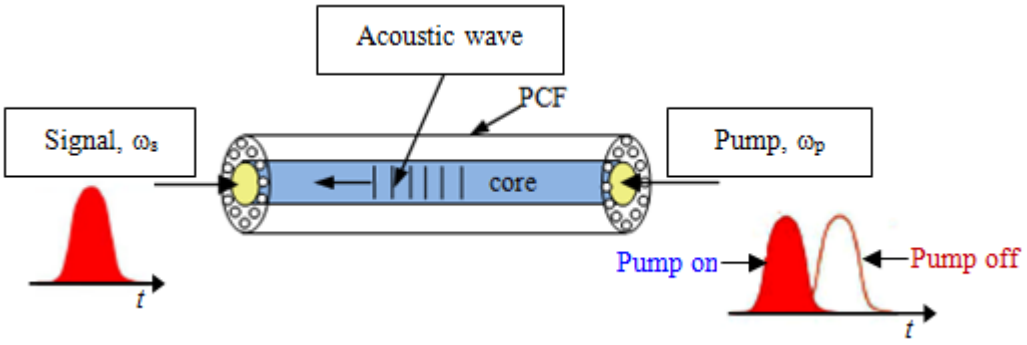

Fig. 8.1: Schematic of the principle of stimulated Brillouin scattering in PCF.

The coupled non linear differential equations for pump and signal waves is specified by the following equations [41]

$$\frac{dI_p}{dz} = -g_B I_p I_s - \alpha_p I_p \qquad (8.1)$$

$$-\frac{dI_s}{dz} = +g_B I_p I_s - \alpha_s I_s \qquad (8.2)$$

by assuming the pump wave as undepleted, and $(\alpha_p \approx \alpha_s) = \alpha$, the result of the Eqs. 8.1 & 8.2 is specified by the relation

$$I_s(0) = I_s(L)\exp\left[(g_B P_0 L_{eff}/A_{eff} - \alpha L\right] \quad (8.3)$$

with, $L_{eff} = \alpha^{-1}(1 - \exp(-\alpha L_{eff}))$ (8.4)

where, L is the real length and L_{eff} is the effective length of the fiber, α is the attenuation constant for the fiber.

The Brillouin gain can be expressed as

$$g_B(\Omega) = \frac{g_p(\Gamma_B/2)^2}{(\Omega - \Omega_B)^2 + (\Gamma_B/2)^2} \quad (8.5)$$

where g_p is the peak value of the Brillouin gain at $\Omega = \Omega_B$ and given by the relation

$$g_p \equiv g_B(\Omega_B) = \frac{2\pi^2 n^7 p_{12}^2}{c\lambda_p^2 \rho_0 v_A \Gamma_B} \quad (8.6)$$

here ρ_0 is the density, and p_{12} is the longitudinal elasto-optic coefficient. The full width at half maximum (FWHM) of the gain spectrum is related to Γ_B by the relation $\Delta\nu_B = \Gamma_B/(2\pi)$.

The nonlinear coefficient (γ) offered by PCF, related to the nonlinear refractive index of material of PCF and the effective area of propagating mode as

$$\gamma = \frac{2\pi n_2}{\lambda A_{eff}} \quad (8.7)$$

where, n_2 is the nonlinear coefficient of material of PCF and A_{eff} is the effective mode area of propagating mode.

The Brillouin gain coefficient of PCF can be calculated using the relation [155]

$$G = 10\log\left[\exp\left(\frac{g_B K P_0 L_{eff}}{A_{eff}} - \alpha L\right)\right] \quad (8.8)$$

where, P_0 is the pump power and K is the polarization factor and depends on the polarization properties of the fiber. The value of polarization factor is 1 if the polarization is maintained and it is 0.5 if polarization is not maintained. Although, some results [153, 154, and 166] showed that K = 0.667 is more appropriate, for the fiber which is low-birefringence and very high polarization beat length. In our simulation K = 0.667 has been used.

The maximum allowable pump power, $P_{\max}$ (the maximum pump power above which the output pulse get distorted), related to the Brillouin gain coefficient g_B as [153, 167]

$$P_{\max} = 21 \frac{A_{\text{eff}}}{K\, g_{\text{B}}\, L_{\text{eff}}} \qquad (8.9)$$

Once pump power approached to $P_{\max}$ then the backscattered wave can be generated from the background noise in the fiber, which leads to serious output pulse distortion. Therefore the value of pump power must be smaller than the $P_{\max}$.

The SBS-induced time delay per unit length and per unit pump power by slow light fiber devices can be expressed as [153, 155]

$$\frac{\Delta t_{\text{d}}}{P_{\text{p}} L_{\text{eff}}} = \frac{g_{\text{B}}\, K}{A_{\text{eff}} \Gamma_{\text{B}}} \qquad (8.10)$$

8.3 Slow Light Generation in Er- Doped Tellurite Fiber

The pump and signal waves propagation are simulated over a 2 meter long *E*r- doped tellurite fiber, which are based on the same parameter values used in Ref. [154]. Specifically, the pump power, P_{p} = 360 mW at 1542 nm, the Brillouin gain coefficient, g_B = 1.47×10^{-10} m/W, Brillouin shift, Ω_B= 7.882 GHz, the mode effective area, A_{eff} = 9.18 μm^2, the fibre loss = 0.51 dB/m ($i.e.\alpha$ = 0.117 m^{-1}) and the polarization factor, K = 0.667.

8.3.1 Results and discussion

Using above mentioned parameters the Brillouin gain of the fiber against the frequency difference between pump and signal $(\omega_p - \omega_s)$ in 2 meter long *E*r-doped tellurite fiber has been illustrated in Fig. 8.2. It can be clearly seen that the peak gain of ~ 29 dB is obtained in this fiber at frequency shift of 7.882 GHz.

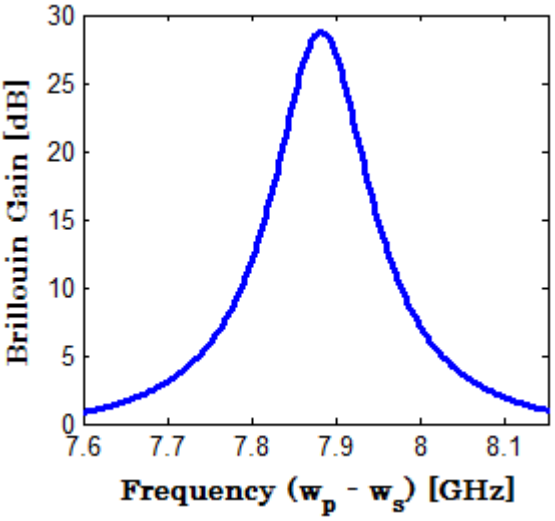

Fig. 8.2: Brillouin gain of the fiber with frequency difference between pump and signal $(\omega_p - \omega_s)$ in two meter Er-doped tellurite fiber.

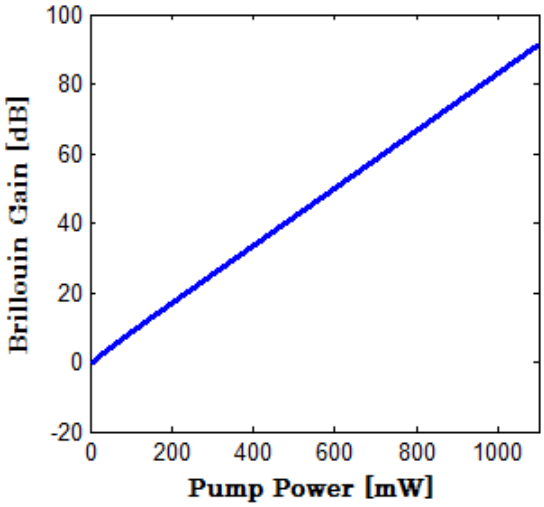

Fig. 8.3: Effect of pump power on Brillouin gain.

Figure 8.3 shows the effect of pump power on Brillouin gain. It is clear from this figure that the Brillouin gain linearly increases with pump power. Our simulation result shows that for pump power of 360 mW, the value of Brillouin gain is 29.72 dB, which correspond to 0.0825 dB/mW of the pump power. It is very close to the experimentally measured value [154], which validates that the formulae for Brillouin gain and MATLAB codes developed for its calculation are correct. Maximum 57.8 dB unsaturated gain has been achieved at pump power of 700 mW. The maximum pump power up to which the output pulse does not get affected by the distortion is about 1100 mW which is obtained from Eq. (8.9). Pump power above 1100 mW leads to serious output pulse distortion. The maximum Brillouin gain which can be achieved at 1100 mW is about 91 dB for 2 meter long fiber.

Figure 8.4 illustrates the dependence of the SBS-induced time delay per unit pump power on the real length of the fiber. For 2 meter length of fiber, 127 ps/mW time delay has been obtained. Therefore, pump power with 360 mW introduces total time delay of 45.72 ns in 2 meter length of *E*r-doped fiber.

Finally, the time delay in pulse with the pump power has been illustrated in Fig. 8.5. The maximum time delay using 2 meter of *E*r-doped fiber has been obtained upto 140 ns at 1100 mW pump power.

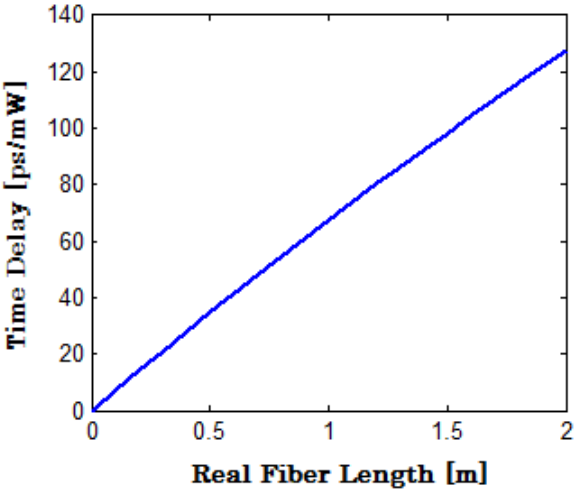

Fig. 8.4: Time delay as a function of real fiber length.

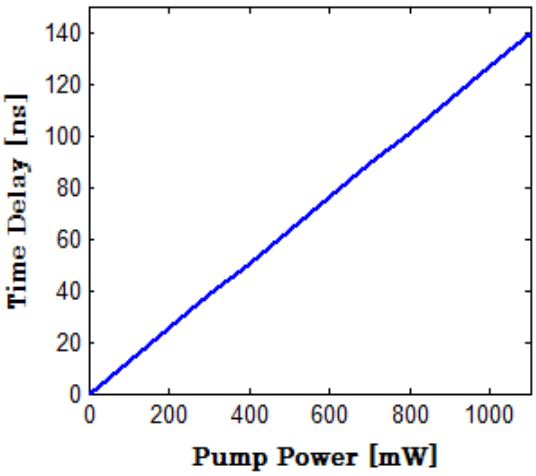

Fig. 8.5: Time delay as a function of pump power.

8.4 Slow Light Generation in Undoped Tellurite Fiber

Another fiber in the study is an undoped tellurite fiber with the following parameters as in Ref. [155]. Specifically, the pump power, P_p = 10 mW at 1550 nm, length of the fiber = 100 m, the Brillouin gain coefficient, g_B=1.6989×10^{-10} m/W, Brillouin shift, Ω_B= 7.972 GHz, the mode effective area, A_{eff} = 6.9697 μm^2, the fibre loss=0.0558 dB/m and the polarization factor, K = 0.667.

8.4.1 Results and discussion

The Brillouin gain of the fiber against the frequency change between pump and signal ($\omega_p - \omega_s$) in undoped tellurite fiber has been illustrated in Fig. 8.6. The maximum value of Brillouin gain of 34.2 dB has been obtained at 7.972 GHz frequency shift with pump power of 10 mW, which is well matched with the experimental result [155].

Brillouin gain of the fiber linearly increases with pump power which is shown in Fig. 8.7. Simulation results show that for pump power of 23 mW, the value of Brillouin gain is ~86 dB, which correspond to 3.73 dB/mW of the pump power. The maximum pump power for which output pulse does not affected by the distortion is 23.5 mW. Based on the simulated results for doped and undoped tellurite fibers, one can conclude that the maximum allowable pump power is larger for E_r-doped tellurite fiber in comparison to that of for undoped tellurite fiber. Therefore, for obtaining same time delay we required short length of E_r-doped tellurite fiber in comparison to undoped tellurite fiber.

The dependence of the SBS-induced time delay per unit pump power on the real length of the fiber has been shown in Fig. 8.8. The time delay per unit power obtained by 100 meters fiber is about 9.88 ns/mW. Therefore, pump power with 10 mW introduces total time delay of ~ 99 ns in 100 meter length of undoped tellurite fiber. As shown in Fig.8. 8, the maximum value of time delay per mW power for 1000 meter long fiber is 26.5 ns/mW. The total time delay with the pump power has been illustrated in Fig. 8.9. The maximum time delay using 100 meter undoped tellurite fiber has been obtained up to 227 ns at 23 mW pump power.

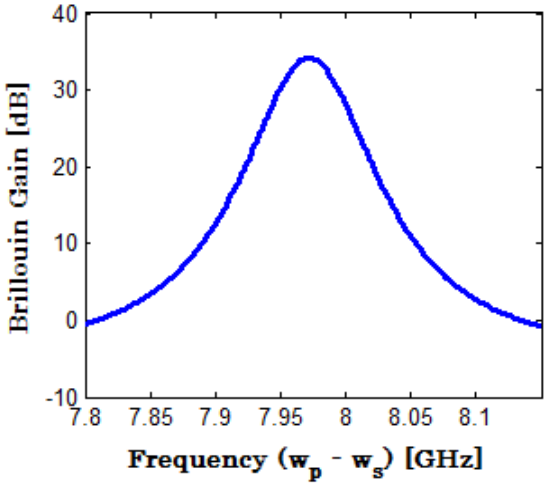

Fig. 8.6: Brillouin gain of the fiber against the frequency difference between pump and signal ($\omega_p - \omega_s$) in 100 meter long undoped tellurite fiber with 10 mW pump power.

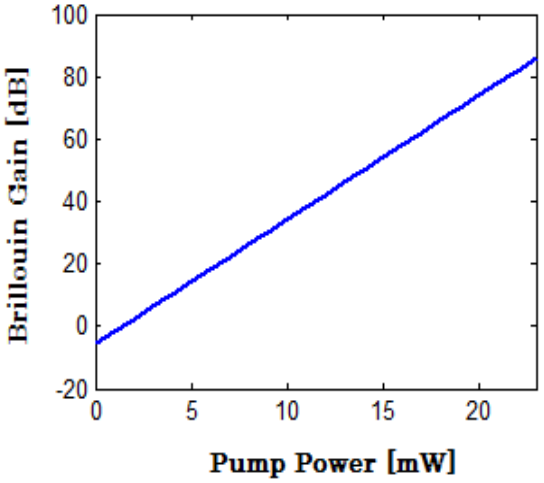

Fig. 8.7: Brillouin gain as a function of pump power.

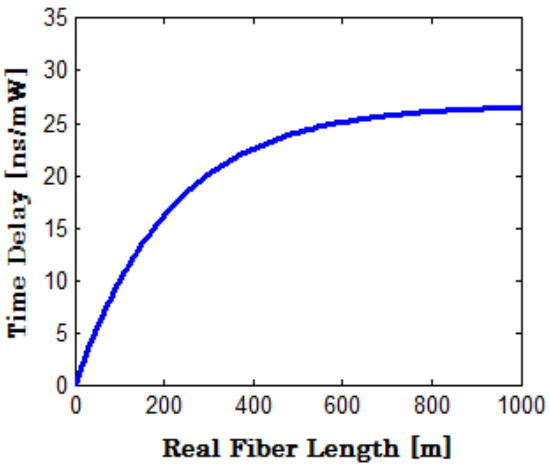

Fig. 8.8: Time delay per unit power with real fiber length.

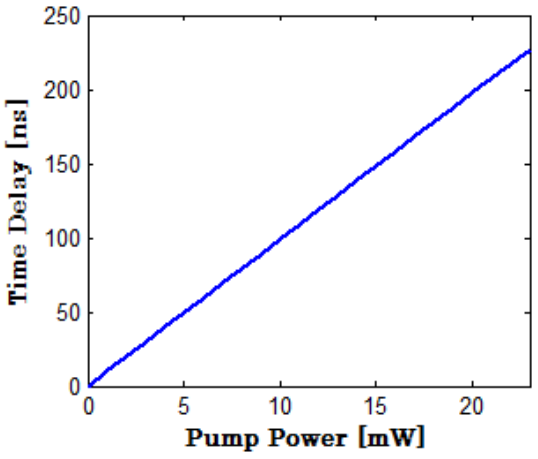

Fig. 8.9: Total time delay with pump power.

8.5 Slow Light Generation in Single Mode PCF

To study the slow light generation in PCF based on stimulated Brillouin scattering, first we have proposed a single-mode PCF design. The transverse cross-sectional view of the proposed PCF structure has been illustrated in Fig. 8.10. It consists of an array of air holes arranged in triangular lattice pattern in As_2Se_3-based chalcogenide glass. The diameter of all air holes is considered identical and represented by '*d*' while the centre to centre distance of the air holes (*i.e.* pitch) is taken as '*Λ*'. In the simulation, the pitch of the PCF has been kept fixed at 1μm. To change the effective mode area of PCF the diameter of air holes can be changed. The refractive index of As_2Se_3 based chalcogenide glass has been taken equal to 2.886 at 1.06 μm. The inherent material properties of As_2Se_3 based chalcogenide material have been taken from Ref. [168]. From the manufacturing point of view our proposed structure can be fabricated by standard extrusion and stacking based methods, commonly used for fabrication of PCFs.

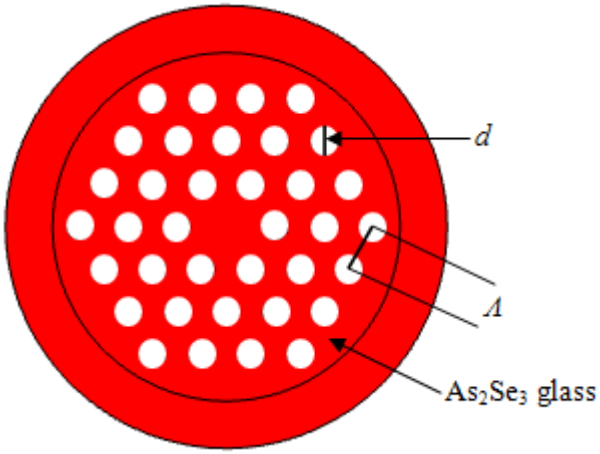

Fig. 8.10: Transverse cross-sectional view of the proposed highly nonlinear photonic crystal fiber structure.

8.5.1 Condition for single mode operation

In order to study the slow light in PCF it is important for PCF to be single-mode at the wavelength of interest. In multimode PCF, the fundamental mode will couple to higher-order modes that have a larger effective area and lower nonlinearity. This results in reduction of nonlinear interaction which is needed for SBS effect. The *V* parameter of a PCF can be simply written as [169]

$$V(\nu) = k\Lambda \sqrt{\left(n_{\text{eff,c}}^2(\nu) - n_{\text{eff,cl}}^2(\nu)\right)} \qquad (8.11)$$

where $n_{\text{eff,c}}(\nu)$ is the effective index of fundamental mode confined in the core, and $n_{\text{eff,cl}}(\nu)$ is the effective index of mode which distributes over the cladding with a periodic array of air holes. For PCF geometry, the single mode condition is found to be $V(\nu) < \pi$ [169].

The numerical result of single mode parameter '*V*' for proposed PCF with various *d/Λ* at fixed wavelength of 1.06 µm is shown in Fig. 8.11. It is clear from this figure that when *d/Λ* = 0.5 the value of *V* parameter become 3.17, which exceeds the limit of single mode operation (*i.e*. 3.14). Therefore the value of *d/Λ* must be less than 0.5 to ensure single mode condition in proposed PCF.

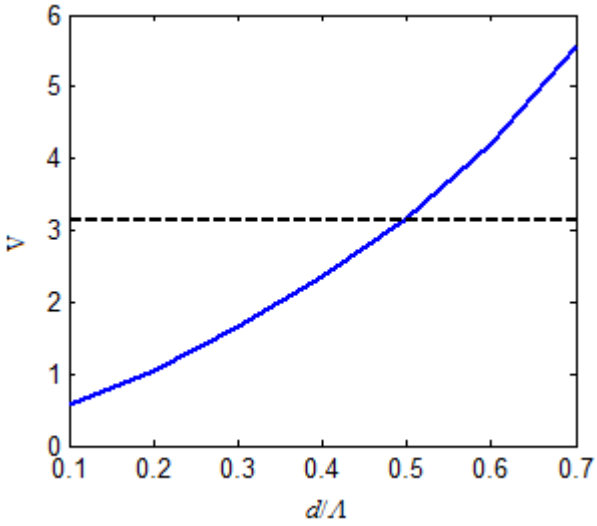

Fig. 8.11: Variation of 'V' parameter of the proposed PCF with d/Λ.

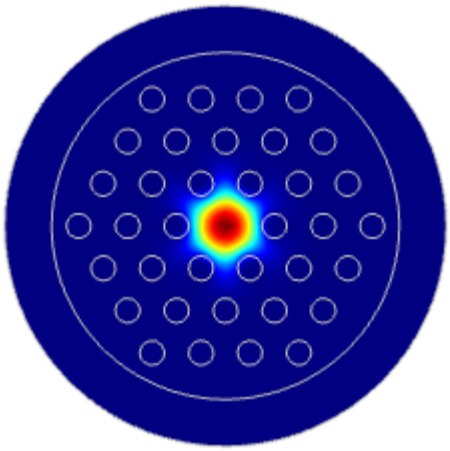

Fig. 8.12: Electric field distribution of fundamental mode with d/Λ = 0.4 at 1.06 µm wavelength.

8.5.2 Results and discussion

As discussed in the previous Section 8.5.1, in order to ensure single-mode operation in proposed PCF, the value of *d/Λ* must be less than 0.5. Therefore, we have chosen *d/Λ* = 0.4 in all the simulations. Figure 8.12 illustrates the electric field distribution of fundamental mode with *d/Λ* = 0.4 at 1.06 um wavelength. The effective mode area plays very important role to enhance nonlinear effects in PCFs. In this work the effective mode area of PCF has been controlled by tuning the air filling fraction (which is defined as the ratio of the diameter of air holes to the pitch of the air holes) of the PCF. The influence of air filling fraction (*i.e. d/Λ*) on the effective mode area of

propagating mode in PCF has been illustrated in Fig. 8.13. The effective mode area decreases on increasing *d/Λ,* because of reduction in the core size on increasing *d/Λ*. Since the nonlinearity is inversely proportion to the effective mode area, the nonlinear coefficient increases on increasing *d/Λ*. Simulated results show that the proposed structure offers nonlinear coefficient as high as 92 W^{-1} m^{-1} with effective mode area of 1.53 um^2 at $d/\Lambda = 0.4$.

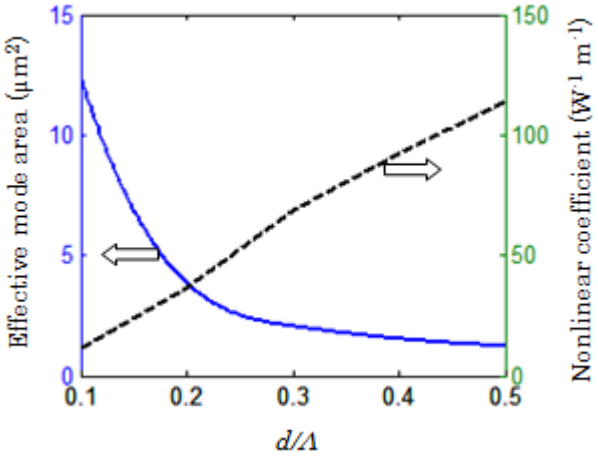

Fig. 8.13: Influence of the effective mode area and nonlinear coefficient with d/Λ.

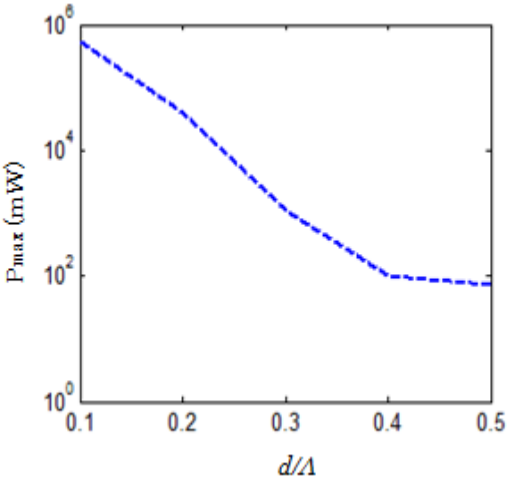

Fig. 8.14: Maximum allowable pump power as a function of d/Λ.

When the value of air filling fraction (AFF) increases, the core area decreases, this restricts on maximum allowable pump power (P_{max}) for undistorted output pulse from the PCF. As shown in Fig. 8.14, the maximum allowable pump power decreases on increasing *d/Λ* value ranging from 0.1 to 0.5 (see Table-8.1). When, AFF or *d/Λ* value of proposed PCF structure increases the effective mode area of propagating mode decreases. Therefore, due to the confinement of field within the smaller region the power handling capability of photonic crystal fiber decreases and hence the maximum allowable pump power decreases. The value of P_{max} is 100.6 mW when $d/\Lambda = 0.4$.

The confinement loss is also a very important feature of photonic crystal fibers. As illustrated in Fig. 8.15 the confinement loss of PCF is very large at $d/\Lambda = 0.1$ and it decreases with *d/Λ*. The reason of decreasing confinement loss on increasing *d/Λ* ratio is that the field becomes more and more confined within the small core of PCF when *d/Λ* increases. This is due to the fact that on increasing hole diameter *d*, the difference between core-cladding refractive index increases leading to higher confinement of light in the core region.

The influence of air filling fraction on Brillouin gain for one meter length of PCF has been illustrated in Fig. 8.16. The Brillouin gain increases on increasing the value of d/Λ. When, air filling fraction increases the effective area of propagating mode decreases.

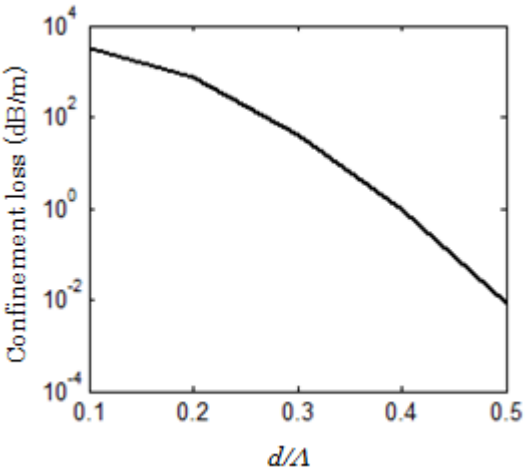

Fig. 8.15: Confinement loss of the proposed PCF structure as a function of d/Λ.

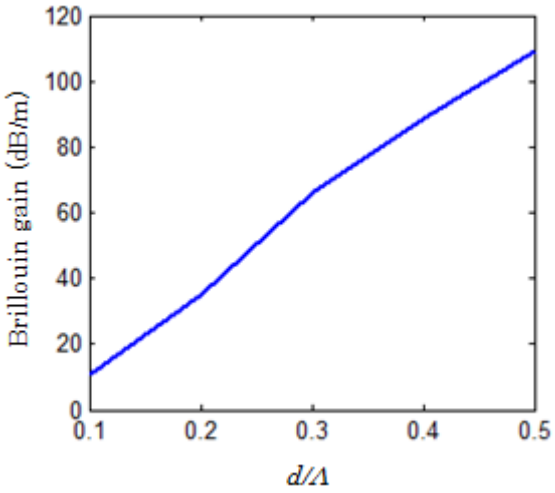

Fig. 8.16: Influence of d/Λ on Brillouin gain in proposed PCF structure with 100 mWpump power.

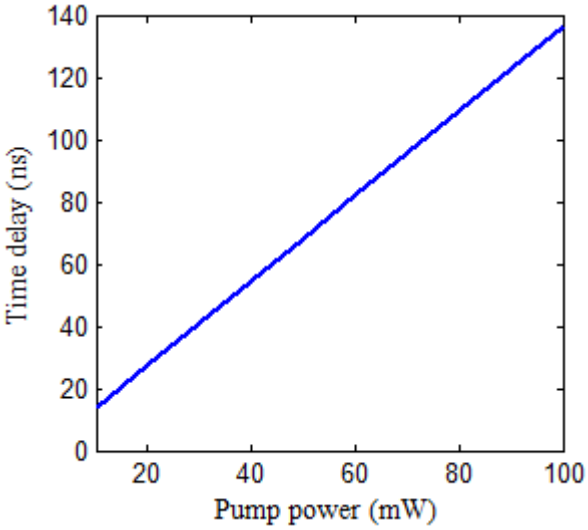

Fig. 8.17: Influence on time delay per unit length with incident pump power.

Therefore, on increasing the value of d/Λ, the light beam is confined within the smaller core. This results in great enhancement in Brillouin scattering and consequently increases the Brillouin gain. At air filling fraction equal to 0.1 the value of Brillouin

gain is 10.8 dB/m and it increases on increasing the value of air filling fraction. Brillouin gain increases upto ~ 88.6 dB/m when air filling fraction reaches at 0.4. However, at such high value of Brillouin gain, even a -50 dB return loss from an angle-polished connector will make the fiber into a Brillouin laser. Therefore, the d/Λ should be suitably selected to avoid return loss at the connecters.

The influence of the pump power on time delay for unit length of PCF with d/Λ = 0.4 has been illustrated in Fig. 8.17. The results obtained at various pump powers are tabulated in Table 8.2. Time delay in output pulse increases linearly with increasing pump power. It is due to the fact that for higher optical powers, there is a stimulated effect, where the optical fields substantially contribute to the phonon population. The time delay can be tuned between ~14 ns to ~137 ns at pump power of 10 mW to 100 mW respectively using one meter long PCF having d/Λ equal to 0.4. Therefore, desired time delay can be obtained by tuning the pump power for a given PCF.

Table. 8.1: Maximum allowable pump power (P_{max}).

d/Λ	0.1	0.2	0.3	0.4	0.5
P_{max} (mW)	540143	39434	1132	100.6	73

Table. 8.2: Time delay in 1 meter long proposed PCF.

Pump power (mW)	20	40	60	80	100
Max. time delay (ns)	27.4	54.9	82.4	109.9	137.4

8.6 Conclusions

In this chapter, three different types of specialty optical fibers have been analysed for tunable slow light generation based on stimulated Brillouin scattering. Simulated results indicate that (*i*) Brillouin gain up to ~91 dB and maximum time delay of 140 ns can be achieved using 2 meter long *E*r-doped tellurite fiber with maximum allowable pump power of 1100 mW, (*ii*) Brillouin gain up to ~86 dB and maximum time delay of 227 ns can be achieved from 100 meter undoped tellurite fiber with 23 mW pump power, *(iii)* Brillouin gain upto ~88 dB/m and maximum time delay upto ~137 ns have been

achieved using 1 meter long photonic crystal fiber pumped with 100 mW. In addition to geometrical parameters of fibers, the time delay can also be tuned with the pump power and thereby tunable slow light features can be obtained. The designed chalcogenide photonic crystal fiber is expected to have potential applications in realization of compact slow light devices.

CHAPTER 9

Concluding Remarks and Scope for Future Work

Concluding remarks and the scope for the future work coming up from the current thesis work has been presented in this chapter. In this thesis we have presented some novel designs in PCF and rectangular waveguide geometries for three different applications (*i.e*., for high power delivery devices, supercontinuum generation and slow light generation). For high power delivery applications the designs show effective SM operation with large-core size by higher-order mode discrimination. In particular we have presented asymmetric air holes arranged in the cladding region of the PCFs and multi-trench leaky cladding design for rectangular channel waveguide. With asymmetric LMA PCF the effective SM operation can be ensured with the effective mode area as large as 1530 μm^2 at 30 cm bend state. Proposed LMA TC PCF geometry-I offers the effective mode area as large as 875 μm^2 with bend radius of 20 cm. In spite of such large effective mode area the proposed TC PCF structure offers very low bend loss for LP_{01} mode (*i.e.* 0.038 dB/m) while very large bend loss for LP_{11} mode (*i.e.* 6.94 dB/m). The proposed LMA TC PCF geometry-II is able to maintain effective mode area as large as ~800 μm^2 with bend radius of 15 cm. With multi-trench leaky cladding design in the channel waveguide structure the core size for the SM operation can be increased to 2.25 times as compared to conventional SM waveguide. The proposed waveguide design shows effective SM operation with core area as large as 100 μm^2. LMA waveguide design offers extended SM operation in the wavelength range of 1.25 – 2.0 μm. Such large core size PCF and waveguide designs are able to eliminate all unwanted nonlinear effects. LMA designs reported in this thesis should be useful for high power delivery devices such as high power fiber lasers and amplifiers.

For supercontinuum and slow light applications the PCF and waveguide designs presented in this thesis have been optimized for low effective mode area to obtained high nonlinearity. To obtain smooth broadening of supercontinuum spectrum, designs have been optimized for all-normal dispersion profile. Proposed TC PCF structure is able to offer ultra-broadband SC spectrum spanning 1.9 – 10 μm at the -30 dB level using only 6 mm long PCF pumped with 50 fs laser pulses of relatively low peak power at 4.5 μm. Proposed TCGI PCF design in As_2Se_3 based chalcogenide glass is able to extend the supercontinuum spectrum spanning 2 – 15 μm using 50 fs laser pulses of 3.5 kW peak power at 4.1 μm. Such ultra broadband white light supercontinuum spectrum is also achieved using rib waveguide and equiangular spiral PCF geometries. Slow light with tunable features is investigated in doped and undoped tellurite fibers and As_2Se_3 based chalcogenide PCF geometries for telecommunication and computing applications. To obtain same time delay we required short length of E_r-doped tellurite fiber in comparison to undoped tellurite fiber. Time delay can be tuned with pump power and fiber length. In PCF geometry the maximum time delay up to 137 ns can be obtained using 1 meter long PCF pumped with 100 mW.

The research work reported in the thesis has identified several areas of research for the future investigation.

To access the actual device performance, the LMA PCF and waveguide designs presented in Chapter 2 & 3 of this thesis can be extended to active materials. The effect of temperature on the modal analysis of the proposed designs can also be studied. The bend insensitive PCF structure can be implemented in the proposed triangular core LMA PCF. Proposed TCGI PCF structure reported in Chapter 5 can be used to obtained supercontinuum generation in visible and deep ultraviolet region taking ZBLAN or tellurite as a PCF material. The spectral coherence of the supercontinuum spectra generated through triangular core PCFs and rib waveguide geometries is also a matter of further study.

References

[1] T. H. Maiman, "Stimulated optical radiation in ruby," Nature 187, 493-494 (1960).

[2] A. Javan, W. R. Bennett, Jr., and D. R. Herriott, "Population inversion and continuous optical maser oscillation in a gas discharge containing a He-Ne mixture," Phys. Rev. Lett., 6, 106-110 (1961).

[3] C. K. N. Patel, "Continuous-wave laser action on vibrational-rotational transitions of CO_2," Phys. Rev., 136, A1187-A1193, (1964).

[4] W. B. Bridges, A. N. Chester, A. S. Halsted and J. V. Parker, "Ion laser plasmas," *Proc*. IEEE 59, 724-737, (1971).

[5] A. Giesen and J. Speiser, "Fifteen years of work on thin-disk lasers: results and scaling laws," IEEE J Sel. Top Quantum Electron. 13, 598-609 (2007).

[6] P. Russbueldt, T. Mans, J. Weitenberg, H. D. Hoffmann and R. Poprawe, "Compact diode-pumped 1.1 kW Yb:Yag Innoslab femtosecond amplifier," Opt. Lett. 35, 4169-4171 (2010).

[7] D. J. Richardson, J. Nillson and W. A. Clarkson, "High power fiber lasers: current status and future perspectives", J. Opt. Soc. Am. B 27, B63-B92 (2010).

[8] M. K. Davis, M. J. F. Digonnet, and R. H. Pantell, "Thermal effects in doped fibers," J. Lightwave Technol., 16, 1013–1023 (1998).

[9] E. Snitzer, "Proposed fiber cavities for optical masers," J. Appl. Phys., 32, 36-39 (1961).

[10] E. Snitzer, "Optical maser action of Nd^{+3} in a barium crown glass," Phys. Rev. Lett., 7, 444–446 (1961).

[11] C. A. Burrus and J. Stone, "Nd^{+3} doped SiO_2 lasers in an end-pumped fiber geometry," Appl. Phys. Lett., 23, 388-389 (1973).

[12] R. J. Mears, L. Reekie, I. M. Juancey, and D. N. Payne, "Low-noise erbium-doped fiber amplifier operating at 1.54 μm," Electron. Lett., 23, 1026-1028 (1987).

[13] E. Shcherbakov, V. Fomin, A. Abramov, A. Ferin, D. Mochalov, and V. P. Gapontsev, Proc. Adv. Solid State Lasers, 27 October – 1 November 2013, Paris, France. (Optical Society of America, 2013), Paper ATh4A.

[14] K. Iizawa, S.K. Varshney, Y. Tsuchida, K. Saitoh, and M. Koshiba, "Bend-insensitive lasing characteristics of single-mode, large-mode-area Ytterbium-doped photonic crystal fibers," Optics Express 16, 579-591 (2008).

[15] I. Abdelaziz, H. Ademgil, F. AbdelMalek, S. Haxha, T. Gorman and H. Bouchriha, “Design of a large effective mode area photonic crystal fiber with modified rings”, Opt. Comm. 283, 5218-5223 (2010).

[16] N. G. R. Broderick, D. J. Richardson, D. Taverner, J. E. Caplen, L. Dong and M. Ibsen, " High-power chirped-pulse all-fiber amplification system based on large-mode-area fiber gratings," Opt. Lett. 24, 566-568 (1999).

[17] G. P. Lees, D. Taverner, D. J. Richardson, L. Dong and T. P. Newson, "Q-switched erbium doped fiber laser utilising a novel large mode area fiber," Electron. Lett. 33, 393-394 (1997).

[18] H. L. Offerhaus, N. G. Broderick, D. J. Richardson, R. Sammut, J. Caplen and L. Dong, "High-energy single-transverse-mode Q-switched fiber laser based on a multimode large-mode-area erbium-doped fiber," Opt. Lett. 23, 1683-1685 (1998).

[19] J. C. Knight, T. A. Birks, R. F. Cregan, P. St. J. Russell and J. P. De Sandro, "Large mode area photonic crystal fibre" Electron. Lett. 34, 1347 (1998).

[20] J. Limpert, T. Schreiber, S. Nolte, H. Zellmer, A. Tunnermann, R. Iliew, F. Lederer, J. Broeng, G. Vienne, A. Petersson and C. Jakobsen, "High-power air-clad large-mode-area photonic crystal fiber laser," Opt. Exp. 818, 11, (2003).

[21] J. R. Folkenberg, M. D. Nielsen, N. A. Mortensen, C. Jakobsen and H. R. Simonsen, "Polarization maintaining large mode area photonic crystal fiber," Opt. Exp. 956, 12 (2004).

[22] B. L. Behera, A. Maity, S. K. Varshney and R. Datta, "Theoretical investigations of trench-assisted large mode-area, low bend loss and single-mode microstructured core fibers," Optics Commun. 307, 9-16 (2013).

[23] M. E. Fermann, “Single-mode excitation of multimode fibers with ultrashort pulses,” Opt. Lett. 23, 52-54 (1998).

[24] J. P. Koplow, D. A. V. Kilner and L. Goldberg, “Single-mode operation of a coiled multimode fiber amplifier”, Opt. Lett. 25, 442-444, (2000).

[25] V. Rastogi and K. S. Chiang, "Leaky optical fiber for large mode area single mode operation,” Electron. Lett. 39, 1110-1112 (2003).

[26] A. Kumar, V. Rastogi, C. Kakkar and B. Dussardier, "Co-axial dual-core resonant leaky fibre for optical amplifiers," J. Opt. A: Pure Appl. Opt. 10, 115306 (2008).

[27] B. Dussardier, V. Rastogi, A. Kumar and G. Monnom, "Large-mode-area leaky optical fiber fabricated by MCVD," Appl. Opt. 50, 3118- 3122 (2011).

[28] S. Fevrier, D. Gaponov, M. Devautour, P. Roy, L. Daniault, M. Hanna, D. N. Papadopoulos, F. Druon, P. Georges, M. E. Likhachev, M. Y. Salganskii and M.

V.Yashkov, "Photonic bandgap fiber oscillators and amplifiers," Opt. Fiber Technol. 16, 419-427 (2010).

[29] J. Limpert, F. Stutzki, F. Jensen, H. J. Otto, T. Eidam, C. Jauregui and A. Tunnermann, "Yb- doped large-pitch fibers: effective single-mode operation based on higher-order mode delocalization," Light: Science & applications 1, (2012).

[30] V. Rastogi and K. S. Chiang, "Propagation characteristics of a segmented cladding fiber," Opt. Lett. 26, 491-493 (2001).

[31] V. Rastogi and K. S. Chiang, "Analysis of segmented-cladding fiber by the radial-effective-index method," Opt. Soc. Am. B 21, 258-265 (2004).

[32] S. K. Varshney, K. Saitoh, M. Koshiba, B.P. Pal, and R.K. Sinha, "Design of S-band Erbium-doped, concentric dual-core photonic crystal fiber amplifiers with ASE and SRS suppression," J. Lightwave Technol., 27, 1725-1733 (2009).

[33] P. Russell, "Photonic crystal fibers," Science 299, 358 (2003).

[34] J C Knight T. A. Birks, D. M. Atkin, and P. St. J. Russell, "Pure silica single-mode fiber with hexagonal photonic crystal cladding," *Proc*. Optical Fiber Communication 2, OSA Technical Digest Series, Optical Society of America, San Jose, CA, USA, 1996.

[35] T. A. Birks, J. C. Knight, and P. St. J. Russell, "Endlessy single-mode photonic crystal fiber," Opt. Lett., 22(13), 961–963 (1997).

[36] B. J. Mangan, J. C. Knight, T. A. Birks, P. St. J. Russell, and A. H. Greenaway, "Experimental study of dual-core photonic crystal fibre," Elect. Lett. 36, 1358-1359 (2000).

[37] A. Ortigosa-Blanch, J. C. Knight, W. J. Wadsworth, J. Arriaga, B. J. Mangan, T. A. Birks, P. St and J. Russell, "Highly birefringent photonic crystal fibers," Opt. Lett. 25(18), 1325-1327(2000).

[38] W. J. Wadsworth, J. C. Knight, W. H. Reeves, P. S. Russell, and J. Arriaga, "Yb^{3+} -doped photonic crystal fiber laser," Elect. Lett. 36, 1452–1454 (2000).

[39] Y. Tsuchida, K. Saitoh, and M. Koshiba, "Design and characterization of single-mode holey fibers with low bending losses," Opt. Exp. 13(12), 4770-4779 (2005).

[40] J. M. Schmitt, "Optical coherence tomography (OCT): A review," IEEE J. Sel. Topics Quant. Elect. 5(4), 1205-1215 (1999).

[41] G. P. Agrawal, Nonlinear Fiber Optics, 5^{th} ed., Elsevier Academic Press (Oxford, UK), 2013.

[42] A. Schliesser, N. Picque, and T. W. Hansch, "Mid-infrared frequency combs," Nature Photon. 6, 440 – 449 (2012).

[43] P. Hsiung, Y. Chen, T. H. Ko, J. G. Fujimoto, C. J. S. de Matos, S. V. Popov, J. R. Taylor, and V. P. Gapontsev, “Optical coherence tomography using a continuous-wave, high-power, Raman continuum light source,” Opt. Exp. 12, 5287–5295 (2004).

[44] R. R. Alfano, and S. L. Shapiro, “Emission in the region 4000 to 7000 Å via four-photon coupling in glass,” Phys. Rev. Lett. 24, 584 (1970).

[45] H. Takara, T. Ohara, T. Yamamoto, H. Masuda, M. Abe, H. Takahashi, and T. Morioka, “Field demonstration of over 1000-channel DWDM transmission with supercontinuum multi-carrier source,” Elect. Lett. 41, 270–271 (2005).

[46] S. Sanders, “Wavelength-agile fiber laser using group-velocity dispersion of pulsed super-continua and application to broadband absorption spectroscopy,” Appl. Phys. B: Lasers and Optics 75, 799–802 (2002).

[47] A. B. Seddon “A prospective for new mid-infrared medical endoscopy using chalcogenide glasses,” Int. J. Appl. Glass Sci. 2, 177-191 (2011).

[48] P. Ma, D. Y. Choi, Y. Yu, X. Gai, Z. Yang, S. Debbarma, S. Madden, and B. L. Davies, " Low-loss chalcogenide waveguides for chemical sensing in the mid-infrared," Opt. Exp. 21(24), 29927 – 29937 (2013).

[49] S. Gross, N. Jovanovic, A. Sharp, M. Ireland, J. Lawrence, and M. J. Withford, "Low loss mid-infrared ZBLAN waveguides for future astronomical applications," Opt. Exp. 23(6), 7946 – 7956 (2015).

[50] N. Granzow, S. P. Stark, M. A. Schmidt, A. S. Tverjanovich, L. Wondraczek, and P. St.J. Russell, "Supercontinuum generation in chalcogenide silica step-index fibers," Opt. Exp. 19(21), 21003 – 21010 (2011).

[51] W. Gao, M. El. Amraoui, M. Liao, H. Kawashima, Z. Duan, D. Deng, T. Cheng, T. Suzuki, Y. Messaddeq, and Y. Ohishi, "Mid-infrared supercontinuum generation in a suspended-core As2S3 chalcogenide microstructured optical fiber," Opt. Exp. 21(8), 9573 – 9583 (2013).

[52] I. Kubat, C. S. Agger, U. Moller, A. B. Seddon, Z. Tang, S. Sujecki, T. M. Benson, David Furniss, S. Lamrini, K. Scholle, P. Fuhrberg, B. Napier, M. Farries, J. Ward, P. M. Moselund, and O. Bang, “Mid-infrared supercontinuum generation to 12.5μm in large NA chalcogenide step-index fibres pumped at 4.5μm,” Opt. Exp. 22(16), 19169-19182 (2014).

[53] C. R. Petersen, U. Moller, I. Kubat, B. Zhou, S. Dupont, J. Ramsay, T. Besson, S. Sujecki, N. Abdel-Moneim, Z. Tang, D. Furniss, A. Seddon, and O. Bang, “Mid-infrared supercontinuum covering the 1.4 – 13.3 μm molecular fingerprint region

using ultra-high NA chalcogenide step-index fibre," Nature Photon. 8, 830 – 834 (2014).

[54] L. Zhang, Y. Yan, Y. Yue, Q. Lin, O. Painter, R. G. Beausoleil, and A. E. Willner, " On-chip two-octave supercontinuum generation by enhancing self-steepening of optical pulses," Opt. Exp. 19(12), 11584 – 11590 (2011).

[55] R. Halir, Y. Okawachi, J. S. Levy, M. A. Foster, M. Lipson, and A. L. Gaeta, "Ultrabroadband supercontinuum generation in a CMOS-compatible platform," Opt. Lett. 37(10), 1685 – 1687 (2012).

[56] J. McCarthy, H. T. Bookey, N. D. Psaila, R. R. Thomson, and A. K. Kar, "Mid-infrared spectral broadening in an ultrafast laser inscribed gallium lanthanum sulphide waveguide", Opt. Exp. 20, 1545 – 1551 (2012).

[57] J. McCarthy, H. Bookey, S. Beecher, R. Lamb, I. Elder, and A. K. Kar, "Spectrally tailored mid-infrared super-continuum generation in a buried waveguide spanning 1750 nm to 5000 nm for atmospheric transmission," Appl. Phys. Lett. 103, 151103 (2013).

[58] H. Hu, W. Li, N. K. Dutta, "Dispersion-engineered tapered planar waveguide for coherent supercontinuum generation," Opt. Commun. 324, 252–257 (2014).

[59] J. Safioui, F. Leo, B. Kuyken, S. P. Gorza, S. K. Selvaraja, R. Baets, P. Emplit, G. Roelkens, and S. Massar, "Supercontinuum generation in hydrogenated amorphous silicon waveguides at telecommunication wavelengths," Opt. Exp. 22(3), 3090 – 3097 (2014).

[60] M. R. Karim, B. M. A. Rahman, and G. P. Agrawal, "Mid-infrared supercontinuum generation using dispersion-engineered $Ge_{11.5}As_{24}Se_{64.5}$ chalcogenide channel waveguide," Opt. Exp. 23(5), 6903 – 6914 (2015).

[61] V. Shiryaev and M. Churbanov, "Trends and prospects for development of chalcogenide fibers for mid-infrared transmission," J. Non-Cryst. Solids 377, 225 – 230 (2013).

[62] R. E. Slusher, G. Lenz, J. Hodelin, J. Sanghera, L. B. Shaw, and I. D. Aggarwal, "Large Raman gain and nonlinear phase shift in high-purity As_2Se_3 chalcogenide fibers," J. Opt. Soc. Am. B 21, 1146–1155 (2004).

[63] M. Klimczak, B. Siwicki, P. Skibinski, D. Pysz, R. Stepien, A. Heidt, C. Radzewicz, and R. Buczynski, "Coherent supercntinuum generation up to 2.3 μm in all-solid soft-glass photonic crystal fibers with flat all-normal dispersion," Opt. Exp. 22(15), 18824 – 18832 (2014).

[64] J. Limpert, F. Roser, D. N. Schimpf, E. Seise, T. Eidam, S. Hadrich, J. Rothhardt, C. J. Misas, A. Tunnermann, “High repetition rate gigawatt peak power fiber laser-systems: Challenges, design, and experiment,” IEEE J. Sel. Top. Quantum Electron. 15, 159–169 (2009).

[65] M. Napierala, E. B. Pawlik, T. Nasilowski, P. Mergo, F. Berghmans, H. Thienpont, "Photonic crystal fiber with large mode area and characteristic bending properties," IEEE Photon. Technol. Lett. 24, 1409-1411 (2012).

[66] J. Ballato, A. F. Abouraddy, "Feature issue introduction: specialty optical fibers," Optical Materials Exp. 2, 1680-1682 (2012).

[67] H. Ademgil and S. Haxha, "Endlessly single mode photonic crystal fiber with improved effective mode area,” Opt. Commun. 285, 1514-1518 (2012).

[68] J. Li, J. Wang, Y. Cheng, R. Wang, B. Zhang, and H. Wang, "Novel large mode area photonic crystal fibers with selectively material-filled structure," Opt. & Laser Tech. 48, 375-380 (2013).

[69] L. Dong, T. Wu, H. A. McKay, Fu. J. Li, and H. G. Winful, "All-glass large core leakage channel fibers," IEEE J. Select. Top. Quant. Electron. 15, 47-53 (2009).

[70] K. Kishor, R. K. Sinha, and A. D Varshney, "Experimental verification of improved effective index method for endlessly single mode photonic crystal fiber," Opt. Lasers Eng. 50, 182-186 (2012).

[71] L. Dong, X. Peng, and J. Li, “Leakage channel optical fibers with large effective area,” J. Opt. Soc. Am. B 24(8), 1689–1697 (2007).

[72] T. Wu, L. Dong, and H. Winful, "Bend performance of leakage channel fibers," Opt. Exp. 16, 4278-4285 (2008).

[73] A. Kumar and V. Rastogi, "Design and analysis of dual-shape-core large-mode-area optical fiber," Appl. Opt. 50, E119-E124 (2011).

[74] A. Kumar and V. Rastogi, "Design and analysis of a multilayer cladding large-mode-area optical fibre," J. Opt. A: Pure Appl. Opt. 10, 015303 (2008).

[75] Y. Tsuchida, K. Saitoh, and M. Koshiba, Design of single-moded holey fibers with large-mode-area and low bending losses: the significance of the ring-core region,” Opt. Exp. 15, 1794–1803 (2007).

[76] M. M. Vogel, M. A. Ahmed, A. Voss, and T. Graf, "Very-large-mode-area, single-mode multicore fiber," Opt. Lett. 34(18), 2876-2878 (2009).

[77] B. Morasse, S. Chatigny, C. Desrosiers, E. Gagnon, M. A. Lpointe, and J. P. Sandro, "Simple design for single mode high power CW fiber laser using multimode high NA fiber," *Proc*. SPIE 7195, Fiber Lasers VI: Technology,

Systems, and Applications, 719505 (February 19, 2009); doi: 10.1117/12.807164.

[78] I. Abdelaziz, F. Abdelmalek, H. Ademgil, S. Haxha, T. Gorman, and H. Bouchriha, "Enhanced effective area photonic crystal fiber with novel air hole design," J. Lightwave Technol. 28, 2810-2817 (2010).

[79] X. Wang, S. Lou, and W. Lu, "Bending orientation insensitive large mode area photonic crystal fiber with triangular core," IEEE Photon. J. 5, 7100408 (2013).

[80] M. Y. Chen, Y. R. Li, J. Zhou, and Y. K. Zhang, "Design of asymmetric large-mode-area optical fiber with low-bending loss," J. Lightwave. Technol. 31, 476-481 (2013).

[81] M. A. Islam, and M. S. Alam, "An Extremely Large Mode Area Microstructured Core Leakage Channel Fiber With Low Bending Loss," J. Lightwave Technol. 32, 250-256 (2014).

[82] S. Guenneu, A. Nicolet, F. Zolla, and S. Lasquellec, "Numerical and Theoretical Study of Photonic Crystal Fibers," Prog. Electromagn. Res. 41, 271-305 (2003).

[83] M. Koshiba, Y. Tsuji, and S. Sasaki, "High-performance absorbing boundary conditions for photonic crystal waveguide simulations," IEEE Microwave Wirel. Compon. Lett. 11, 152–154 (2001).

[84] N. H. Vu, I. K. Hwang, and Y. H. Lee, "Bending loss analyses of photonic crystal fibers based on the finite-difference time-domain method," Opt. Lett. 33 (2008) 119-121 (2008).

[85] K. Saitoh and M. Koshiba, "Full-vectorial imaginary-distance beam propagation method based on a finite element scheme: Application to photonic crystal fibers," IEEE J. Quantum Electron. 38, 927-933 (2002).

[86] F. Zolla, G. Renversez, A. Nicolet, B. Kuhlmey, S. Guenneau, and D. Felbacq, "Foundations of Photonic Crystal Fibres", Imperial College Press, London, ISBN: 1–86094–507–4, (2005).

[87] M. J. Li, X. Chen, A. Liu, S. Gray, J. Wang, D. T. Walton and L. A. Zenteno, "Fiber design for higher power laser", *Proc*. SPIE 6469, 64690H, (2007).

[88] M.-C. Oh, S.-H. Cho, Y.-O. Noh, H.-J. Lee, J.-J. Joo and M.-H. Lee, "Variable optical attenuator based on large-core single-mode polymer waveguide," IEEE Photon. Technol. Lett. 17, 1890-1892 (2005).

[89] A. Kumar, V. Rastogi and K. S. Chiang, "Large-core single-mode channel waveguide based on geometrically shaped leaky cladding," Appl. Phys. B: Laser and Optics 90, 507-512 (2008).

[90] X. Wang, S. Lou and W. Lu, “Bend-resistant large-mode-area photonic crystal fiber with a triangular-core,” Appl. Opt. 52(18), 4323-4328 (2013).

[91] J. M. Eggleston, T. J. Kane, K. Kuhn, R. L. Byer, and J. Unternahrer, “The slab geometry laser I-Theory,” IEEE J. Quantum Electron. 20, 289–301 (1984).

[92] J. N. Walpole, J. P. Donnelly, P. J. Taylor, L. J. Missaggia, C. T. Harris, R. J. Bailey, A. Napoleone, S. H. Groves, S. R. Chin, R. Huang, and J. Plant, “Slab-coupled 1.3-μm semiconductor laser with single-spatial large-diameter mode”, IEEE Photon. Technol. Lett. 14, 756-758 (2002).

[93] R. K. Huang, and L. J. Missaggia, J. P. Donnelly, C. T. Harris, and G. W. Turner, “High-brightness slab-coupled optical laser arrays”, IEEE Photon. Technol. Lett. 17, 959-961 (2005).

[94] X. Zhang, B. Lee, C. Lin, A. X. Wang, A. Hosseini, and R. T. Chen, “Highly linear broadband optical modulator based on electro-optic polymer", IEEE Photon. Journal 4(6), 2214 – 2228 (2012).

[95] C. Y. Lin, A. X. Wang, B. S. Lee, X. Zhang, and R. T. Chen, "High dynamic range electric field sensor for electromagnetic pulse detection," Opt. Exp. 19, 17372 – 17377 (2011).

[96] X. Li, P. C. Li, L. Ji, C. Stender, C. McPheeters, S. R. Tatavarti, K. Sablon, and E. T. Yu “Subwavelength nanostructures integrated with polymer-packaged III/V solar cells for omnidirectional, broad-spectrum improvement of photovoltaic performance,” Prog. Photovoltaics: Res. Appl. DOI: 10.1002/pip.2565, (2014).

[97] D. P. Shepherd, S.J. Hettrick, C. Li, J.I. Mac-kenzie, R.J. Beach, S.C. Mitchell, and H. E. Meissner, “High-power planar dielectric waveguide lasers”, J. Phys. D Appl. Phys. 34, 2420-2432 (2001).

[98] M. C. Oh, S. H. Cho, Y. O. Noh, H. J. Lee, J. J. Joo and M. H. Lee, “Variable optical attenuator based on large-core single-mode polymer waveguide”, IEEE Photon. Technol. Lett. 17, 1890-1892 (2005).

[99] J. C. Shelton, F. K. Reinhart, and R. A. Logan, “Characteristics of rib waveguides in AlGaAs,” J. Appl. Phys., 50, 6675–6687 (1979).

[100] J. M. Heaton, M. M. Bourke, S. B. Jones, B. H. Smith, K. P. Hilton, G. W. Smith, J. C. H. Birbeck, G. Berry, S. V. Dewar and D. R. Wight, “Optimization of deep-etched, single-mode GaAs/AlGaAs optical waveguides using controlled leakage into the substrate”, J. Lightwave Technol., 17, 267-281 (1999).

[101] A. Kumar, V. Rastogi and K. S. Chiang, “Leaky optical waveguide for high power applications”, Appl. Phys. B 85, 11-16 (2006).

[102] A. Kumar and V. Rastogi, "Multilayer cladding leaky planar waveguide for high power applications," Appl Phys B 92, 577-583 (2008).

[103] I. Hartl, X. D. Li, C. Chudoba, R. K. Ghanta, T. H. Ko, J. G. Fujimoto, J. K. Ranka, and R. S. Windeler, "Ultrahigh-resolution optical coherence tomography using continuum generation in an air-silica microstructure optical fiber," Opt. Lett. 26, 608–610 (2001).

[104] J. Ye, H. Schnatz, and L. Hollberg, "Optical frequency combs: from frequency metrology to optical phase control," IEEE J. Sel. Topics Quant. Elect. 9, 1041–1058 (2003).

[105] C. Dunsby, P. M. P. Lanigan, J. McGinty, D. S. Elson, J. Requejo-Isidro, I. Munro, N. Galletly, F. McCann, B. Treanor, B. Onfelt, D. M. Davis, M. A. A. Neil, and P. M. W. French, "An electronically tunable ultrafast laser source applied to fluorescence imaging and fluorescence lifetime imaging microscopy," J. Phys. D: Applied Physics 37, 3296–3303 (2004).

[106] M. Ere-Tassou, C. Przygodzki, E. Fertein, and H. Delbarre, "Femtosecond laser source for real-time atmospheric gas sensing in the UV - visible," Opt. Commun. 220, 215–221 (2003).

[107] J. Wegener, R. H. Wilson and H. S. Tapp, "Mid-infrared spectroscopy for food analysis: recent new applications and relevant developments in sample presentation methods," Trends Anal. Chem. 18, 85-93 (1999).

[108] J. M. Dudley, G. Genty, and S. Coen, "Supercontinuum generation in photonic crystal fiber," Rev. Mod. Phys. 78(4), 1135–1184 (2006).

[109] J. Swiderski and M. Michalska, "Mid-infrared supercontinuum generation in a single-mode thulium-doped fiber amplifier," Laser Phys. Lett. 10, 035105(2013).

[110] J. K. Ranka, R. S. Windeler and A. J. Stentz, "Visible continuum generation in air silica microstructured optical fibers with anomalous dispersion at 800 nm," Opt. Lett. 25(1), 25-27 (2000).

[111] M. El-Amraoui, G. Gadret, J. C. Jules, J. Fatome, C. Fortier and J. Troles, "Microstructured chalcogenide optical fibers from As_2S_3 glass: towards new IR broadband sources," Opt. Exp. 18, 26655-26665 (2010).

[112] L. Liu, G. Qin, Q.Tian, D. Zhao, and W. Qin, "Numerical investigation of mid-infrared supercontinuum generation up to 5 μm in single mode fluoride fiber," Opt. Exp. 19, 10041-10048 (2011).

[113] W. Yuan "2–10 μm mid-infrared supercontinuum generation in As_2Se_3 photonic crystal fiber," Laser Phys. Lett. 10(9), 095107 (2013).

[114] P. Yan, R. Dong, G. Zhang, H. Li, S. Ruan, H. Wei, J. Luo, “Numerical simulation on the coherent time-critical 2-5 μm supercontinuum generation in an As_2S_3 microstructured optical fiber with all-normal flat-top dispersion profile,” Opt. Commun. 293, 133-138 (2013).

[115] L. B. Shaw, V. Q. Nguyen, J. S. Sanghera, I. D. Aggarwal, P. A. Thielen, and F. H. Kung, “IR supercontinuum generation in As-Se photonic crystal fiber,” *Proc*. Adv. Solid State Photon., paper TuC5 (2005).

[116] J. Hu, C. R. Menyuk, L. B. Shaw, J. S. Sanghera, and I. D. Aggarwal, "Maximizing the bandwidth of supercontinuum generation in As_2Se_3 chalcogenide fibers," Opt. Exp. 18(7), 6722-6739 (2010).

[117] I. Kubat, C. S. Agger, P. M. Moselund, and O. Bang, “Mid-infrared supercontinuum generation to 4.5 μm in uniform and tapered ZBLAN step-index fibers by direct pumping at 1064 or 1550 nm,” J. Opt. Soc. Am. B 30 (10), 2743-2757 (2013).

[118] I. Kubat, C. R. Petersen, U. V. Moller, A. Seddon, T. Benson, L. Brilland, D. Mechin, P. M. Moselund, and O. Bang, “Thulium pumped mid-infrared 0.9-9 μm supercontinuum generation in concatenated fluoride and chalcogenide glass fibers,” Opt. Exp. 22 (4), 3959 - 3969 (2014).

[119] W. Liu, L. Pang, X. Lin, R. Gao, and X. Song, “Observation of soliton fission in microstructured fiber,” Appl. Opt. 51(34), 8095 – 8101 (2012).

[120] A. V. Husakov and J. Herrmann, “Supercontinuum generation of higher order solitons by fission in photonic crystal fibers,” Phys. Rev. Lett. 87, 203901 (2001).

[121] G. Steinmeyer and J. S. Skibina, “Entering the mid-infrared,” Nature Photon. (news & views) 8(11), 814-815 (2014).

[122] N. Leindecker, A. Marandi, R. L. Byer, K. L. Vodopyanov, J. Jiang, I. Hartl, M. Fermann, and P. Schunemann, “Octave-spanning ultrafast OPO with 2.6 – 6.1 μm instantaneous bandwidth pumped by femtosecond Tm-fiber laser,” Opt. Exp. 20, 7046- 7053 (2012).

[123] H. G. Dantanarayana, N. Abdel-Moneim, Z. Tang, L. Sojka, S. Sujecki, D. Furniss, A. B. Seddon, I. Kubat, O. Bang, and T. M. Benson, “Refractive index dispersion of chalcogenide glasses for ultra-high numerical-aperture fiber for mid-infrared supercontinuum generation,” Opt. Mat. Exp. 4(7), 1444-1455 (2014).

[124] B. Ung and M. Skorobogatiy, "Chalcogenide microporous fibers for linear and nonlinear applications in the mid-infrared," Opt. Exp. 18(8), 8647-8659 (2010).

[125] M. Klimczak, G. Stepniewski, H. Bookey, A. Szolno, R. Stepien, D. Pysz, A. Kar, A. Waddie, M. R. Taghizadeh, and R. Buczynski, "Broadband infrared supercontinuum generation in hexagonal-lattice tellurite photonic crystal fiber with dispersion optimized for pumping near 1560 nm," Opt. Lett. 38(22), 4679-4682 (2013).

[126] A. Baili, R. Cherif, A. Heidt, and M. Zghal, "Maximizing the bandwidth of coherent, mid-IR supercontinuum using highly nonlinear aperiodic nanofibers", J. Modern Opt. 61 (8), 650-661 (2014).

[127] G. Genty, M. Lehtonen, H. Ludvigsen, J. Broeng, and M. Kaivola, "Spectral broadening of femtosecond pulses into continuum radiation in microstructured fibers," Opt. Exp. 10(20), 1083 – 1098 (2002).

[128] M. A. Foster, and A. L. Gaeta, "Ultra-low threshold supercontinuum generation in sub-wavelength waveguides," Opt. Exp. 12(14), 3137 – 3143 (2004).

[129] L. Yin, Q. Lin, and G. P. Agrawal, "Soliton fission and supercontinuum generation in silicon waveguides," Opt. Lett. 32(4), 391 – 393 (2007).

[130] M. R. E. Lamont, B. L. Davies, D. Y. Choi, S. Madden, and B. J. Eggleton, "Supercontinuum generation in dispersion engineered highly nonlinear (γ = 10 /W/m) As_2S_3 chalcogenide planar waveguide," Opt. Exp. 16(19), 14938 – 14944 (2008).

[131] M. R. Karim, B. M. A. Rahman, and G. P. Agrawal, "Dispersion engineered $Ge_{11.5}As_{24}Se_{64.5}$ nanowire for supercontinuum generation: A parametric study," Opt. Exp. 22(25), 31029 – 31040 (2014).

[132] X. Gai, T. Han, A. Prasad, S. Madden, D. Y. Choi, R. Wang, D. Bulla, and B. L. Davies, "Progress in optical waveguides fabricated from chalcogenide glasses," Opt. Exp. 18(25), 26625 – 26646 (2010).

[133] B. J. Eggleton, "Chalcogenide photonics: fabrication, devices and applications Introduction," Opt. Exp. 18(25), 26632 – 26634 (2010).

[134] Y. Yu, X. Gai, T. Wang, P. Ma, R. Wang, Z. Yang, D. Y. Choi, S. Madden, and B. L. Davies, "Mid-infrared supercontinuum generation in chalcogenides," Opt. Mat. Exp. 3(8), 1075 – 1086 (2013).

[135] B. J. Eggleton, B. L. Davies, and K. Richardson, "Chalcogenide photonics," Nature Photon. 5, 141 – 148 (2011).

[136] J. T. Mok and B. J. Eggleton, "Expect more delays," Nature 433, 811-812 (2005).

[137] S. Rawal, R. K. Sinha, and R. M. De La Rue, Slow light miniature devices with ultra-flattened dispersion in silicon-on-insulator photonic crystal, Opt. Exp.17, 13315-13325 (2009).

[138] S. Rawal, R. K. Sinha and R. M. De La Rue, Silicon-on-insulator photonic crystal miniature devices with slow light enhanced third-order nonlinearities, J. Nanophoton. 6, 063504 (2012).

[139] M. Santagiustina, G. Eisenstein, L. Thevenaz, J. Capmany, J. Mork, J.P. Reithmaier, A. D. Rossi, S. Sales, K. Yvind, S. Combrie and J. Bourderionnet, Slow light devices and their applications to microwaves and photonics, IEEE Photon. Soc. Newsletter, 5-12 (2012).

[140] K. Y. Song, M. Gonzalez Herraez, and L. Thevenaz, Observation of pulse delaying and advancement in optical fibers using stimulated Brillouin scattering, Opt. Exp. 13, 82-88 (2005).

[141] J. Sharping, Y. Okawachi and A. Gaeta, Wide bandwidth slow light using a Raman fiber amplifier, Opt. Exp.13, 6092–6098 (2005).

[142] L. Y. Ren and Y. Tomita, Transient and nonlinear analysis of slow-light pulse propagation in an optical fiber via stimulated Brillouin scattering, J. Opt. Soc. Am. B 26, 1281-1288 (2009).

[143] S. H. Wang, L. Y. Ren, Y. Liu and Y. Tomita, Zero-broadening SBS slow light propagation in an optical fiber using two broadband pump beams, Opt. Exp. 16, 8067-8076 (2008).

[144] D. Dahan and G. Eisenstien, Tunable all optical delay via slow and fast light propagation in a Raman assisted fiber optical parametric amplifier: a route to all optical buffering, Opt. Exp. 13, 6234-6248 (2005).

[145] E. P. Ippen and R. H. Stolen, “Stimulated Brillouin scattering in optical fibers,” Appl. Phys. Lett. 21, 539-540 (1972).

[146] A. Kobyakov, M. Sauer, and D. Chowdhury, “Stimulated Brillouin scattering in optical fibers,” Adv. Opt. Photon. 2, 1–59 (2010).

[147] E. Shumakher, A. Willinger, R. Blit, D. Dahan and G. Eisenstein, "Large tunable delay with low distortion of 10 Gbit/s data in a slow light system based on narrow band fiber parametric amplification," Opt. Exp. 14, 8540-8545 (2006).

[148] M. S. Bigelow, N. N. Lepeshkin and R. W. Boyd, "Superluminal and slow-light propagation in a room-temperature solid," Science 301, 200-202 (2003).

[149] T. Baba, "Slow light in photonic crystals", Nature Photon. 2, 465-473 (2008).

[150] T. Schneider, D. Hannover and M. Junker, "Investigation of Brillouin scattering in optical fibers for the generation of millimeter waves," J. Lightw. Tech. 24, 295- 304 (2006).

[151] K. S. Abedin, "Observation of strong stimulated Brillouin scattering in single-mode As_2Se_3 chalcogenide fiber," Opt. Exp. 13, 10266–10271 (2005).

[152] C. florea, M. Bashkanshy, Z. Dutton, J. Sanghera, P. Pureza and I. Aggarwal, "Stimulated Brillouin scattering in single-mode As_2S_3 and As_2Se_3 chalcogenide fibers," Opt. Exp. 14, 12063-12070 (2006).

[153] J. H. Lee, T. Tanemura, K. Kikuchi, T. Nagashima, T. Hasegawa, S. Ohara, and N. Sugimoto, "Experimental comparison of a Kerr nonlinearity figure of merit including the stimulated Brillouin scattering threshold for state-of-art nonlinear optical fibers," Opt. Lett. 30, 1698–1700 (2005).

[154] K. S. Abedin, "Stimulated Brillouin scattering in single-mode tellurite glass fiber," Opt. Exp.,14(24), 11766–11772 (2006).

[155] K. S. Abedin, G. W. Lu and T. Miyazaki, "Slow light generation in single mode Er-doped tellurite fiber," Electron. Lett. 44(1), 16 – 17 (2008).

[156] G. Qin, H. Sotobayashi, M. Tsuchiya, A. Mori, T. Suzuki and Y. Ohishi, "Stimulated Brillouin cattering in a single mode tellurite fiber for amplification, lasing and slow light generation," J. Lightw. Tech. 26, 492-498 (2008).

[157] S. Yang, H. Chen, C. Qiu, M. Chen, M. Chen, S. Xie, J. Li and W. Chen, "Slow-light delay enhancement in small core pure silica photonic crystal fiber based on Brillouin scattering," Opt. Lett. 33, 95-97 (2008).

[158] R. I. Woodward, E. J. R. Kelleher, S. V. Popov and J. R. Taylor, "Stimulated Brillouin scattering of visible light in small-core photonic crystal fibers," Opt. Lett. 39, 2330-2333 (2014).

[159] B. Corcoran, C. Monat1, C. Grillet, D. J.Moss, B. J. Eggleton, T. P. White, L. O'Faolain and T. F. Krauss, "Green light emission in silicon through slow-light enhanced third-harmonic generation in photonic crystal waveguides," Nature Photon.3 206 – 210 (2009).

[160] M. E. Heidari, C. Grillet, C. Monat, and B. J. Eggleton, "Dispersion engineering of slow light photonic crystal waveguides using microfluidic infiltration," Opt. Exp. 17(3), 1628 – 1635 (2009).

[161] C. Monat, B. Corcoran, D. Pudo,M. E. Heidari, C. Grillet, M. D. Pelusi, D. J. Moss, B. J. Eggleton, T. P. White, L. O'Faolain, and T. F. Krauss, "Slow light

enhanced nonlinear optics in silicon photonic crystal waveguides, IEEE J. Sel. Top. Quant. Elect. 16, 344 – 356 (2010).

[162] R. Pant, A. Byrnes, C. G. Poulton, E. Li, D. Y. Choi, S. Madden, B. L. Davies, and B. J. Eggleton, "Photonic-chip-based tunable slow and fast light via stimulated Brillouin scattering," Opt. Lett. 37(5), 969-971 (2012).

[163] Z. Zhu, D. J. Gauthier, Y. Okawachi, J. E. Sharping, A. L. Gaeta, R. W. Boyd and A. E. Willner, "Numerical study of all-optical slow-light delays via stimulated Brillouin scattering in an optical fiber," J. Opt. Soc. Am. B 22(11), 2378-2384 (2005).

[164] V. P. Kalosha, L. Chen and X. Bao, "Slow and fast light via SBS in optical fibers for short pulses and broadband pump," Opt. Exp. 14(26), 12693-12703 (2006).

[165] S. Hou, Z. Wang, Y. Shang, Y. Liu, J. Lei and Y. Xu, "Infuence of SBS gain coefficient on time delay and pulse broadening in fibers," PIERS Proceedings, Suzhou, China, September 12-16, 938-942 (2011).

[166] M. O. Van, Deventer and A. J. Boot, "Polarization properties of stimulated Brillouin scattering in single-mode fibers," J. Lightw. Tech. 12(4), 585-590 (1994).

[167] D. Cotter, "Observation of stimulated Brillouin scattering in low-loss silica fiber at 1.3 μm," Electon. Lett. 18, 495-496 (1982).

[168] K. Ogusu, H. Li and M. Kitao, "Brillouin-gain coefficients of chalcogenide glasses," J. Opt. Soc. Am. B 21, 1302-1304 (2004).

[169] S. Kim, C.S. Kee and J. Lee, "Single-mode condition and dispersion of terahertz photonic crystal fiber," J. Opt. Soc. Korea 11 (3), 97-100 (2007).

Brief Bio-Data of the Author

THAN SINGH SAINI

Present Address: Flat No. 90, Type-II, Delhi Technological University Campus, Delhi-110 042, INDIA

Contact No.: 9873572496

E-Mail: tsinghdph@gmail.com, thansingh.saini@dtu.co.in

Website: https://sites.google.com/site/thansinghsainiphy/home

Qualification:

M. Phil. (Physics): 2009 (I Division)
M. Sc (Physics): 2006 (I Division)
B. Sc (PCM) : 2004 (I Division)

Field of Interest: Specialty optical fibers/waveguides; Supercontinuum generation; Slow and fast light generation; Nonlinear optics

Publications: Journal publications: **9**; Conference proceeding publications: **23**

Software Skills: COMSOL Multiphysics, RP Fiber, Photon Design & MATLAB

Honours:

2015 : **President,** SPIE-DCE Chapter
2015 : **Vice President,** OSA DCE Chapter
2014 : **Vice President,** SPIE-DCE Chapter

Professional Activities / Services:

Volunteer Services:

- **Ambassador:** SPIE Winter school on optics, 26 – 29 December 2013, IISER-K, INDIA
- **Facilitator:** SPIE leadership workshop, 8 August 2015, San Diego, USA.
- **Talk** delivered on "*Designing of photonic crystal fibers for supercontinuum generation*" at CSIR CSIO-Chandigarh, 31 July 2015, INDIA.
- **Reviewer:** Optics Letter (OSA)

Awards/Prizes/Fellowships:

1. **SPIE Travel Scholarship (**2014)
2. **Best Presentation Award:** IONS Asia-6 Conference, IIT-KGP, WB, INDIA (2014)
3. **Best Presentation Award**: ICOL-2014, IRDE, Dehradun, INDIA (2014)
4. **OSA Chapter Officer Travel Grant:** Student Leadership Workshop, Tucson,USA (2014)
5. **OSA Travel Grant**: Siegman International School on Lasers, Stanford University, USA (2014)
6. **Best Paper Presentation Award:** SPIE-Winter School on Optics, IISER-K, INDIA (2013)
7. **SPIE Chapter Officer Travel Grant:** Chapter Student Leadership Workshop, USA (2013)
8. **Second Best Prize:** for writing a scientific essay in college level competition (2006)
9. **Ekikrit Scholarship:** from Govt. of Uttar Pradesh (1996)

Memberships of Professional societies:

(i) **IEEE:** Membership number: 93421530
(ii) **SPIE:** SPIE ID: 3477366
(iii) **OSA:** Member Number: 1051841

Date: September 2015
Place: Delhi, India **(Than Singh Saini)**